Elements of a Method for Multiscale Characterization of Recrystallization in Deformed Metals

Ahl, Sonja Rosenlund

Publication date:
2018

Document Version
Publisher's PDF, also known as Version of record

Elements of a Method for

Multiscale Characterization of Recrystallization in Deformed Metals

Sonja Rosenlund Ahl

supervised by

Henning Friis Poulsen
Dorte Juul Jensen

Department of Physics
Technical University of Denmark
February 2018

Abstract

Recrystallization of deformed metals is a complex multiscale process which involves the migration of the boundary of a recrystallizing grain into the surrounding deformed structure. The lattice of a recrystallizing grain is almost defect-free whereas the deformed structure consists of subgrains separated by low angle boundaries made up of dislocations. The migrating grain boundary is a high angle boundary and its shape is related to the characteristics of the neighbouring subgrains.

To study the structures and dynamics involved in recrystallization an appropriate experimental technique is required. Such a technique should be able to produce three-dimensional grain maps of the whole mm-sized sample and at the same time be able to zoom in on individual grains, grain boundary segments or subgrains. The technique should be fast enough to study dynamics and have high enough resolution to resolve submicron-sized structures, millidegree angular differences and strain on the order of 10^{-4}. Penetrative power to reach embedded bulk structures is necessary and preferably the technique should allow for *in situ* annealing.

X-ray imaging techniques such as three dimensional x-ray diffraction (3DXRD) and diffraction contrast tomography (DCT), that have been developed over recent years, utilize hard x-rays from a synchrotron source to produce grain maps. Zooms on individual grains are facilitated by the implementation of topo-tomography. With the introduction of a new technique, dark field x-ray microscopy (DFXRM), a spatial resolution better than 100 nm is reached together with millidegree angular resolution.

In this thesis a first application of DFXRM to recrystallization is presented together with a framework for analysing DFXRM data in terms of distortion fields and dislocation densities. Three-dimensional maps of the internal structure of recrystallizing grains in cold-rolled aluminium AA1050 were obtained by means of DFXRM in a few hours. Mosaicity and strain maps revealed that the investigated recrystallizing grains possessed a well-ordered internal network of ultra low angle boundaries. The misorientation across these boundaries was less than 0.1° and some boundaries were sharp to within the instrumental resolution whereas others were several μm wide. A clear correlation between the intragranular network and the shape of the grain boundary was observed, with retrusions at points where the ultra low angle boundaries met the external grain

boundary. Furthermore, there were indications that the ultra low angle boundary network was related to the subgrain structure that it grew from, and during annealing the intragranular structure became more well-ordered.

A new method for monitoring the structural evolution of several thousand individual subgrains during recovery is also demonstrated. At constant heat rate for temperatures well below the onset of recrystallization the size, orientation and internal strain of individual subgrains was observed to change while the overall size distribution remained unaltered. Each subgrain exhibited its own growth kinetics and in contradiction with prevalent models for recovery this study found no correlation between subgrain size and growth rate. A simple model for thermally activated recovery was applied to extract individual critical temperatures and a region of increased dynamics was observed around 160°C. Furthermore, promising first results from a preliminary test of a triangulation method for mapping subgrain structures is presented.

Dansk resumé

Rekrystallisering af deformeret metal er en kompleks multiskala proces, der involverer grænsebevægelse for det nye korn ind i den omgivende deformerede struktur. I det nye korn er krystalgitteret stort set fri for defekter, mens den deformerede struktur indeholder subkorn adskilt af lavvinkelgrænser, der består af dislokationer. Den korngrænse, der flytter sig, er en højvinkelgrænse og kornets form afhænger af de omgivende subkorns egenskaber.

For at kortlægge den struktur og dynamik, der ligger til grund for rekrystallisering, kræves passende eksperimentelle teknikker. En sådan teknik skal kunne fremstille tredimensionelle visualiseringer af kornstrukturen i millimeterstore prøver og på samme tid være i stand til at zoome ind på individuelle korn, stykker af korngrænser eller subkorn. Teknikken skal være hurtig nok til at studere dynamik og have en høj nok opløsning til at kunne kortlægge sub-mikrometer store strukturer, vinkelforskelle på milligraders og tøjninger i størrelsesordenen 10^{-4}. Teknikken skal kunne trænge ind til indre strukturer og muligheden for *in situ* varmebehandling er ønskeligt.

Visualiseringsteknikker baseret på røntgen såsom tredimensionel røntgenspredning (3DXRD) og spredningskontrast tomografi (DCT) er blevet udviklet over de seneste år og udnytter hård røntgen stråling fra en synkrotron til at visualisere kornstrukturer. Zoom til de enkelte korn kan opnås med topo-tomografi, og med den nye teknik, dark field røntgenmikroskopi (DFXRM), kan opnås en rumlig opløsning bedre end 100 nm sammen med en vinkelopløsning på milligrader.

I nærværende afhandling præsenteres den første anvendelse af DFXRM til at studere rekrystallisering. Desuden introduceres en metode til at bestemme deformationsfelter og dislokationsdensiteter fra DFXRM-data. Tredimensionelle visualiseringer af den indre struktur i nye korn i kold-valset aluminium AA1050 blev fremstillet på få timer. Mosaicitet og tøjningsfelter afslørede, at de undersøgte nye korn indeholdt et velordnet indre netværk af ultra lavvinkelgrænser. Misorienteringen henover disse grænser var mindre end 0.1°, og nogle af grænserne var smallere end instrumentopløsningen, mens andre var flere μm brede. Der sås en klar korrelation mellem disse indre grænser og den ydre korngrænses form, med indhak i korngrænsen hvor de indre lavvinkelgrænser mødte denne. Desuden fandtes indikationer af en strukturel relation mellem det indre netværk af ultra lavvinkelgrænser og den deformerede subkorn-struktur, som det nye korn

var groet ud af.

En ny metode til at følge udviklingen af strukturen for flere tusind individuelle subkorn under recovery er også præsenteret. Ved konstant temperaturforøgelse og for temperaturer under grænsen for rekrystallisering ændres størrelse, orientering of indre tøjning for individuelle subkorn, men størrelsesfordelingen for alle subkorn forblev uændret. Hvert subkorn fulgte en unik vækstkurve og i modstrid med fremherskende modeller for recovery fandtes ingen korrelation mellem subkorn størrelse og væksthastighed. En simple model for termisk aktiveret recovery blev anvendt til at bestemme individuelle kritiske temperaturer og der sås et temperaturinterval med øget dynamik omkring 160°C. Desuden præsenteres lovende første resultater fra en indledende test af en trianguleringsmetode til at visualisere subkorn strukturer.

Preface

This thesis is submitted in partial fulfilment of the requirements for obtaining the Ph.D. degree in physics at the Technical University of Denmark (DTU).

The research presented here was carried out at the Department of Physics at DTU in the period from October 2014 to February 2018.

The project has been supervised by Drs. Henning Friis Poulsen and Dorte Juul Jensen to whom I owe my deepest gratitude for their instruction and encouragement as well as for sharing their wide knowledge and joy in science. I also owe a special thanks to Hugh Simons and Anders Clemen Jacobsen for their support, patience and great company at beamtimes.

I am thankful to Carsten Detlefs, YuBin Zhang, Wolfgang Pantleon, Andrew Godfrey, and Søren Schmidt for scientific discussions and support, and to Phil Cook, Can Yilderim, Mustafacan Kutsal, Anders Filsøe Pedersen, Frederik Stöhr, Alberto Cereser, José 'Tato' Xavier Sierra Trujillo, Jun Sun, Jacob Bowen, Nicolai Ytterdal Juul, Jeff Wade, Jette Oddershede, Hanne Sørensen, and Henning Bo Nicolajsen who have all contributed to this Ph.D.-project in different ways.

I acknowledge the financial support from ERC Advanced Grant 291321 d-TXM as well as from DanScatt for travel expenses and I thank the European Synchrotron Radiation Facility (ESRF) for provision of beamtime on beamline ID06.

Finally, I am grateful to my family and friends, Fina, Eskil, Ulf, Else, Thorbjørn, Gyrithe, Emil, Emilie, Can, Anja, Maja, Theis, and Martin, for believing in me. I love you all.

Sonja Rosenlund Ahl

List of Publications

First author papers

Paper1 Ahl, S.R. Simons, H., Zhang, Y.B, Detlefs, C., Stöhr, F., Jakobsen, A.C., Juul Jensen, D., Poulsen, H.F.: *Ultra-low-angle boundary networks within recrystallizing grains.* Scripta Materialia 139 (2017) 87-91.

Paper2 Ahl, S. R., Simons, H., Jakobsen, A. C., Zhang, Y., Stöhr, F., Juul Jensen, D., Poulsen, H. F.: *Dark field X-ray microscopy for studies of recrystallization.* 36th Risø International Symposium on Materials Science, IOP Conf. Series: Materials Science and Engineering 89 (2015) 012016

Paper3 Ahl, S.R., Simons, H., Juul Jensen, D., Poulsen, H.F.: *Kinetics of individual subgrains during recovery.* In preparation.

Co-authored papers

Paper4 Simons, H., Ahl, S. R., Poulsen, H. F., Detlefs, C.: *Simulating and optimizing compound refractive lens-based X-ray microscopes.* Journal of Synchrotron Radiation 24 (2017) 392-401.

Paper5 Poulsen, H.F., Jakobsen, A.C., Simons, H., Ahl, S.R., Cook, P.K., Detlefs, C.: *X-ray diffraction microscopy based on refractive optics.* Journal of Applied Crystallography 50 (2017) 1441–1456.

Paper6 Simons, H., Jakobsen, A.C., Ahl, S.R, Detlefs, C., Poulsen, H.F.: *Multiscale 3D characterization with dark-field x-ray microscopy.* MRS Bulletin, 41 (2016) 454-459.

Paper7 Simons, H., Jakobsen, A.C., Ahl, S.R., Poulsen, H.F., Pantleon, W.P., Detlefs, C., Chu, Y.-H., Valanoor, N.: Mesoscale Symmetry Breaking by Misfit Dislocations in Epitaxial Complex Oxides. In preparation.

Conference Presentations

Presentation1 Ahl, S.R., Simons, H., Poulsen, H.F.,: *Quantifying the onset of recrystallization in deformed metals using x-rays* Sustain DTU, Kgs. Lyngby, 2017.

Presentation2 Ahl, S.R., Simons, H., Jakobsen, A.C., Juul Jensen, D., Poulsen, H.F.: *In situ multiscale 3D-mapping of embedded recrystallizing grains in aluminium.* 3DMS - 3rd International Congress on 3D Materials Science, Chicago, 2016.

Presentation3 Ahl, S.R., Simons, H., Poulsen, H.F., *Quantifying the onset of recrystallization in deformed metals using dark field x-ray microscopy.* Annual meeting of the Danish Physical Society (DFS), Middelfart, 2016.

Presentation4 Ahl, S.R., Simons, H., Jakobsen, A.C., Zhang, Y.B., Pantleon, W., Stöhr, F., Juul Jensen, D., Poulsen, H.F.: *Dark fiels x-ray microscopy for studies of ultra low angle boundaries.* TMS2016 - 145th Annual Meeting and Exhibition, Nashville, 2016.

Presentation5 Ahl, S.R., Simons, H., Jakobsen, A.C., Zhang, Y.B., Stöhr, F., Juul Jensen, D., Poulsen, H.F.: *Dark field x-ray microscopy for studies of recrystallization.* 36th Risø International Symposium on Materials Science, Roskilde, 2015.

Presentation6 Ahl, S.R.: *Røntgenmikroskopi - makrodetektiv i en mikroverden*, PhD ScienceSlam, Big Bang Konferencen, Roskilde, 2015.

Conference posters

Poster1 Ahl, S.R., Poulsen, H.F., Simons, H., Jakobsen, A.C., Zhang, Y.B., Juul Jensen, D.: *Going grainspotting and beyond with dark field x-ray microscopy.* Annual meeting of the Danish Physical Society (DFS), Kgs. Lyngby, 2015.

Poster2 Ahl, S.R., Simons, H., Jakobsen, A.C., Poulsen, H.F.: *Recovery and Recrystallization studied by dark field x-ray microscopy.* Annual meeting of the Danish Physical Society (DFS), Middelfart, 2017.

Poster3 Ahl, S.R., Simons, H., Jakobsen, A.C., Poulsen, H.F.: *Recovery and Recrystallization studied by dark field x-ray microscopy.* DanScatt annual meeting, Odense, 2017.

At the time of writing several additional publications are in earlier stages of preparation and therefore are not included in this list.

Contents

1 Introduction

The manufacturing of all sorts of metal parts from airplanes to earrings typically involves repeated deformation and annealing steps aiming at optimizing mechanical properties such as strength, fatigue resistance, hardness or ductility. Deformation involves the introduction of defects while annealing removes these defects, resulting in a more uniform crystalline structure. However, there are significant gaps in the understanding of the underlying mechanisms and how to optimize the processes for a specific purpose. The existing materials models are not complete in the sense, that it is not possible using first principle simulation tools to predict the final properties given an initial structure of the material and a given processing route. This is partly due to the lack of appropriate experimental techniques for characterization of the structural dynamics. In this thesis several elements of a generic experimental method for annealing studies of metals based on x-ray diffraction are presented and demonstrated.

Polycrystalline samples such as deformed metals typically possess structure at many different length scales ranging from single dislocations and cells in deformed microstructures at the nanometer to micrometer scale up to μm- to mm-sized recrystallized grains. Coarsening is defined as processes that result in an increase of the typical size at a certain length-scale. For metals, annealing leads to a multiscale structural coarsening process involving dislocation annealing and rearrangements (recovery), the nucleation and growth of new almost defect-free grains (recrystallization) and the curvature driven growth of the new grains at the expense of each other (grain growth). As these processes can take place simultaneously, it is important to understand the interactions between the various mechanisms. Classical characterization methods such as optical and electron microscopy study the near-surface and bulk structures must be exposed by cutting the sample, leaving a lack of options for *in situ* dynamical studies as well as the question whether results are representative of bulk behavior. Thus to quantify and investigate the induced structural changes there is a need for a non-invasive all-in-one tool for multiscale characterization, which permits fast and reliable *in situ* mapping of the morphology and crystallography in 3D and at the different length-scales simultaneously. Therefore, the ideal experimental technique for studying structural dynamics in polycrystalline samples should have penetrating power to allow bulk studies and hold the ability to zoom in and out between the different structural length scales without removing the

sample from the instrument.

Spatially resolved X-ray diffraction using a synchrotron source is ideal for such mapping. Full field tomographic methods such as three-dimensional x-ray diffraction (3DXRD) and diffraction contrast tomography (DCT) (see Chapter 2) can provide comprehensive 3D-maps of orientations of up to 20,000 grains within mm-sized specimens, but they are limited to a spatial resolution of about 2 μm. Using a microscopy approach instead, the recently developed synchrotron x-ray technique Dark Field X-Ray Microscopy (DFXRM) enables mapping of embedded grains, subgrains or cells with a spatial resolution better than 100 nm and in combination with 3DXRD or DCT one may zoom out enough to map the full grain structure of a mm-sized recrystallizing sample. With an angular resolution better than millidegrees it is even possible to map the distortion fields associated with single dislocations and low angle boundaries. DFXRM is also applicable to the study of structural dynamics in a variety of other polycrystalline samples such as functional ceramics, medical tablets, and natural specimens like ice and pieces of rock.

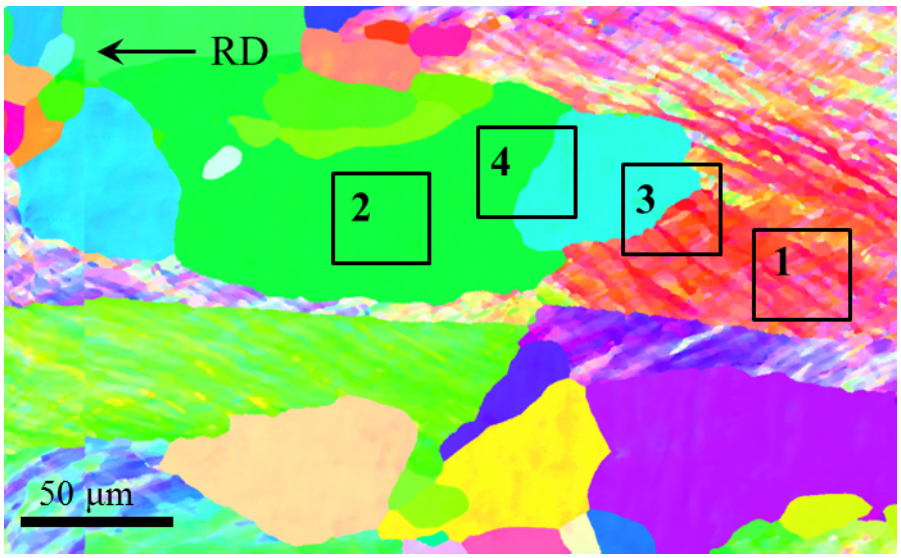

Figure 1: **EBSD map of partly recrystallized aluminium AA1050** The sample was cold-rolled to a 50% reduction in thickness and subsequently annealed at 325 °C for 50 min. to obtain approximately 50% recrystallization. The colors indicate the local orientations and the color-scale spans the full pole-figure. Courtesy of J. Sun.

This thesis exploits DFXRM for mapping and tracing the morphology and the structural changes during recrystallization of deformed aluminium, which is relevant both as a model system for proof-of-concept experiments and as an industrial material produced and processed in large quantities every day. All samples were cut from the same piece of aluminium AA1050, which had been cold-rolled to 50% reduction in thickness and subsequently annealed to obtain an approximately 50% recrystallized structure as shown in the electron backscatter diffraction (EBSD) map in Figure 1.

As indicated in the figure the resulting structure may be analysed in terms of four different types of regions with different morphologies and dynamics. In the following, the characteristics of these four regions are introduced in terms of appearance and expected mechanisms of structural evolution together with main open questions related to each region, some of which are addressed in this thesis work. A more detailed description of recrystallization and deformation with references to the literature including experimental investigations is given in Chapter 2.

1. *Subgrain structure in the interior of deformed grains*

   Plastically deformed grains have a highly disordered structure typically consisting of fuzzy cell-walls made up of many entangled dislocations and cells of slightly lower dislocation density. Upon annealing the dislocations organize further, arrange in dislocation walls and annihilate to lower the stored energy. The cells recover to a more ordered structure with largely defect-free volumes known as subgrains, separated by subgrain boundaries.

   The complexity of the cell-structure makes it difficult to predict the motion of individual dislocation lines and a lot is lacking in the understanding of the underlying mechanisms in the formation of the deformed structure as well as the recovery of cells to subgrains. Little is known about how nucleation processes giving rise to nuclei of new orientations and about the driving forces governing the size changes associated with coarsening. Therefore it is currently not possible to predict which subgrains will grow to become recrystallizing grains.

   Even the necessity of subgrain boundary migration is still an open question since alternative mechanisms are possible, but have not been unambiguously experimentally documented. For example, subgrains may coalesce by rotating towards the lattice orientation of each other if the subgrain

boundaries are sufficiently soft, or single dislocations may sweep through the subgrain and thereby alter its orientation and strain.

In this thesis a new experimental method for quantitatively monitoring the properties of hundreds of subgrains during annealing is presented. Measurements and statistical analysis of the evolution of the subgrain structure during annealing at temperatures well below the onset of recrystallization are demonstrated, sparking a discussion of the possible driving forces and mechanisms involved.

2. *Interior of recrystallizing grains of high crystallinity*

   New grains forming and growing during annealing are virtually dislocation-free, although even single crystals are known to possess an internal mosaic spread due to the presence of a small defect density. Models for recrystallization assume that the recrystallizing grains are defect-free and to appreciate the applicability of these models it is necessary to validate the underlying assumption.

   There are ways to map and quantify the shape and orientation of larger recrystallizing grains and to some extent the internal strain and spatial variations in lattice orientation may also be investigated experimentally. However, faster mapping of bulk structures with higher resolution is necessary to shed light on how the local internal properties and fields relate to the external shape and affect the structural development of the recrystallizing grain.

   In this thesis the internal structure of recrystallizing grains are mapped by means of DFXRM in terms of lattice orientation and axial strain. The distribution of remaining defects and the structural evolution during further annealing are discussed. Furthermore, it is demonstrated how the distortion fields and dislocation densities associated with few or single remaining dislocations in an embedded recrystallizing grain may be extracted from DFXRM measurements.

3. *Boundary of recrystallizing grains towards deformed material*

   The external boundaries of recrystallizing grains are sharp and migrate through the deformed structure to form an almost defect-free lattice in the new grain. The boundary migration is driven by a reduction in stored energy. However, the local structure is so complex that it is not possible to

assign a stored energy let alone predict the evolution of the structure. High resolution *in situ* mapping of the migrating grain boundary and the neighbouring deformed structure provide new insight towards the mechanisms involved and settle open questions. For example whether the subgrains closest to the boundary prepare to become part of the recrystallizing grain or the boundary motion is governed solely by the internal properties of the recrystallizing grain.

These boundaries towards deformed material are typically not smooth but possess protrusions and retrusions. Sections of these grain boundaries move in a stop-go manner, which is suggested to be governed by the characteristics of the surrounding subgrains. However, a faster technique with higher angular (and spatial) resolution is necessary to quantify potential relations between the orientation, size and internal strain of a neighbouring subgrain and its likelihood of becoming absorbed into the recrystallizing grain as the grain boundary migrates.

In this thesis the relation between the distribution of the remaining defects in the recrystallizing grain, its external shape, and the subgrain structure of the deformed material is discussed based on DFXRM-measurements and a method for simultaneously mapping the evolution of the recrystallizing grain and the surrounding deformed material utilizing the DFXRM-setup is suggested.

4. *Boundary between two recrystallizing grains*

   The boundary between two recrystallizing grains is generally smooth. It is characterized by the misorientation between the two neighbouring grains, by the (local) curvature of the boundary, and by the inclination of the boundary with respect to the crystallographic lattice. The boundary migrates with a velocity given by the product of the boundary mobility and the driving force. Real metals exhibit relatively large anisotropies, with e.g. mobilities varying by several orders of magnitude depending on misorientation angle.

   Grain growth, the coarsening of a fully recrystallized grain structure, has been extensively studied utilizing techniques such as 3DXRD, DCT, and EBSD as well as numerical simulations, and analytical expressions exist for idealized (isotropic) geometries. However, a model of grain growth for

real specimens is still far away, as the local mobilities and energies are largely unknown and not experimentally verified except for a few special cases. Also, the basic assumptions need to be tested. Another issue is that the boundary movement between two newly recrystallized grains is likely to be in a transition stage, where the idealized situation of grain growth (involving e.g. self-similarity) does not apply.

Combining DFXRM with 3DXRD or DCT at the same setup provides the opportunity to obtain a full 3D grain map and then zoom in on specific grains one by one to map the internal lattice variations as well as the grain boundary curvature with much improved spatial resolution. However, this is outside the scope of the present thesis work since the focus was on recrystallization.

The DFXRM technique has been developed at beamline ID06 at the European Synchrotron Facility (ESRF) in Grenoble during the last six years. In a collaborative effort between DTU and ESRF a dedicated instrument was commissioned at the beginning of 2017. During my PhD study I participated in the formulation of a geometrical optics based description of the microscope (see list of publications). This work is briefly discussed in relation to the instrument, but is otherwise outside the scope of this Thesis.

The thesis work is the first application of DFXRM within recrystallization. The aim has been to address open questions regarding the structure and dynamics in partly recrystallized specimens. In particular, focus has been on mapping the intragranular structure of recrystallizing grains and a method for mapping the few remaining defects in terms of local dislocation densities has been developed. Furthermore, the evolution of the subgrain structure in the deformed matrix has been investigated. Data acquisition strategies and data analysis procedures have been established and results are discussed in connection to the current understanding within the field.

This thesis is comprised of the following parts:

Chapter 2. Background Gives a brief overview of the necessary background material, including a theoretical description of dislocations and a metallurgical description of recrystallization, as well as the basics of x-ray diffraction.

Chapter 3. Dark Field X-Ray Microscopy Gives a introduction to the experimental setup and a walk-through of the beamline ID06 at ESRF alongside a theoretical description of different aspects of x-ray microscopy including data analysis.

Chapter 4. Recrystallizing grains with interior structure Presents the results from the first application of DFXRM to map in 3D the interior mosaicity and strain in bulk recrystallizing grains, including a discussion of data analysis and interpretation.

Chapter 5. Recovery kinetics of individual subgrains Presents the results from the in situ annealing study of subgrains in the deformed structure by means of a new method, in which the evolution of hundreds of individual subgrains are tracked during annealing.

Chapter 6. Outlook Gives an overview of the problems discovered and ideas emerged during the thesis work.

Chapter 7. Conclusion

2 Background

This chapter provides an overview of the necessary background information for the thesis work and is divided in three sections. In the first section the properties of dislocations are described and their theoretically derived elastic fields are presented for later comparison with experimental observations. The second section gives an overview of the current understanding of recrystallization and a brief presentation of experimental results from the literature. The basics of x-ray imaging techniques are described in the third section with emphasis on applications in recrystallization.

2.1 Dislocations

The description of the structure and recrystallization of deformed metals involves the concept of dislocations as the carriers of deformation. In polycrystalline materials it is dislocation structures that accommodate the differences in lattice orientation between the individual crystallites and changes to the internal structure may be described in terms of single or collective dislocation motion driven by a lowering of the energy stored in the dislocation structure.

The scope of this section is to give an overview of the properties of stationary dislocations. The fields associated with straight dislocation lines and a simple example of a dislocation boundary are listed, with focus on the distortion fields to make the equations directly applicable to the data presented in later chapters. For a basic introduction to dislocation and lattice defects the reader is referred to textbooks such as [HullBacon2011].

2.1.1 Lattice defects

In a perfect crystal lattice of a single element the atoms form a periodic array with translational symmetry along all directions. The structure that is repeated throughout the lattice is called the unit cell and may be composed of one or more atoms. In real lattices the long range translational symmetry is broken by different kinds of defects.

Several kinds of point defects are possible: A single lattice site may be occupied by an atom of a different element (substitution), the atom at a lattice site may be missing (vacancy), or an additional atom may occupy the space between lattice sites (interstitial). The number and arrangement of these depend

on the chemical composition and temperature. At finite temperature point defects are present even in otherwise perfect crystals.

To achieve a lasting external shape change of a crystal the lattice must be plastically deformed and thus the atoms in the lattice must shift with respect to each other. The shift is assisted by line defects moving through the crystal along certain lattice planes. These dislocation lines can only end at grain boundaries or external boundaries (or merge or split up at intersections), therefore bulk dislocations always form loops or networks. Dislocations are characterised by a line vector $\vec{\xi}$ pointing along the dislocation line and the Burgers vector $\vec{b}$ which is the closure failure on following the lattice around the dislocation perpendicular to the line vector. The Burgers vector is coincident with a close-packed direction of the lattice.

If a (piece of) dislocation line has $\vec{\xi} \perp \vec{b}$ the defect is called a pure edge dislocation. This is equivalent to the dislocation line being the edge of an extra lattice plane inserted in the crystal. Likewise, a pure screw dislocation has $\vec{\xi} \parallel \vec{b}$, equivalent to the lattice planes being displaced by one layer along the dislocation line, see Figure 2. Any dislocation line may be decomposed into a screw and an edge component. If a dislocation line meets another dislocation line with the same $\vec{\xi}$ but opposite $\vec{b}$, they may annihilate.

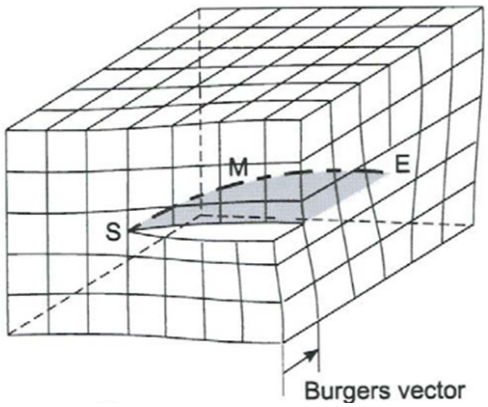

Figure 2: **Dislocation line** At S the dislocation is a pure screw dislocation and at E a pure edge. In between at M the dislocation has a mixed character and may be decomposed into a screw and an edge component. The line vector is parallel to the tangent of the dislocation line and the Burgers vector is constant and indicated in the Figure. From [HullBacon2011].

Dislocation motion occur as glide along slip-planes, which are the close-packed planes that contain both the line vector and the Burgers vector. For a screw dislocation there are several slip-planes and therefore cross-slip can occur in which the dislocation motion changes from one slip-plane to another. Furthermore, edge dislocations may climb in a plane perpendicular to $\vec{b}$ by the aid of vacancies, therefore climb is thermally activated.

For a dislocation to move a force must be applied to the slip-plane in the form of lattice stresses. This stress may be applied externally as in deformation or be present in the crystal in the form of other defects and elastically deformed regions. The latter is driving recrystallisation and is thermally activated. Dislocations are often pinned by other defects, for example when entangled in cell-wall, or locked in a network, see Figure 3. The former gives rise to short-ranged barriers that may be overcome by thermal activation, whereas the latter gives rise to long-range fields that pin dislocations also at elevated temperatures.

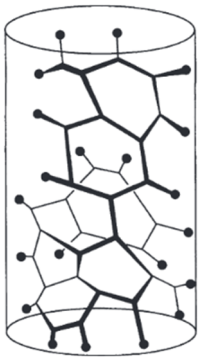

Figure 3: **Frank network** In a well-annealed crystal the remaining dislocations may form a network as sketched here. From [HullBacon2011]

2.1.2 Dislocations in *fcc*

In this thesis focus is on aluminium which has a face-centered cubic (*fcc*) lattice structure. The unit cell consists of a cube with extra lattice sites at all faces, see Figure 4. The close-packed planes are the 211 and the close-packed directions are the $\langle 110 \rangle$. Thus the Burgers vector may be any of the 12 vectors $\frac{1}{2}\langle 110 \rangle$. Due to the alternating lattice structure along [110], an edge dislocation in an *fcc* lattice is actually equivalent to the introduction of two extra lattice planes. This opens the possibility of the dislocation splitting up into two Shockley partials

and a stacking fault area between them. However, the separation between the two partials is expected to be small in aluminium because of the large stacking fault energy.

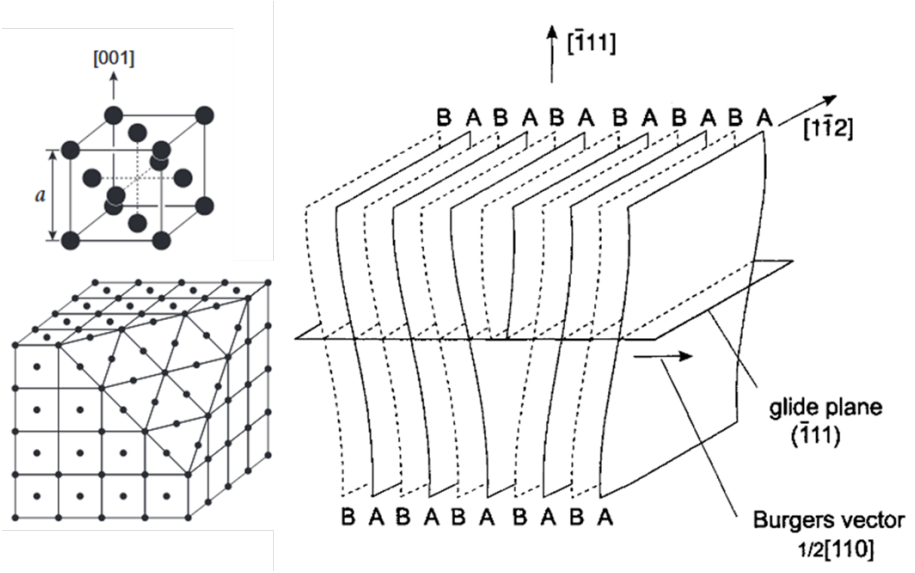

Figure 4: ***fcc* crystal structure and dislocations** Unit cell and arrangement of atoms in the periodic *fcc*-lattice. Orientation of Burgers vector and glide plane with respect to crystallographic axes. From [HullBcon2011].

Any plastic deformation in the sense of dislocations is associated with elastic deformation. The presence of a dislocation line gives rise to long range stress fields that falls off inversely proportional to the distance to the dislocation line (see mathematical expressions below). Dislocations interact through these fields and attract or repel each other, and the dislocations arrange into lower energy structures by shielding each others stress fields.

For example, similar dislocations of parallel Burgers vectors of length b may form low angle boundaries by lining up along a certain direction, see Figure 5. With an average dislocation spacing of D this arrangement will give rise to lattice misorientation across the low angle boundary of:

$$\theta = \frac{b}{D} \tag{1}$$

The current understanding of plastic deformation in terms of dislocations is based on the pioneering work by Volterra [Volterra1907], Taylor [Taylor1934],

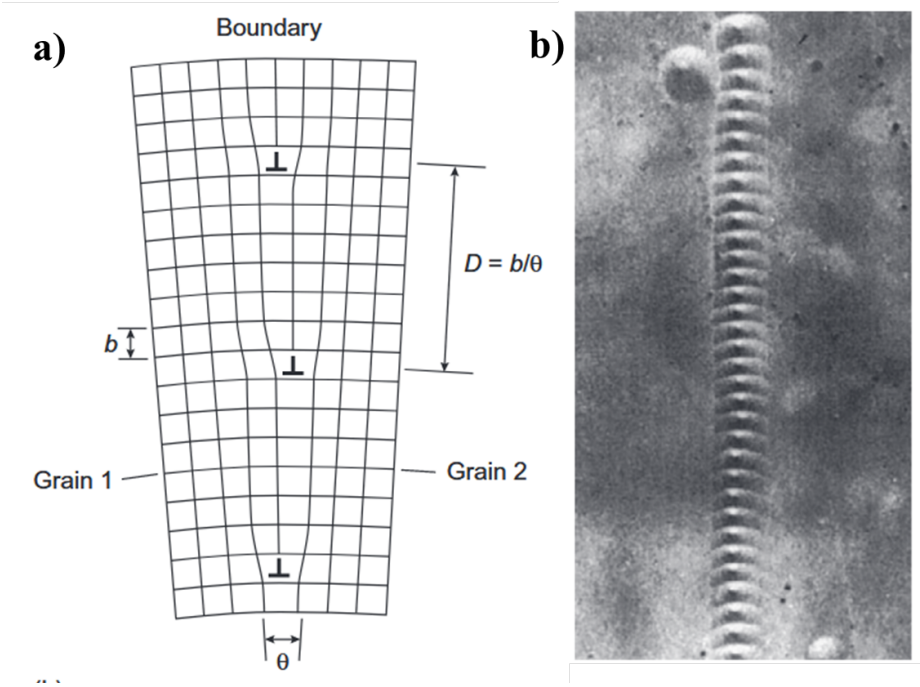

Figure 5: **Dislocation boundary** a) Symmetric tilt boundary consisting of evenly separated parallel edge dislocations of identical Burgers vector. b) Evenly spaced etch pits at the boundary between two grains indicate the presence of a symmetric tilt boundary. From [Bacon2011, Vogel1953].

Orowan [Orowan1934], Polanyi [Polanyi1934], and others, and with the development of experimental techniques for visualising dislocations and dislocation structures, the theory was confirmed.

2.1.3 Visualising dislocation

There are several well-established methods for visualising dislocations. The first direct evidence of the presence of dislocations was obtained by etching the surface of a deformed crystal, see Figure 5, utilizing that etch pits form where a dislocation line meets the surface because the atoms are easier to remove here [Vogel1953]. It is even possible to track the motion of endpoints of the dislocation lines utilizing that the lattice regains its strength as the dislocation moves away so that the etch pit at this point does not grow deeper.

Stable dislocation structures may be visualised directly using optical microscopy if the dislocations are dressed by impurity atoms, or in some cases

under crossed polarisers.

Nowadays the vast majority of dislocation imaging is carried out using transmission electron microscopy (TEM). Electrons are diffracted by a periodic lattice according to Bragg's law in much the same way as x-rays (see below) and dislocation lines appears in the TEM-images due to the slight deviations in lattice orientation associated with dislocation line. The electron microscope has a sub-nanometre spatial resolution, but as the name indicates, the electrons are transmitted, which limits the sample size to a μm-thick wafer. Nevertheless, beautiful images of dislocations and dislocation structures are obtained using TEM, see Figure 6, and due to short acquisition times the motion of single dislocations and dislocation boundaries may be filmed. Three-dimensional imaging is possible, but only for thin samples. Furthermore, in a modified version know as high-resolution TEM (HREM) it is possible to achieve sub-angstrom spatial resolution, which allow for imaging of the atomic structure of the lattice at the site of the dislocation, see Figure 6.

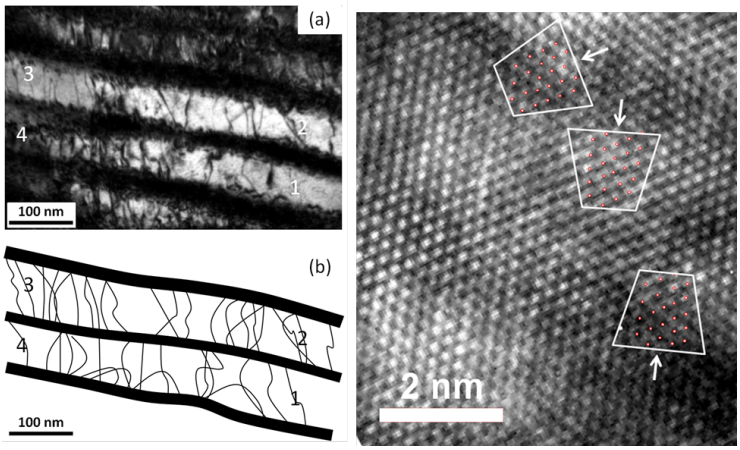

Figure 6: **TEM and HREM images of dislocations** Left: Transmission electron micrograph (TEM) of single dislocations in ferrite lamellae. From [Zhang2011]. Right: HREM of the atomic structure of single dislocations in a low angle boundary. From [Zhang2016].

Electron backscatter diffraction (EBSD) is widely used for determining misorientations as a measure of the stored energy due to the dislocation content but does not have the sufficient resolution to visualize single dislocations. In a similar manner to TEM, x-ray topography (see below) enables direct imaging of single dislocations in thicker samples provided the dislocation density is low,

since individual dislocation lines appear several micrometers wide. To be able to quantify observations in terms of lattice distortion and variations in orientation and strain, a model for the fields around dislocation lines are necessary, and this is addressed in the following.

2.1.4 Stress and strain

The theoretical derivation of the stress and distortion fields associated with individual dislocations is a chicken-and-eggs questions. We may consider the fields to be continuous and turn to elasticity to derive expressions for the fields to afterwards place the distorted lattice sites so that the energy is minimized. However, the fields are only there because the lattice is distorted around the dislocation line, and we could as well place the lattice sites first and from this determine the fields, as is done in simulations such as DFT. Furthermore, the lattice is heavily deformed at the dislocation core, therefore the small strain approximation usually applied in elasticity is not valid here. Nevertheless, the fields given below are derived in a linear elasticity approximation, since for DFXRM studies the collective lattice properties and not the position of individual atoms are of interest.

2.1.5 Displacement and distortion

Deformation of a crystal may be described in terms of a displacement field $\vec{U}$ which measures the deviation from perfect crystal structure. Then the distortion tensor is defined as the gradient of the displacement, $\beta = \nabla\vec{U}$, or in terms of components, where ∂_i denotes the partial derivative with respect to the ith coordinate:

$$\beta_{ij} = \partial_j U_i \tag{2}$$

Since the line integral of a gradient around any closed loop is zero it is implied that:

$$\oint \beta \cdot d\vec{l} = 0 \tag{3}$$

2.1.6 Nye tensor and Burgers vector

For a plastically deformed sample the part of the displacement due to plastic deformation, $\vec{u}^p$, is in general not known and only the local elastic part, $\vec{u}^e$, is

accessible from the structure. Thus with $\vec{U} = \vec{u}^p + \vec{u}^e$ gradient integral may be rewritten as:

$$\oint \beta^e \cdot d\vec{l} = -\oint \beta^p \cdot d\vec{l} = \int_A \alpha \cdot d\vec{a} \tag{4}$$

To obtain the latter equality Stokes theorem was applied and the Nye tensor defined as $\alpha = \nabla \times \beta^e$ was introduced. The components of the Nye tensor are given by:

$$\alpha_{ij} = -\varepsilon_{jkl}\partial_k \beta^e_{il} \tag{5}$$

Here ε_{ijk} denotes the Levi-Cevita permutation symbol which is 1 for an even number of permutations of $ijk = 123$, -1 for odd, and zero for all other combinations of possible indices. Summation over repeated indices is implied from the Einstein notation. For α to be non-zero there must be a non-gradient contribution to β^e, since the curl of a gradient is identically zero. This lattice incompatibility is the signature of dislocations, and α is related to the dislocation density [Kröner1958, Nye1953]. From the definition of the Nye tensor it is evident that $\nabla \cdot \alpha = 0$. The Burgers vector $\vec{b}$ is related to the Nye tensor as:

$$\vec{b} = \int_A \alpha \cdot d\vec{a} \tag{6}$$

Superscripts are omitted in the following since all fields mentioned below are associated with the elastic deformation. The distortion tensor may be decomposed into a symmetric strain ϵ and a skewsymmetric rotation ω, such that $\beta = \epsilon + \omega$ with $\epsilon_{ij} = \frac{1}{2}(\beta_{ij} + \beta_{ji})$ and $\omega_{ij} = \frac{1}{2}(\beta_{ij} - \beta_{ji})$. It is assumed that all β-components are small everywhere such that the problem may be linearised and that the crystal is isotropic such that Hooke's law apply for the relation between the stress σ and strain:

$$\sigma = 2\mu\epsilon + \lambda \mathrm{I}\mathrm{Tr}\epsilon \tag{7}$$

Here μ and λ are the material specific Lamé coefficients, which are related to the Poisson ratio as $\nu = \lambda/2(\lambda + \mu)$ and to the shear modulus as $G = \mu$.

Then the fields may be derived from the compatibility relations

$$\nabla \cdot \sigma = 0 \tag{8}$$

together with the boundary condition that all fields vanish far away from the dislocation line. Depending on the method, additional compatibility relations for the moments are also needed. From DFXRM-measurements components of the distortion tensor are obtained and components of the Nye tensor may be

derived, see the description in Chapter 3. Therefore, in the following only these fields and not the stress and strain fields are stated.

2.1.7 Far field solution

Introducing a singular dislocation density, where superscripts e and s denotes edge and screw dislocation, respectively,

$$\alpha^e_{xz} = \frac{b}{2\pi}\delta(r) \tag{9}$$

$$\alpha^s_{zz} = \frac{b}{2\pi}\delta(r) \tag{10}$$

or by simple inspection of the geometry of the dislocation, stress and displacement fields may be derived (the derivations and/or fields are found in textbooks on dislocations, e.g.[Weertman1992, HullBacon2011]). These fields are singular at the location of the dislocation line and therefore the solution is only valid outside the dislocation core, typically taken to be around $5b$ in radius where b is the length of the Burgers vector. For straight, infinite screw dislocations with $\vec{\xi} \parallel \hat{z}$ the non-zero components of the distortion tensor are given by:

$$\beta^s_{zx} = -\frac{b}{2\pi}\frac{y}{r^2} \tag{11}$$

$$\beta^s_{zy} = \frac{b}{2\pi}\frac{x}{r^2} \tag{12}$$

Here $r = \sqrt{x^2+y^2}$ and $\vec{b} = b\hat{z}$. Likewise, for edge dislocations parallel to the z-direction and with $\vec{b} = b\hat{x}$ the distortion is given by:

$$\beta^e_{xx} = B\frac{x}{r^2}\left[2\nu - \frac{3x^2+y^2}{r^2}\right] \tag{13}$$

$$\beta^e_{yy} = B\frac{y}{r^2}\left[2\nu + \frac{x^2-y^2}{r^2}\right] \tag{14}$$

$$\beta^e_{xy} = -B\frac{x}{r^2}\left[2\nu - \frac{3x^2+y^2}{r^2}\right] \tag{15}$$

$$\beta^e_{yx} = B\frac{y}{r^2}\left[2\nu - \frac{x^2+3y^2}{r^2}\right] \tag{16}$$

Here $B = b/4\pi(1-\nu)$ where ν denotes the Poisson ratio and all elements that are not mentioned are zero. The fields decrease as $1/r$ away from the dislocation line.

2.1.8 Non-singular solution

The singularity may be removed by several different approaches for example gauge theory [Lazar2003], strain gradient elasticity [Gutkin1999], or non-symmetric stress theory [Nowacki1986]. The resulting equations and fields are similar and here we give the solutions stated in [Lazar2003]:

$$\beta^s_{zx} = -\frac{b}{2\pi}\frac{y}{r^2}\left[1-\kappa_1(r)\right] \quad (17)$$

$$\beta^s_{zy} = \frac{b}{2\pi}\frac{x}{r^2}\left[1-\kappa_1(r)\right] \quad (18)$$

$$\beta^e_{xx} = -B\frac{y}{r^2}\left[(1-2\nu)+\frac{2x^2}{r^2}+\frac{y^2-3x^2}{r^2}\kappa_2(r)-2\left(\frac{y^2}{r^2}-\nu\right)\kappa_1(r)\right] \quad (19)$$

$$\beta^e_{yy} = -B\frac{y}{r^2}\left[(1-2\nu)-\frac{2x^2}{r^2}-\frac{y^2-3x^2}{r^2}\kappa_2(r)-2\left(\frac{x^2}{r^2}-\nu\right)\kappa_1(r)\right] \quad (20)$$

$$\beta^e_{xy} = B\frac{x}{r^2}\left[(3-2\nu)-\frac{2y^2}{r^2}-\frac{x^2-3y^2}{r^2}\kappa_2(r)-2\left((1-\nu)+\frac{y^2}{r^2}\right)\kappa_1(r)\right] \quad (21)$$

$$\beta^e_{yx} = -B\frac{x}{r^2}\left[(1-2\nu)+\frac{2y^2}{r^2}+\frac{x^2-3y^2}{r^2}\kappa_2(r)-2\left((1-\nu)-\frac{y^2}{r^2}\right)\kappa_1(r)\right] \quad (22)$$

Here $\kappa_1(r) = krK_1(kr)$, $\kappa_2(r) = \frac{4}{k^2r^2} - 2K_2(kr)$, $B = b/4\pi(1-\nu)$ and all elements that are not mentioned are zero. The additional terms involve the modified Bessel functions of the second kind $K_n(kr)$ and a parameter k which is related to the length scale of the additional terms. The modified non-singular fields reduce to the far field solution away from the dislocation but vanish at the position of the dislocation line. Therefore the Nye tensor and thus the dislocation density are altered in the core region:

$$\alpha^e_{xz} = \frac{bk^2}{2\pi}K_0(kr) \quad (23)$$

$$\alpha^s_{zz} = \frac{bk^2}{2\pi}K_0(kr) \quad (24)$$

Consequently, the modified Burger's vectors for edge and screw dislocations are, respectively:

$$b^e_x = b\left[1-krK_1(kr)\right] \quad (25)$$

$$b^s_z = b\left[1-krK_1(kr)\right] \quad (26)$$

The value of k cannot be derived directly from the models and must be determined experimentally. The distortion field components of a screw dislocation are shown in Figure 7 and of an edge dislocation in Figure 8 with $\nu = 0.3$ and $k = 1/b$.

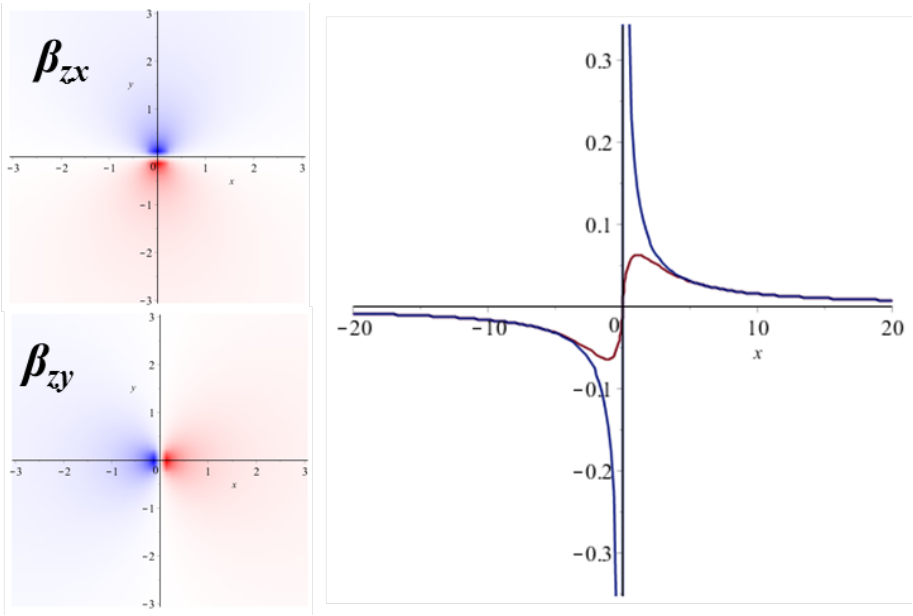

Figure 7: **Distortion of a screw dislocation** The two non-zero distortion tensor components associated with a pure screw dislocation are plotted according to the non-singular solution. The dislocation line as well as the Burgers vector are parallel to the z-direction (out of the page). The saturation of the color indicates field strength with negative values in blue, positive values in red, and zero given in white. The axes are given in units of $100b$. The cross-sections for β_{zy} through the dislocation center along x (horizontally) show a comparison of the far field solution (blue) and the non-singular solution (red).

2.1.9 Dislocation arrays and low angle boundaries

In the linear approximation the resulting fields associated with a collection of N parallel dislocation lines are given by the sum of the individual fields centered at the position of the individual dislocation lines:

$$\beta_N = \sum_{n=1}^{N} \beta_n \tag{27}$$

$$\alpha_N = \sum_{n=1}^{N} \alpha_n \tag{28}$$

However, since the fields of the individual dislocations were derived given the assumption that the fields vanish at infinity, one should be careful to make sure the original boundary condition is still fulfilled in the case of many dislocations

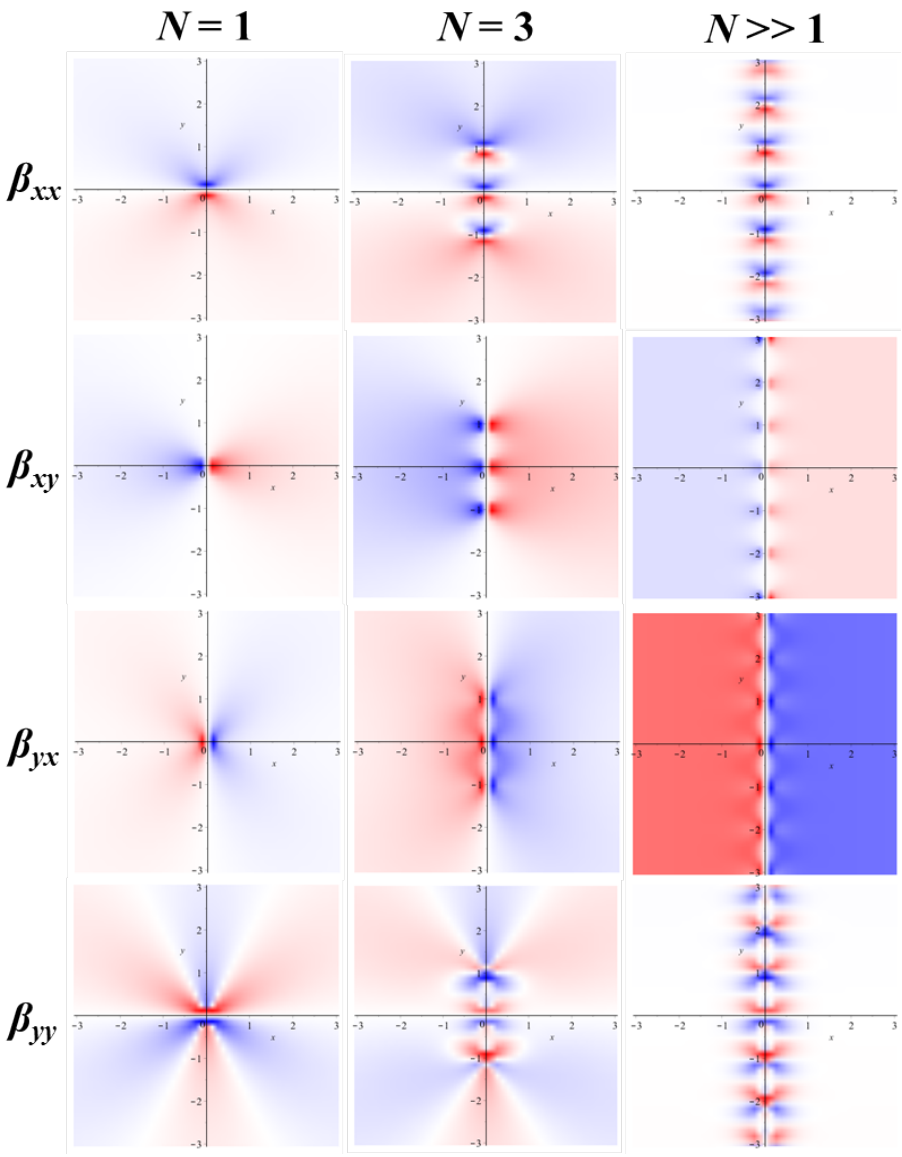

Figure 8: **Distortion of an edge dislocation and simple dislocation boundary** The four non-zero distortion tensor components associated with a pure edge dislocation are plotted according to the non-singular solution. The dislocation line is parallel to the z-direction (out of the page) and the Burgers vector parallel to the positive x-direction (horizontal). The saturation of the color indicates field strength with negative values in blue, positive values in red, and zero given in white.

scattered over a large volume.

The arrangement of dislocations is not random as they align to minimize the total energy [Wilsdorf1999], which gives rise to periodic structures such as dislocation boundaries in the case of identical parallel dislocation lines. For example a low angle boundary consisting of N identical edge dislocations parallel to the z-direction and evenly spaced along the y-direction with spacing D gives rise to the distortion fields shown in Figure 8 for $N = 5$ and $N \to \infty$, under the assumption that the boundary conditions are fulfilled. The fields oscillate along the boundary with a period given by the dislocation spacing and change sign across the boundary.

This non-singular representation of dislocations in terms of distortion fields derived within an elasticity model provides the mathematical framework for interpretation of DFXRM measurements in terms of dislocations as the carriers of deformation. This connection is established in Chapter 3 and applied in Chapter 4, but first the basics of recrystallization and x-ray imaging are introduced.

2.2 Recrystallization

This section gives a brief overview of the prevalent view of static recrystallization of deformed metals. For completeness, a description of deformation and recovery processes and the resulting structures typically occurring prior to recrystallization is given. Furthermore, the section is concluded with a mention of grain growth in the fully recrystallized structure.

The current understanding of the mechanisms involved has been established on a mainly empirical foundation as the structure and its dynamics and spatial variations are extremely complex. An overview of stages and structures during annealing is shown in Figure 9 and explanations follow below. For a thorough description of recovery and recrystallization the reader is referred to the many textbooks on the subject, for example Humphreys and Hatherly [HH2004] or [Haessner1978].

2.2.1 Deformation and recovery

Plastic deformation alters the shape of the sample and introduces defects and dislocations into the crystal lattice. Thus during deformation processes such as rolling or drawing individual crystalline grains in a polycrystalline sample change shape, orientation, and dislocation content. For moderate degrees of deformation the original grain boundaries of the deformed grains change shape and orientation but remain still discernible. After deformation a large orientation spread (typically up to 5-10 degrees for 50% cold-rolled aluminium) is present within the deformed grains, which were single crystalline before deformation.

The as-deformed structure of a metal consists of many entangled dislocations. In cell-forming metals such as aluminium the dislocations organize during deformation to form cells of lower dislocation density separated by fuzzy cell-walls of higher dislocation density. The cell structures are arranged in cell-blocks separated by walls of even higher dislocation density, the geometrically necessary dislocation walls, which again may be ordered in various bands, see Figure 10. Many experimental studies have been dedicated to the mapping and/or characterization of the deformed structure of different metals and alloys. An example of a TEM-image of the cell-block structure found in cold-rolled high purity aluminium is shown in Figure 11.

Energy is stored in the deformed structure since no matter how the atoms arrange themselves they cannot form a perfect lattice due to the presence of

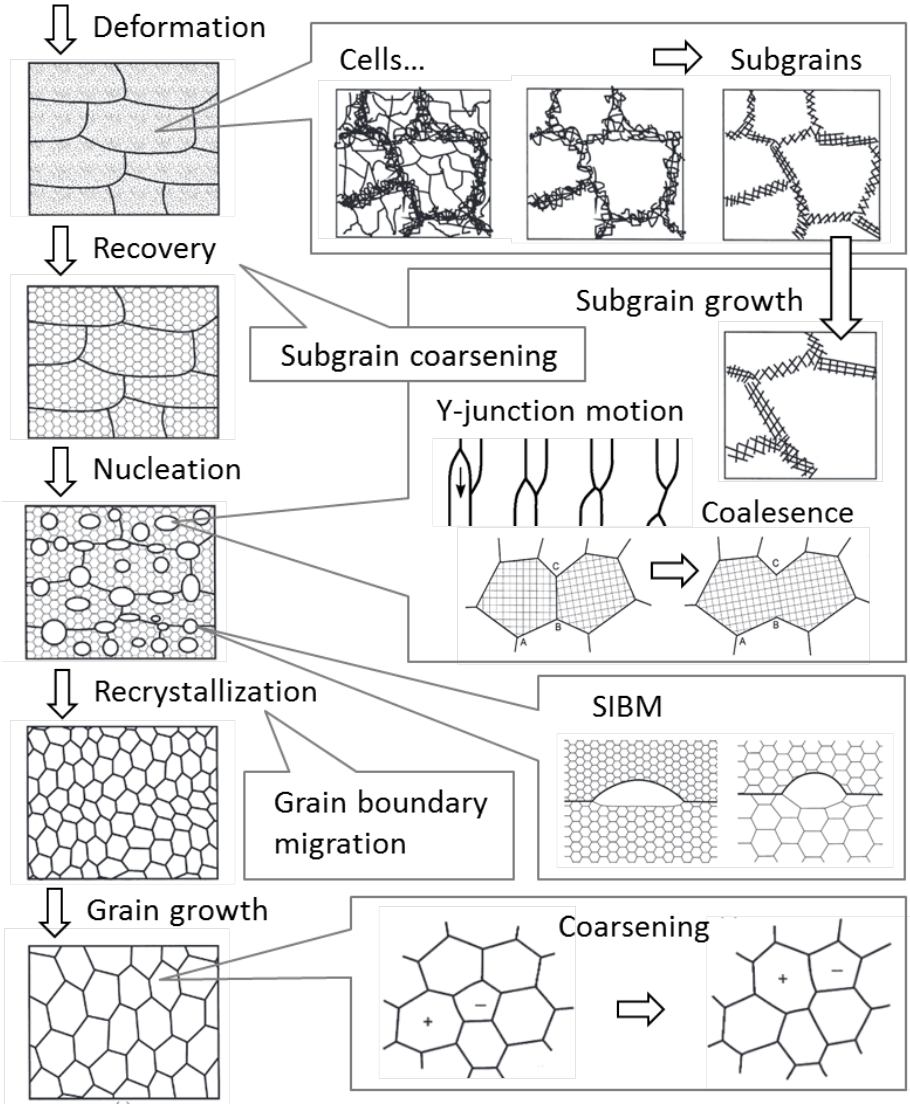

Figure 9: **Overview of processes during annealing** The cell structure of the deformed specimen recovers to a more ordered subgrain structure during deformation and/or initially during annealing. At sufficient temperature nucleation onsets recrystallization and several possible mechanisms may be considered including subgrain growth by boundary migration, triple-junction motion or coalescence in the interior of deformed grains, and strain induced grain boundary migration (SIBM) at sites where high angle boundaries are present. During recrystallization the nuclei grow into the deformed matrix and eventually the specimen is fully recrystallized. Then follows grain growth, the coarsening of the recrystallized grain structure. Adapted from [HH2004, Yu2015]

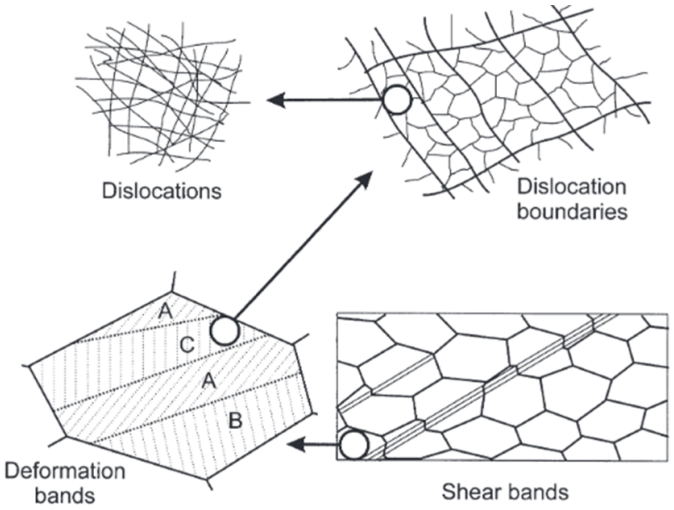

Figure 10: **Deformed structure** Dislocations are introduced during deformation and the structure is altered at different length scales with shear bands through the whole polycrystal, deformation bands in individual grains, and dislocation boundaries and dislocations at the smallest scale. From [HH2004]

dislocations. However, the stored energy may be minimized if the dislocations arrange themselves so that they shield each others stress fields (or potentially annihilate). Dislocation motion is facilitated by increasing the temperature, thus during annealing dislocations gather in the cell or subgrain walls. Here opposite dislocations annihilate and dislocation lines organize in structures of higher order to lower the stored energy, see the top row of images in Figure 9. The resulting structure consists of subgrains of low dislocation density separated by well-ordered boundaries. The low angle boundaries lie in certain planes and their structure may be characterized by means of TEM [Hong2013], see Figure 11.

In Figure 1 in Chapter 1 regions containing subgrains are visible in the EBSD-map of the partly recrystallized structure of a specimen from the same batch of cold-rolled aluminium AA1050 as is studied in the present thesis work.

From bulk properties such as heat capacity or hardness measured as a function of annealing temperature at constant heating rate it is inferred that there are two distinct temperature regions with different dynamics, see Figure 12 where measurements for aluminium deformed by compression to 75% and an-

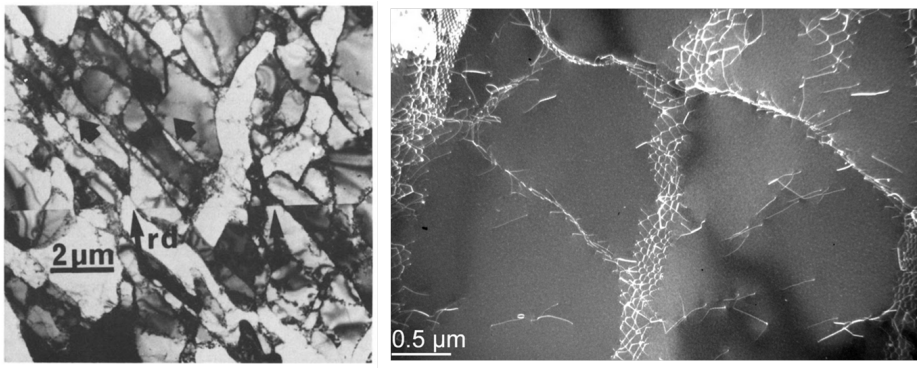

Figure 11: **Deformed structure** TEM-images of deformed structures in aluminium. Left: Cell-blocks in 50% cold-rolled high purity aluminium. From [BayHansen1992]. Right: Well-ordered subgrain boundaries in 10% cold-rolled high purity aluminium. Analysis of the structure of the dislocation network in given in [Hong2013]. Image courtesy of C. Hong.

nealed at constant heating rate are shown. The first region is at low annealing temperature, 100 - 250°C and is identified with recovery, whereas the more sharply peaked second region identified with recrystallisation is onset at 250°C and peaked at 325°C.

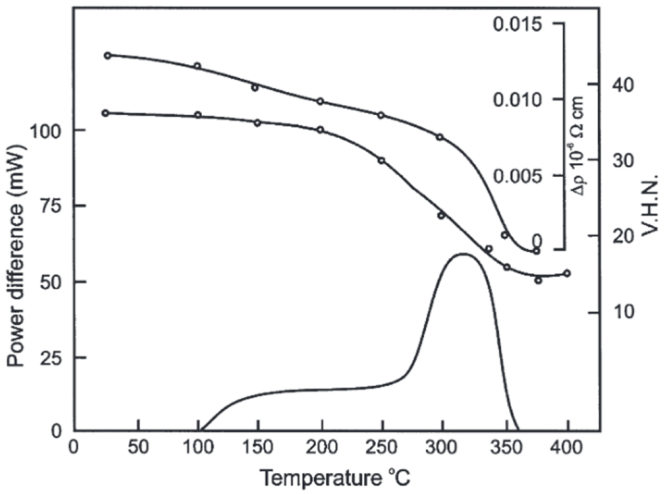

Figure 12: **Bulk measurements** The recovery of 99.998% aluminium deformed to 75% in compression, measured by calorimetry, electrical resistivity, and hardness. The heating rate was 6°C/min. From [HH2004].

2.2.2 Subgrain growth and coarsening during recovery

The average subgrain size and thus the characteristic length scale increases during recovery, therefore single dislocations or dislocation boundaries must be moving. Like the dislocation velocity, the velocity per boundary area of a migrating boundary is given by $v = MP$ from reaction rate theory where M is the boundary mobility and P is the pressure on the boundary. This relation has been verified experimentally in most cases tested.

The driving force given as a pressure P on a subgrain boundary of curvature $1/R$ is the reduction of stored energy as the boundary moves [HH2004]:

$$P = -\alpha R \frac{d}{dR}\left(\frac{\gamma_s}{R}\right) \tag{29}$$

Here γ_s is the surface energy of the boundary and α is a constant. In the case of constant surface energy during migration this reduces to the Laplace pressure $P = \alpha\gamma_s/R$. This is valid if the misorientation across the boundary remains unchanged during boundary migration since the surface energy γ_s of such low angle boundaries is given by the Read-Shockley equation:

$$\gamma_s = \gamma_0\theta(A - \ln\theta) \tag{30}$$

Here $\theta = b/D$ is the misorientation of the lattice across a boundary consisting of parallel dislocations of Burgers vector b and spacing D, $\gamma_0 = Gb/4\pi(1-\nu)$, and A is related to the dislocation core energy. For small angles the expression is reduced to $\gamma_s = c_2 Gb\theta$ with constant c_2.

If for low angle boundaries the migration may be described in terms of the motion of individual dislocations the mobility is suggested to be [ØrsundNes1989]:

$$M = \frac{c_1 D_s b}{kT} \tag{31}$$

Here c_1 is a constant of order unity and D_s is the coefficient of self-diffusion, b is the length of the Burgers vector of the dislocations in the boundary, k is the Boltzmann constant, and T is the absolute temperature. It is assumed that the migration is thermally activated and may be described in terms of diffusion of atoms from one subgrain to the neighbour through the subgrain boundaries.

Combining the above the velocity of a migrating low angle boundary is inversely proportional to both the annealing temperature and the radius of curvature of the boundary:

$$v = C\frac{GbD_s\theta}{kTR} \tag{32}$$

The constant pre-factor is given by $C = \alpha c_1 c2$.

In reality, this model should be modified by an onset pressure because dislocations and boundaries are pinned by impurities, and other defects and dislocation structures such that $v = M(P - P_0)$.

A similar relationship may be derived for a dislocation structure of characteristic length scale $\bar{R}$, where the velocity may be interpreted as the change to this characteristic length, such that $v = d\bar{R}/dt$. For example for a Frank network of mesh size $\bar{R}$ where the boundary migration is governed by climb of single dislocations the velocity depends on the concentration of jogs c_j on the dislocation lines [Friedel1964]:

$$\frac{d\bar{R}}{dt} = \frac{D_s c_j G b^3}{2kT\bar{R}} \tag{33}$$

Assuming the subgrains behave like grains (see below) and the structure may be described as an assembly of spherical grains the growth rate of individual subgrains is given by [Hillert1965]:

$$\frac{dR}{dt} = M\gamma_s \left(\frac{1}{R_c} - \frac{1}{R} \right) \tag{34}$$

Thus with the critical size R_c it is expected that small subgrains with $R < R_c$ will shrink and larger ones will grow.

From geometrical considerations it is predicted that growth is related to the number of sides or triple junctions n of each subgrain since the equilibrium situation is expected to be that of zero boundary curvature and 120°angles at triple junctions. The von Neumann-Mullins formula [vonNeumann1952, Mullins1956] for the development of grain area A in a 2D structure of uniform surfaces with surface tension γ and mobility M states that:

$$\frac{dA}{dt} = -2\pi M\gamma \left(1 - \frac{n}{6} \right) \tag{35}$$

Thus subgrains with $n < 6$ will shrink and subgrains with $n > 6$ will grow as indicated in the bottom right of Figure 9. Larger subgrains have larger boundary area and therefore are more likely to have more than six neighbours. The 2D structure is stable when all subgrains have $n = 6$ and all boundary curvatures are zero, that is for a grid of identical hexagons. This formula was recently generalized to 3D structures [MacPherson2007], however, 3D space cannot be filled with identical polygons, therefore in principle coarsening continues until only one (sub)grain remains.

In reality, the subgrain structure is much more complex with huge variations in boundary energy due to large local structural variations in the deformed microstructure. Therefore optimal angles at triple points may differ markedly from 120°, and other effects such as triple junction motion should be taken into account, especially in specimens deformed to high strain, see Figure 13 [Yu2015].

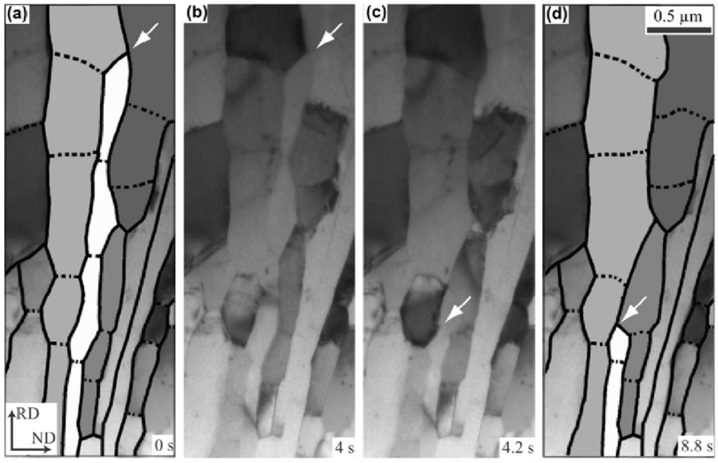

Figure 13: **Triple junction motion** TEM-images of rapid motion of triple junctions in aluminium AA1050 cold-rolled to a true strain of 5.5 during annealing at 320 °C. From [Yu2015].

Another possible but not experimentally confirmed mechanism of subgrain coarsening is the coalescence of two neighboring subgrains, see Figure 9. Subgrain are assumed to rotate within the matrix of soft dislocation boundaries to match the orientation of the neighboring subgrain and merge [Hu1963]. Also, single dislocation lines from the boundaries or the interior of the subgrain may sweep through the subgrain and there altering its orientation and strain slightly.

Besides the subgrain size and current temperature the boundary migration is also affected by internal strain, point defects and small impurities which pin the otherwise moveable dislocations as well as the nature of the subgrain boundaries. The properties of boundaries are observed to vary markedly with misorientation, boundary dislocation structure, subgrain orientation and material and it is at current not possible to predict the evolution of a given subgrain structure [HH2004].

2.2.3 Nucleation

Upon annealing at sufficiently large temperatures new nuclei may develop in the recovered structure and thereby initiate recrystallization, see Figures 9 and 12. Nuclei grow to a size considerably larger than the average subgrain size, which according to the models described above markedly increases the likelihood of that particular nucleus growing further and becoming a recrystallizing grain.

It has been found that nucleation happens more often at intersection between grain boundaries of deformed grains or intragranular sites of large local misorietation such as shear bands and especially at triple points [Vandermeer1959]. A mechanism often observed to lead to nucleation is strain induced grain boundary migration (SIBM) in which a high angle boundary that separates two deformed regions migrates into the region of higher dislocation density and leaves behind a larger almost defect-free nucleus, see the central part of Figure 9. The driving force is the reduction of stored energy due to the decrease in bulk dislocation density ρ, since the bulk stored energy is $\propto \rho G b^2$ [HH2004].

Nuclei may also form as a result of the subgrain coarsening and growth as described above, which suggest that the initially largest cells or subgrains will grow the most and eventually become recrystallizing grains. However, at present it is not possible to predict which cells or subgrains become nuclei, since the number of possible geometries (combinations of lattice orientations and boundary/dislocation network configurations) is too large to allow first principle calculations. Moreover, direct experimental methods to guide and verify the modelling are absent. Electron microscopy and other invasive techniques are subject to a missing information problem since while nuclei can be identified and mapped it is not known what the structure was at the same position prior to the nucleation event.

In aluminium the nuclei form very early in recrystallization process and site-saturation is typical.

2.2.4 Growth of recrystallizing grains

All processes that occur during annealing are driven by a reduction in stored energy [HumphreysHaterly]. Grain growth of the fully recrystallized sample as well as the expected subgrain coarsening during recovery of highly deformed specimens in particular are both expected to be driven by the reduction of boundary energy under boundary migration. In contrast, recrystallization is

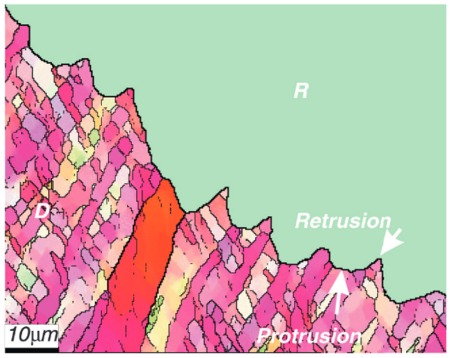

Figure 14: **Boundary migration of recrystallizing grain** The grain boundary of a recrystallizing grain is not smooth but posses protrusions and retrusions. The migration of the boundary depends not only on the difference in dislocation density by also on local boundary curvature and geometry. EBSD-map from [Moelan2013]

driven by a reduction in the stored energy in the bulk, and the driving pressure is proportional to the difference in defect density $\Delta\rho$ before and after boundary migration:

$$P = Gb^2\Delta\rho \tag{36}$$

The recrystallizing grains are assumed to be defect-free and $\Delta\rho$ is thus assumed to be equal to the density of dislocation in the deformed structure. The migration of a high angle boundary is thermally activated and the mobility is given by an Arrhenius type temperature dependence:

$$M = M_0 \exp\left(-\frac{Q}{kT}\right) \tag{37}$$

Here Q denotes the activation energy of the thermally activated migration and the pre-factor M_0 depends on the properties of the boundary in terms of orientation difference etc. Assuming that the dislocation density is constant in the immediate vicinity of a given recrystallizing grain of equivalent spherical radius R, the growth rate $v = dR/dt$ of the grain at constant annealing temperature is given by:

$$\frac{dR}{dt} = M_0 G b^2 \rho \exp\left(-\frac{Q}{kT}\right) \tag{38}$$

However, recent measurements [Moelans2013, Zhang2017] reveal that the external boundaries of the recrystallizing grain towards the subgrains of the deformed structure are not smooth, but possess protrusions and retrusions, see

Figure 14. Furthermore, the boundary regions move in a stop-go manner, which is possibly related to the morphology of the deformed structure adjacent to the boundary [Schmidt2004]. Thus the boundary migration depends not only on the difference in stored energy between the recrystallizing grain and the deformed matrix, but also on local boundary curvature as well as the local morphology of the deformed material and the differences in strain and orientation across the boundary.

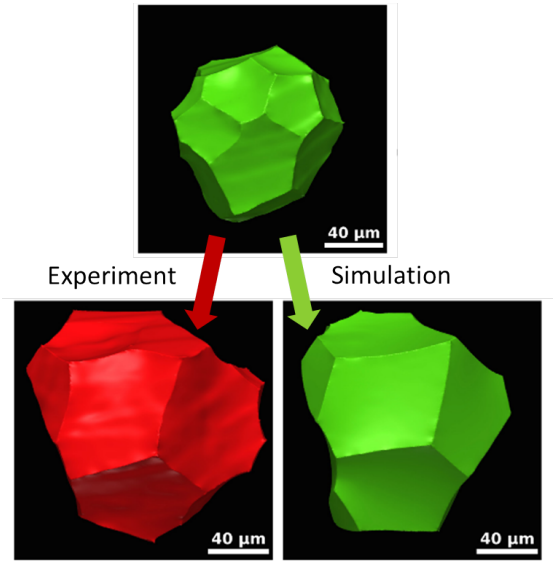

Figure 15: **Evolution of a single grain** A bulk grain in a recrystallized specimen of Ti-β-21S. a) Initial shape as measured by x-ray tomography. b) The final shape as measured. c) The final shape as determined by phase-field simulation. From [McKenna2014].

2.2.5 Grain growth

When recrystallisation is complete the structure is entirely made up of new recrystallized grains of very low dislocation density separated by sharp grain boundaries. The boundaries are relatively smooth and may be described mathematically in a purely geometrical sense with curvature, inclinations and intersections as the main features. The larger characteristic length scale of the structure allows for easy imaging and orientation mapping by EBSD and existing x-ray techniques (see below) and several numerical simulation techniques have been established based on for example vertex models, see e.g. [Lepinoux2010] and

phase-field models, see e.g. [Krill2002]. In particular, a grain structure mapped experimentally by x-ray tomography (see below) before and after annealing was taken as the input of a phase-field simulation and the output showed excellent agreement with the experimental observations [McKenna2014], see Figure 15.

2.3 X-ray properties and methods

The diffraction and absorption of x-rays have been exploited for more than a century resulting in the development of an impressive variety of different techniques from everyday crystal structure checks in the pharmaceutical industry or absorption x-ray images of teeth at the dentist to highly specialised research equipment for determining ever more complicated protein crystal structures, filming molecular dynamics in real-time or investigating the behaviour of materials under extreme conditions.

The new x-ray method, dark field x-ray microscopy (DFXRM), presented in this thesis belongs to the family of diffraction-based imaging-techniques which also include for example diffraction contrast tomography (DCT), three-dimensional x-ray diffraction (3DXRD), topo-tomography and scanning beam techniques such as differential aperture x-ray microscopy (DAXM). Thus the scope of this section is to provide a brief overview of the well-established experimental x-ray imaging techniques already developed for resolving the microstructure of polycrystalline samples. All techniques presented rely on hard x-ray synchrotron radiation to have high resolution at the appropriate length-scales as well as short acquisition times. The techniques are presented as applied to recrystallization. Examples from the literature are given and the advantages and shortcomings are discussed. As an introduction a short presentation of the basics of x-ray diffraction and absorption is given. For details on this topic the reader is referred to textbooks such as [Als2001, Warren1990].

2.3.1 X-ray scattering and diffraction

Consider a monochromatic x-ray beam of wavelength λ, corresponding energy $E = (12.398\text{keV}/\text{Å})/\lambda$ and incoming wave vector $\vec{k}_0$ of length $k_0 = 2\pi/\lambda$. X-rays are elastically scattered by electrons in atoms to have an outgoing wave vector of $\vec{k}$. The scattering vector is $\vec{q} = \vec{k} - \vec{k}_0$ and the scattering amplitude is given by a form factor $F(\vec{q})$ for the electrons. The total scattered intensity $I(\vec{q})$ is the norm-square of the scattering amplitude.

A collection of atoms at positions $\vec{r}_j$ of individual form factors $f_j(\vec{q})$ has the collective form factor:

$$F_c(\vec{q}) = \sum_j f_j(\vec{q}) e^{i\vec{q}\cdot\vec{r}_j} \tag{39}$$

The exponential phase factor gives rise to interference when the atomic structure is periodic. A crystal lattice is periodic with identical unit cells at all positions $\vec{R}_n = \sum_i n_i \vec{a}_i$ with integer n_i, where the lattice basis vectors are $(\vec{a}_1, \vec{a}_2, \vec{a}_3)$ and the position of the jth atom within the unit cell is represented by $\vec{r}_j$. The reciprocal lattice vector $\vec{G} = h\vec{b}_1 + k\vec{b}_2 + l\vec{b}_3$ with integer Miller indices (h, k, l) may be defined from the set of reciprocal lattice basis vectors:

$$\vec{b}_1 = 2\pi \frac{\vec{a}_2 \times \vec{a}_3}{\vec{a}_1 \cdot (\vec{a}_2 \times \vec{a}_3)} \tag{40}$$

$$\vec{b}_2 = 2\pi \frac{\vec{a}_3 \times \vec{a}_1}{\vec{a}_1 \cdot (\vec{a}_2 \times \vec{a}_3)} \tag{41}$$

$$\vec{b}_3 = 2\pi \frac{\vec{a}_1 \times \vec{a}_2}{\vec{a}_1 \cdot (\vec{a}_2 \times \vec{a}_3)} \tag{42}$$

$$\tag{43}$$

The unit cell volume is $V = \vec{a}_1 \cdot (\vec{a}_2 \times \vec{a}_3)$. From the definition it is seen that these vectors have the property:

$$\vec{a}_i \cdot \vec{b}_j = 2\pi\delta_{ij} \tag{44}$$

Each combination of Miller indices corresponds to a set of planes (hkl) with normal vector $\vec{a}_1/h + \vec{a}_2/k + \vec{a}_3/l$. For cubic unit cells of material specific side length a the separation between planes is given by:

$$d = \frac{a}{\sqrt{h^2 + k^2 + l^2}} \tag{45}$$

The position of any atom in the lattice may be described by a vector $\vec{R}_n + \vec{r}_j$. Thus the phase of the scattering amplitude split into a part for the unit cell and a part for the periodicity, and the scattering amplitude $F(\vec{q})$ becomes:

$$F(\vec{q}) = F_c(\vec{q}) \sum_n e^{i\vec{q}\cdot\vec{R}_n} \tag{46}$$

Due to the periodicity of the lattice and the position of the atoms, the sum over all lattice points vanishes unless the scattering vector is coincident with a reciprocal lattice vector:

$$\vec{q} = \vec{G} \tag{47}$$

This is the Laue condition for diffraction. An equivalent formulation of diffraction is the Bragg law which states that a reflection occurs at the scattering angle 2θ for lattice planes of separation d such that the following relation is fulfilled:

$$\lambda = 2d \sin\theta \tag{48}$$

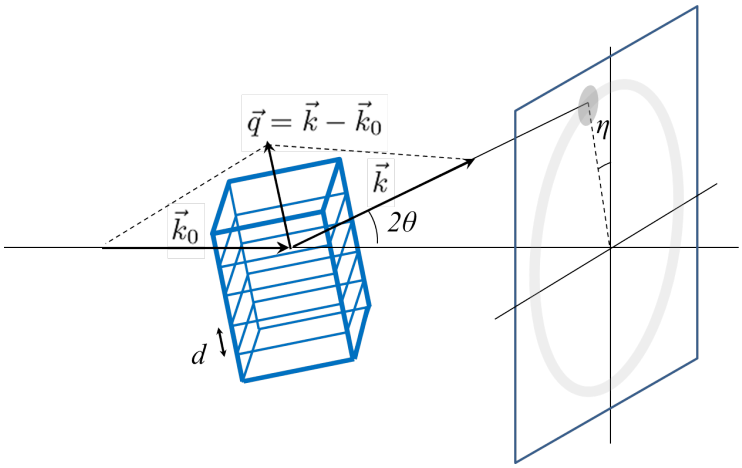

Figure 16: **Scattering geometry** A crystal of lattice plane spacing d gives rise to a diffraction spot at scattering angle 2θ and azimuthal angle η when the crystal is oriented such that the scattering condition is fulfilled.

The scattering angle 2θ is defined as the angle between $\vec{k}$ and $\vec{k}_0$.

An additional selection rule applies to *fcc*-lattices because of the symmetry from the additional atoms at the faces of the cubic unit cell, namely that all indices must be either even or odd. Thus in order of increasing scattering angle the first reflections are (111), (200), (220), and (311).

The scattering geometry is sketched in Figure 19. The scattering plane is defined as the plane containing both $\vec{k}$ and $\vec{k}_0$. For diffraction to take place the lattice plane normal must also lie in the scattering plane, therefore for a single crystal reflections are only seen at specific points on the 2θ-ring. The angle of the scattering plane to the vertical direction is denoted by η and indicates the orientation of the crystal. A powder sample on the contrary diffracts in all directions and gives rise to full Debye-Scherer rings at each scattering angle that fulfils the Bragg condition. A polycrystalline sample gives rise to many reflections distributed on the rings according to the texture of the sample. From the appearance of such diffraction patterns the crystal structure may be resolved and for polycrystalline samples the orientation and even the relative position of each diffracting crystallite may be determined, see below.

2.3.2 Refraction, absorption and tomography

X-rays may interact with crystals and material in general in other ways than diffraction. At an interface refraction may take place and on passing through the material the x-rays may be absorbed, causing a loss of intensity. These properties are determined by the real and imaginary part of the refractive index, respectively, which is given by:

$$n = 1 - \delta + i\beta \tag{49}$$

Here δ is the refractive decrement and β is related to the the linear attenuation coefficient $\mu = 4\pi\beta/\lambda$ for x-rays of wavelength λ. Both parameters depend on the material and the x-ray energy, see Figure 17. Typically for x-rays both parameters are small and furthermore $\delta \gg \beta$. Also note that the refractive index of most materials is less than 1 so that refraction of x-rays occur in the opposite direction to optical light.

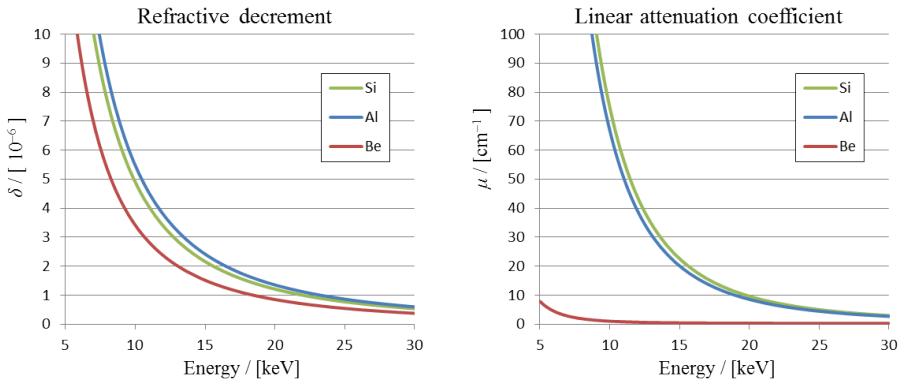

Figure 17: **Constants of refraction and attenuation** The refractive decrement and linear attenuation coefficient for Be, Al, and Si are shown as functions of x-ray energy. From [Nist2018, Henke2018].

The refractive decrement indicates how much the direction of propagation of an x-ray beam changes at an interface as predicted by Snells law of refraction:

$$\frac{\sin\alpha_1}{\sin\alpha_2} = \frac{n_2}{n_1} \tag{50}$$

Here α denotes the angle of the ray to the interface normal and n is the refractive index with the indices 1 and 2 referring to incoming and refracted rays, respectively. For close to normal incidence on a planar interface the angles are

small and $\alpha_2 = (1-\delta)\alpha_1$ (it is assumed that $n = 1$ in air). For x-rays the refractive decrements are small and the effects of refraction are negligible at single interfaces in most cases. However, the mutual effect of refraction of x-rays through a series of many interfaces is non-negligible and may be exploited for example in the form of compound refractive lenses for x-ray microscopy as is demonstrated in this thesis.

The absorption or attenuation of x-rays is governed by Lambert-Beers law, which describes how both the phase and amplitude is altered inside a material according to the refractive index n of the material. For a monochromatic wave $A\exp(ikx)$ of amplitude A and wavenumber k propagating along the x-direction:

$$A'e^{ik'x} = Ae^{inkx} = Ae^{i(1-\delta)kx}e^{-\frac{1}{2}\mu x} \tag{51}$$

Thus $A' = A\exp(-\frac{1}{2}\mu x)$ (or $I/I_0 = \exp(-\mu x)$) and $k' = (1-\delta)k$ so that x-rays passing through and absorbing object will experience a reduction in intensity as well as a phase shift according to the length of its path through the object.

As shown in Figure 17 the attenuation coefficient decreases with increasing x-ray energy, thus to have high penetrative power it is necessary to use hard x-rays. Furthermore, the high x-ray intensity available at synchrotron facilities provides fast measurements of good signal-to-noise ratios.

The attenuation of x-rays is utilized in several imaging techniques since the projected shape and thickness of an illuminated object can be determined by detecting the resulting amplitude or phase. Multiple projections at different orientations of the object may be analysed together by a computerised algorithm to yield the three-dimensional shape of the object. This method is the basis of x-ray tomography. Considering the strong material-dependence of the attenuation coefficient the object may be embedded and x-ray tomography provides a non-destructive means of studying internal structures i 3D. Ultra high spatial resolution may be achieved by measuring the phase shift instead of the absorbed intensity, for example by means of ptychography methods (see for example [Li2018]), grating-based techniques such as Talbot interferometry [Momose2003], or propagation phase contrast tomography (PCT) [Cloetens1997].

Absorption tomography is highly applicable where the differences in absorption coefficient may be exploited to obtain high resolution, for example for mapping porous structures and cracks or samples consisting of different materials or phases. However, for single phase polycrystalline samples the internal contrast is negligible and the boundaries must be dressed with a precipitate of

impurity atoms or a second phase to become visible. This is only possible for certain systems and the technique does not provide any crystallographic information. Thus these techniques are not suitable for local orientation or strain measurements and an extension of the tomography approach is necessary for studying annealing of deformed metals.

2.3.3 Diffraction contrast tomography - DCT

When a polycrystalline sample is illuminated by monochromatic x-rays some of the crystallites may be oriented such that a set of lattice planes fulfil the diffraction condition. Not only does this result in diffraction spots somewhere on the 2θ-rings, it also causes an extinction spot in the projected absorption image since some of the incoming x-ray intensity has been scattered, see Figure 18. A series of images acquired at different angles of rotation ω around a direction perpendicular to the box beam constitutes the input for a reconstruction algorithm. Now imaging of internal structures is possible in the form of diffraction contrast tomography (DCT) [Ludwig2009].

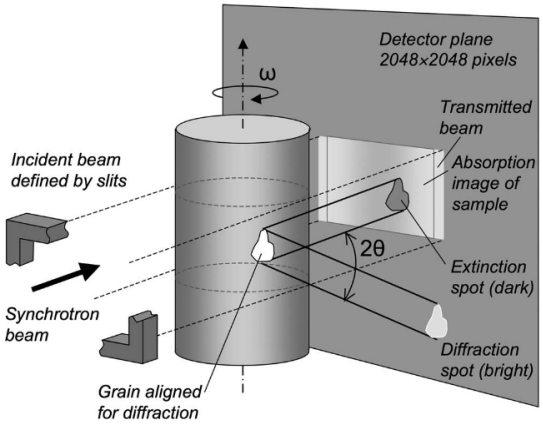

Figure 18: **Diffraction contrast tomography** Grains oriented so that the diffraction condition is fulfilled give rise to an extinction spot in the absorption image as well as a diffraction spot. The incoming beam is restricted by slits to a box beam, and the detector is placed close to the sample to collect both the extinction and diffraction spots. From [Ludwig2009].

By means of DCT a full 3D grain map of a mm-sized sample containing thousands of grains can be obtained with 3D-shape and crystallographic orientation determined for each grain, see Figure 20. The spatial resolution depends

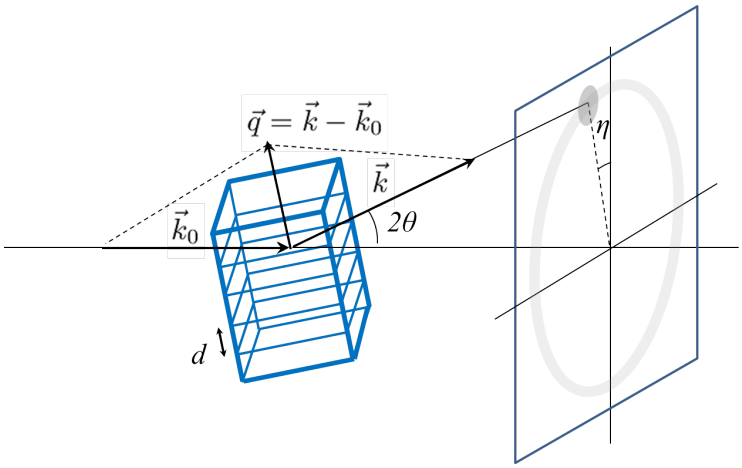

Figure 19: **Scattering geometry** A crystal of lattice plane spacing d gives rise to a diffraction spot at scattering angle 2θ and azimuthal angle η when the crystal is oriented such that the scattering condition is fulfilled.

on the specific setup, with an accuracy in the position of grain boundaries on the order of 2 μm as evidence by comparison to the same boundaries observed with PCT.

The crystallographic orientation of each grain is determined by a reconstruction algorithm, see below, in principle with millidegree precision. However, the grains must be highly uniform and the reconstruction is limited to an internal orientation spread of $< 1°$. The minimum detectable grain-size may be tuned to suit the morphology of the sample and may be as small as a few microns. However, a sample consisting of micron-sized grains can only be mapped if the misorientation between neighbouring subgrains is larger than $2°$ for the diffraction peaks to be distinguishable, and the total number of grains must be sufficiently small ($\leq 10^4$), that peak overlap is avoided. Since the measurements are non-destructive and the mapping may be repeated after annealing and the size, shape and orientation of individual grains may be traced through a heating series. DCT provides a fast method for obtaining an overview of the grain structure of a fully or partly recrystallized sample. The position, orientation, and shape of each grain may be obtained from the measurements and the temporal evolution may be traced. However, no strain measurements are available and furthermore the spatial resolution of DCT is low so for a detailed view of individual grains an additional 'trick' may be applied.

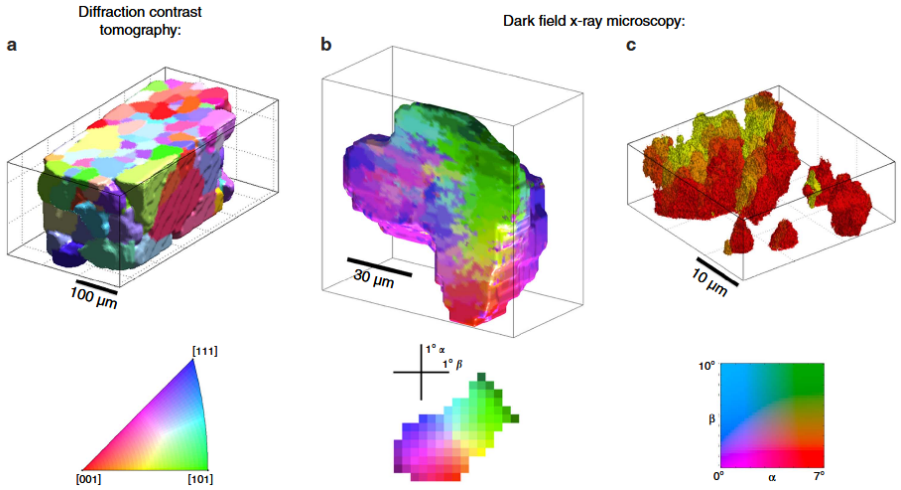

Figure 20: **Multiscale mapping of deformed aluminium** The structure of 10% tensile deformed aluminium mapped at different length-scales. a) Grain map of the whole sample obtained by DCT. The grains are color-coded by the average orientation. b) Zoom on a single embedded grain. The map was obtained by magnified topo-tomography at the DFXRM setup and is color-coded by the orientation to reveal the intrinsic variations in orientation. c) DFXRM map of the orientation variations. The spatial resolution was 3.5 μm, 1.5 μm, and 300 nm and the angular resolution was 0.5°, 0.15 ° and 0.03°, respectively. From [Simons2015].

2.3.4 Topo-tomography

The topology of a single grain may be investigated by aligning the scattering vector with the axis of rotation, see Figure 21. The technique called topo-tomography [Ludwig2001] has a sub-micron spatial resolution, and may be extended to yield the local orientation variations with a resolution of 0.1° by collecting a rocking curve at each step while rotating the sample. Furthermore, the setup and acquisition time may be fine-tuned to give the optimal resolution for a specific grain. The technique is fast but only works for one grain at the time.

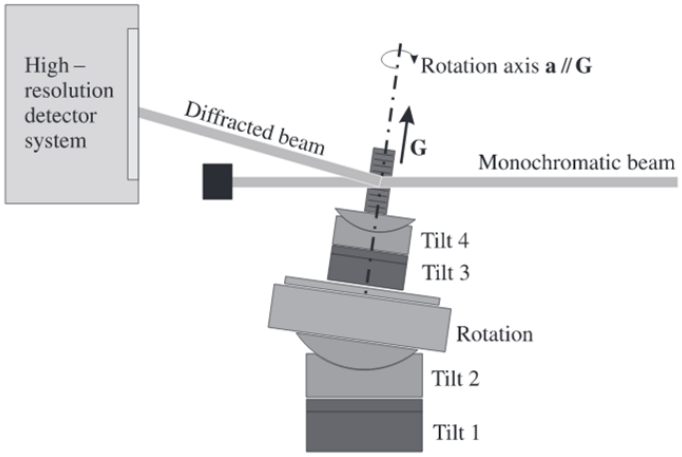

Figure 21: **Topo-tomography setup** In the topo-tomography setup the axis of rotation is aligned with the scattering vector such that the condition for diffraction is fulfilled throughout the rotation series. The 3D shape of the grain is reconstructed from the projections. From [Ludwig 2001]

Topo-tomography is well-suited for tracing the evolution of a recrystallizing grain during annealing and to monitor the migration of its boundaries into the surrounding deformed matrix in 3D. This was for example demonstrated in [vanBoxel2014], see Figure 22.

2.3.5 Three-dimensional x-ray diffraction - 3DXRD

Three-dimensional x-ray diffraction (3DXRD) also known as high energy x-ray diffraction microscopy (HEDM) are techniques for tracking and mapping the grain structure of a sample with spatial resolution in the micron-range and an

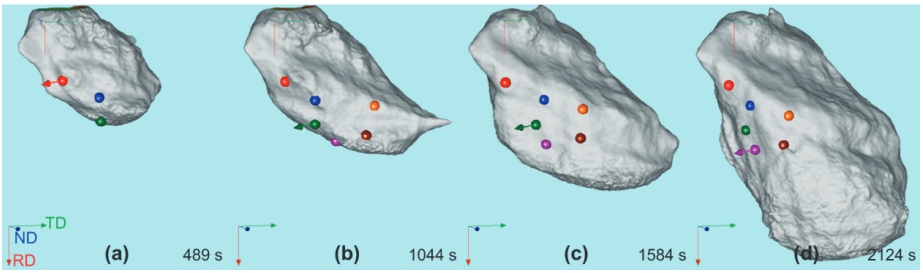

Figure 22: **Growth of recrystallizing grain** The shape of an initially 100 μm recrystallizing grain in an aluminium AA1050 single crystal cold-rolled to 30% reduction in thickness as mapped by topo-tomography. The sample was annealed several times and the grain was mapped in between each heating step to yield an annealing series. The coloured spots are used to identify grain boundary facets. From [vanBoxel2014]

angular resolution of 0.1°. The full 2θ-rings in far field are acquired for as many reflections as possible and the sample is rotated around its vertical axis to create the input for a reconstruction algorithm, see below. Typically, a line beam is applied and the 3D-structure is pieced together from scans at different vertical positions. Accompanying near field data or data acquired at several sample-to-detector distances allow for tracking of diffraction spots to facilitate reconstruction. Since the method is non-destructive, the sample may be heated or deformed and then mapped again. For a thorough description of 3DXRD the reader is referred to [Poulsen2004].

A sketch of the experimental setup is shown in Figure 23 together with an example of a detector image observed for a polycrystalline sample in the far field. The intensity of individual diffraction spots may be tracked through a series of images obtained while annealing the sample. Since the intensity is proportional to the diffracting volume this procedure gives a qualitative measure of the evolution of the volume of the grain corresponding to the diffraction spot. Two examples of this are given in Figure 24 for annealing of cold-rolled aluminium AA1050. On the left is shown the growth of six (small) recrystallizing grains during annealing from nucleation to radius of 2-7 μm [Lauridsen2000] and on the right the growth of recrystallizing grains from sizes of 5-20 μm in diameter is shown [Poulsen2011]. It was observed that the growth of individual grains are very different. The initial growth of nuclei was step-wise and at larger sizes the growth curves became approximately linear with individual growth

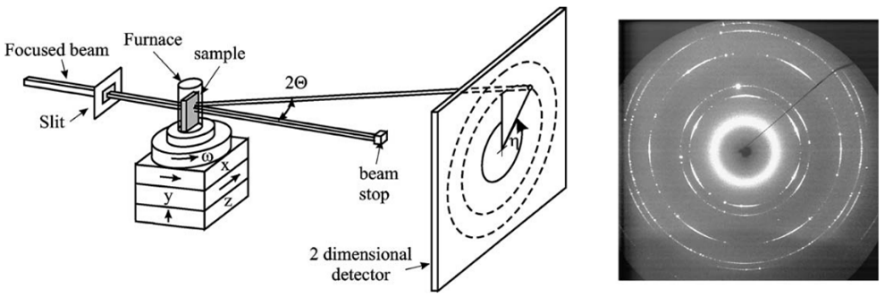

Figure 23: **3DXRD setup** For 3DXRD-measurements the sample is illuminated by a line beam and the detector is placed in the far field region to collect the diffraction pattern at a series of rotations of the sample around the vertical axis. Data may be collected at several detector positions including to facilitate tracking of the grain positions. From [Lauridsen2003].

rates depending on temperature. However, the observed growth curves does not comply with the prevalent assumption that grain size determines the growth behaviour. The individual activation energies for the growth of 793 grains were determined from the change in growth rates (slope of growth curve) before and after increasing the temperature slightly.

The evolution of subgrains with radius > 150 nm may be traced in thin samples less than 100 subgrains thick, however, the detectable orientation difference between subgrains is limited to $0.3°$ [Gundlach2004]. To increase the angular resolution and the resolvable number of grains a narrow point beam may be applied instead of a line beam to avoid diffraction peak overlap [Hayashi2015]. However, this requires a beam size considerably smaller that the grain size and the acquisition time is markedly increased.

By reconstructing the grain shape, see below, the growth of individual grains during annealing may be 'filmed' in 3D. The first example of the growth of a recrystallizing grain was given in [Schmidt2004] with a spatial resolution along the best direction of 4.2 μm. It was observed that the grain growth was highly heterogeneous. Likewise, the full grain structure of a recrystallized sample may be reconstructed and the grain growth filmed during annealing, see for example [Schmidt2008, Hefferan2012].

The method relies heavily on robust reconstruction algorithms, see for example [Lauridsen2001, Bernier2011]. The algorithms identify and back-project the diffraction spots by the aid of a quaternion representation and iteratively

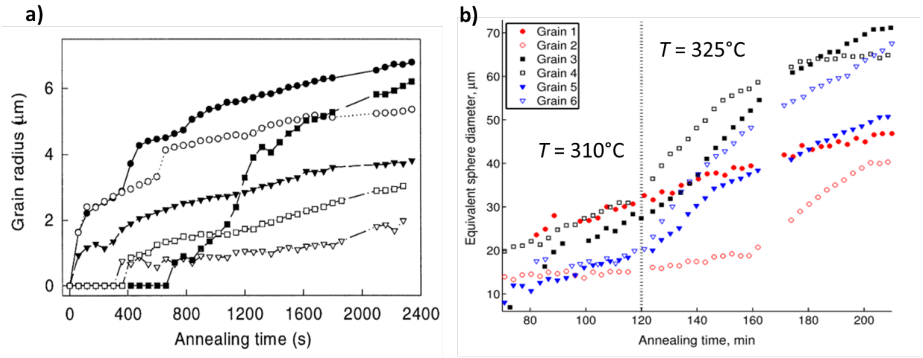

Figure 24: **Growth curves for recrystallizing grains** Recrystallizing grains tracked during recrystallization of cold-rolled aluminium AA1050. The grains exhibit individual growth kinetics. a) Nucleation and initial growth of new grains in a specimen cold-rolled to 42% reduction in thickness and annealed at 270°C. From [Lauridsen2000]. b) Growth curves for recrystallizing grains in a 50% cold-rolled specimen. The sample was annealed at 310°C for the first 120 min. then the temperature was increased to 325°C. Activation energies for the individual grains was determined from the difference in growth rate before and after the increase in temperature. From [SPoulsen2011].

matches the reconstructed grain structure and the intensity and positions of the measured diffraction spots until convergence is achieved. In this way the size and position of all grains in the polycrystalline sample may be determined, since the volume of a grain is proportional to the scattered intensity and the intersection of back-projections from the same grain reveals its position within the sample. The shape of the individual grains may be estimated by tessellation, but if the scope of the study is to examine the grain boundaries it is more reliable to include near field diffraction data or DCT and apply an iterative backwards-forwards projection algorithm, that accounts for both position, orientation, strain, and shape at the same time. Current state-of-the-art allow reconstruction of samples consisting of up to 20.000 grains, but the spatial resolution is limited by detectors to at best 1 μm [Simons2015].

2.3.6 Scanning beam techniques

As an alternative to the monochromatic diffraction methods described above a polychromatic beam focused down to a pencil beam of very small size may be utilized to scan the sample. In this way a single line through the sample diffracts at a time and by scanning an absorbing wire across the sample perpendicular to this line, the diffraction from each point in depth through the sample may be identified. This technique provides a high spatial resolution of 300 nm and differential aperture x-ray microscopy (DAXM) has recently been successfully applied to map both the advancing boundary of a recrystallizing grain and the surrounding deformed matrix at the same time [Zhang2017], see Figure 25. However, scanning techniques are slow due to the need for data acquisition at each voxel individually and only a small sample volume may be mapped.

2.3.7 Combination of techniques

The experimental setup for DCT, topo-tomography, and 3DXRD are similar and all three types of experiments may be performed at the same high energy instrument by adjusting the beam shape, detector positions and the approach to data acquisition. The sample volume may be fully illuminated or scanned in a layer-by-layer manner and the data may be analysed statistically from tracking many individual diffraction spots or reconstructed to yield volumetric visualisations. In general, the setup may be customized to suit the morphology and texture of the sample, but the techniques are limited to polycrystalline samples

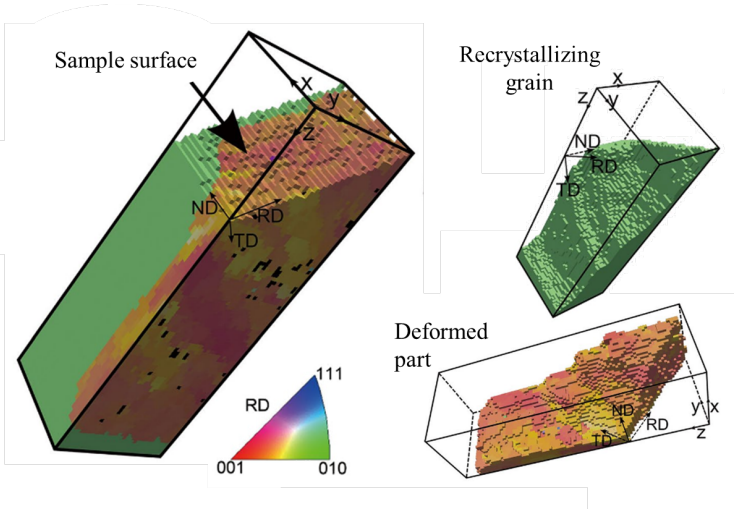

Figure 25: **A recrystallizing grain and deformed matrix** 3D visualisation of a $28 \times 32 \times 95$ μm^3 volume containing a recrystallizing grain and the deformed matrix in partly recrystallized high-purity aluminium which had be cold-rolled to 50% reduction in thickness prior to annealing. The map is color-coded according to the local orientation. The boundary migration was characterized in terms of the relation to the deformed structure. Adapted from [Zhang2017].

of rather well-defined micron-sized grains of orientation spread of less than a few degrees. If the grains are deformed to a higher strain a complimentary option at the same setup is to study the evolution of the internal structure such as the formation of subgrains and nuclei by means of high resolution reciprocal space mapping, see for example [Jakobsen2007]. The 3DXRD and DCT-techniques and the reconstruction algorithms are now well-established, and even a laboratory version of DCT (labDCT) has been developed and demonstrated to be able to produce grain-maps and trace several hundreds of grains of average initial size of 100 μm and minimum detectable size of 40 μm and spatial resolution of 5 μm [McDonald2015].

Recently, an additional complementary technique was presented, namely dark field x-ray microscopy (DFXRM), see [Simons2015, **Paper6**]. This technique utilizes a similar basic setup with a full illumination or a narrow line beam (the latter is used in this thesis), but with the addition of a x-ray objective to magnify a diffracted signal from a single grain. In this way, a spatial resolution of less than 100 nm may be achieved and with a sub-millidegree angular resolution DFXRM provides new possibilities for mapping deformed structures as well as grain shapes in greater detail, see Figure 20. In combination, an overview map of the grain structure of polycrystalline materials may be obtained by DCT or 3DXRD, a single bulk grain may be selected and mapped with better resolution by topo-tomography, and with DFXRM the details of the internal variations in orientation and strain may be mapped without moving the sample. Furthermore, the measurements are non-destructive and fast enough to be repeated during deformation or annealing.

In this thesis, DFXRM is applied to recrystallization for the first time and a new complimentary method for tracking the evolution of subgrains in the deformed structure is presented. A presentation of the DFXRM-technique is given in the following chapter.

3 Dark field x-ray microscopy

To study structural dynamics during deformation and annealing of metals and polycrystals in general there is a need for a fast multiscale 3D-imaging technique capable of mapping bulk structures non-destructively. Currently well-established x-ray techniques such as those presented in the previous chapter provide neat grain maps, growth curves and grain shapes but are limited by detectors to a spatial resolution of 1 μm and an angular resolution of 0.1°.

In this chapter the new technique dark field x-ray microscopy (DFXRM) is presented, which takes x-ray imaging to the next level by providing 3D-maps of the mosaicity and strain distributions with better than 100 nm spatial resolution and millidegree angular resolution. The technique relies on the ability of an x-ray objective to single out a narrow angular range and magnify the direct space distribution of sources of diffraction of that particular corresponding lattice orientation and strain. Furthermore, the objective works as a filter that selects a single diffraction spot thereby avoiding spot overlap.

The geometry, experimental setup, and data acquisition strategies are described in the first section. Details are also found in [Simons2015, **Paper6**] together with a first demonstration of the technique and an overview of recent results, respectively. A brief introduction to the optical properties of compound refractive lenses (CRL) and the resulting resolution of the x-ray microscope is included since the theoretical description of CRLs and their application to DFXRM has been a significant part of the phd-work. A thorough description is found in [**Paper4**, **Paper5**].

The following sections describe the data acquisition and analysis, and a novel theoretical description of how DFXRM measurements may be interpreted as direct measurements of dislocation densities is presented [*paper currently in preparation*]. The importance of careful alignment and focusing of the microscope has become evident through the analysis of the data acquired during the thesis work. Therefore a section on the current methods for focusing and the problems involved as discovered during the thesis work is included. The chapter is concluded with a section describing the samples.

3.1 Experimental method and setup

This section gives an introduction to DFXRM. The geometry of the experiment and method is described followed by a walk-through of the setup at the dedi-

cated DFXRM beamline where the measurements presented in this thesis were performed. The resolution of the instrument and data acquisition strategies are discussed.

3.1.1 Geometry

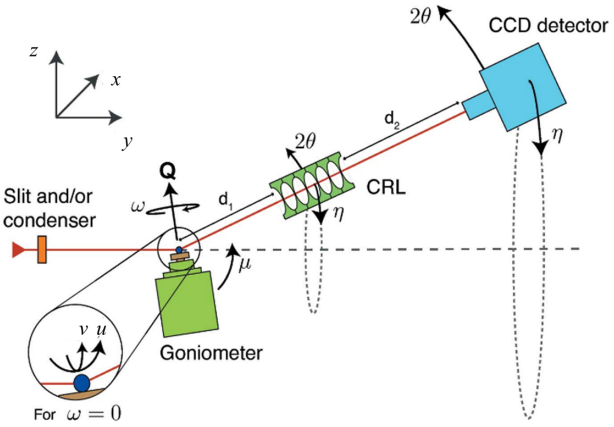

Figure 26: **DFXRM setup** Definition of parameters. The sample is illuminated by a line beam to select a layer and the objective singles out a nsrrow range in angular space. In this manner there is a direct correspondence between the sample and detector coordinates. The lab coordinate system is defined. From [**Paper5**].

An overview of the geometry of the DFXRM setup is shown in Figure 26. A pixel on a two-dimensional detector has coordinates (x_d, z_d) denoting the horizontal and vertical directions, respectively, and may be understood in terms of the scattering angle 2θ which defines the deviation of the direction of the diffracted beam with respect to the direct beam and the angle η which defines the rotation of the scattering plane away from the vertical direction.

A crystallite in the sample has position (x_s, y_s, z_s) where y_s is parallel to the beam, x_s is horizontal and perpendicular to the beam, and z_s is the vertical direction. When illuminated, the crystallite diffracts at scattering angle 2θ only if the crystallite is oriented such that the diffraction condition is fulfilled. The scattering angle is related to the lattice plane separation d by Braggs law, see section 2.3. The orientation of the lattice plane normal is given in terms of two tilts, u with axis of rotation parallel to x_s and v around y_s. Thus a diffraction

spot observed at a certain detector position is a 2D projection (x_d, z_d) of 6D information $(x_s, y_s, z_s, u, v, 2theta)$, which may be extracted by reconstruction as for 3DXRD and DCT or by restricting the geometry of the experimental setup.

If the spatial position of the diffracting point inside the sample is known, 2θ gives the internal axial strain, ϵ, from Braggs law, since $d = d_0(1+\epsilon) = \lambda/2\sin(2\theta/2)$. The angle η gives the tilt of the lattice along v and $u = 2\theta/2$. If the position is unknown, but the illuminated area is small and the scattering geometry is vertical with a limited η-range, the horizontal detector position of the diffraction spot is a convolution of orientation v and position x_s. The vertical detector position is then a convolution of position in y_s and z_s and the strain (and to some extend u, which is related to 2θ). A more rigorous description of the coordinate system etc. in given in [**Paper5**].

3.1.2 DFXRM approach

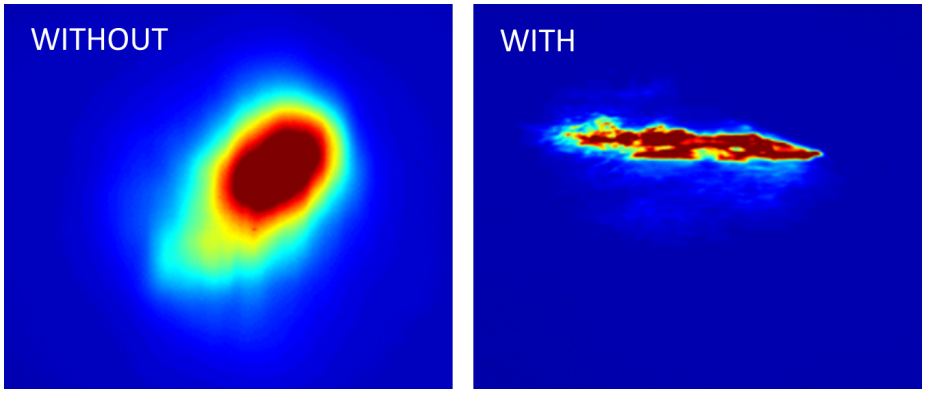

Figure 27: **Diffraction without and with the objective lens** Without the objective the diffraction spot is approximately Gaussian, whereas with the objective a direct space image of the distribution of the selected strain and lattice orientation is obtained.

For DFXRM the incoming beam is shaped by slits and a condenser to a narrow line beam which defines an illuminated layer in the sample and thereby z_s is known. The objective singles out a narrow region in angular space, thereby defining both (u, v) and 2θ. Thus the detector image may be immediately interpreted as a 2D real space image of the spatial distribution of the selected orientation and strain within the selected layer. Furthermore, the objective

serves to magnify the diffracted signal such that the spatial resolution of the measurements is markedly increased.

Now there is a direct spatial correspondence since $(x_d, z_d) = -\mathcal{M}(x_s, y_s \tan(2\theta))$, see Figure 27, and the full 6D space may in principle be mapped by acquiring images at all orientations and all values of 2θ for a series of layers in z_s that covers the full sample. In practice this is not feasible, however, the mosaicity of a single grain of low internal orientation spread $< 1^\circ$ may be mapped in 3D in a manner of hours by acquiring detector images at a series of tilts in (u, v) for a series of consecutive layers. From the images acquired at a series of small tilts in (u, v) that covers the full diffraction peak from that layer in the grain, the orientation of the scattering vector at each point of the sample may be assigned as the orientation of highest intensity (see the DFXRM data analysis section). Likewise, information about the local axial strain at each point in the sample is obtained in a similar manner by adjusting the objective in a series of 2θ-values and tilting the sample, typically only in u, since the resolution in this tilt direction is an order of magnitude better than in v, see below. Both the assigned orientation and strain must be corrected by a linear factor in the position, see below. As a main part of this thesis DFXRM is utilized for mapping the intrinsic mosaicity and strain in a recrystallizing grain. The results are presented in Chapter 4.

3.1.3 Near field statistics approach

Without the objective, the intensity profile in the far field of a diffraction spot from a single crystalline region is approximately Gaussian with a width given by the instrumental resolution and the angular size of the diffracting region, see Figure 27. In the near field the shape of the diffraction spot is related to the shape of the diffracting region. The integrated peak intensity is always proportional to the volume of the diffracting region. If the diffracting region is not single crystalline but possesses mosaicity and variations in internal strain, the spot will be broadened in the horizontal direction due to mosaicity and in the vertical direction due to strain variations.

For a polycrystalline sample of micron-sized (sub)grains, individual spots from the many small crystalline regions may be identified if the energy, illuminated area, and detector position is chosen carefully. The detector position must be in the near field region, where a section of a few degrees in η a Debye-Scherer

ring can be detected. A tilt series in u covering a few degrees will add an extra dimension to yield a piece of the diffraction surface. The position of spots in the u-direction is directly interpretable as lattice orientation. Each diffraction spot may be traced through for example a heating series and changes to the spot intensity, size, shape, and detector position in (x_d, z_d, u), can be interpreted as changes to the internal properties such as size, orientation, strain and internal disorder of the crystalline regions.

This approach is applied in Chapter 5 as a means for statistical analysis of the evolution of the subgrain structure during recovery of a partly recrystallized sample, which is the second main part of this thesis.

3.1.4 Beamline ID06

All experiments were carried out at the high brilliance x-ray source European Synchrotron Radiation Facility, ESRF, in Grenoble, France, in the EH1 hutch at the beamline ID06 which is dedicated to DFXRM. Below is given a walk-through of the beamline and experimental setup following the direction of the x-ray beam, see Figure 28. For details about the accelerator ring the reader is referred to consult the ESRF-webpage [ESRF2018].

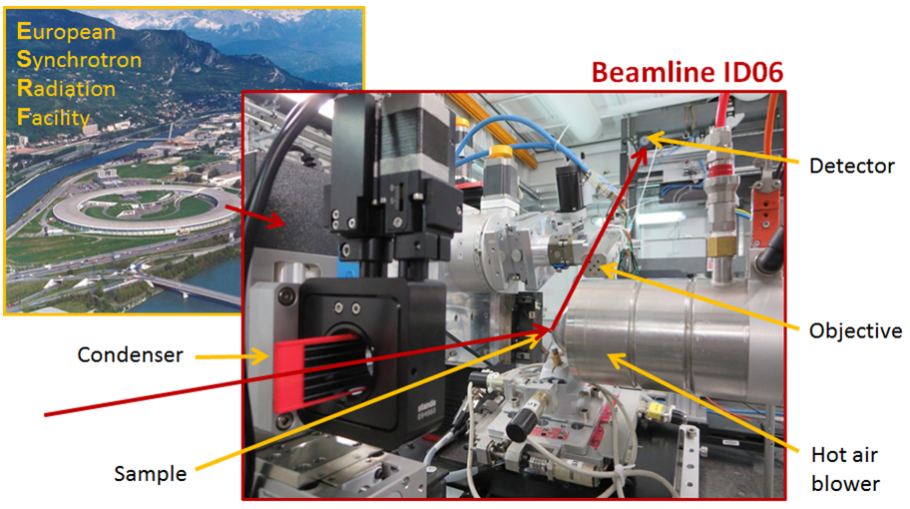

Figure 28: **Beamline ID06** The beamline ID06 at ESRF is dedicated to DFXRM experiments. The instrumental setup consists of condenser, sample-stage, objective, and several detectors. A hot air blower is installed here for annealing.

X-rays are created at an undulator magnet and photons of a particular energy is selected by a Si(111) Bragg-Bragg monochromator. For the present studies the selected energies were 15 - 17 keV, which is equivalent to an x-ray wavelength of 0.83-0.73 Å. The divergence of the incoming beam was on the order of 10^{-3}.

The beam is slightly focused onto the sample position (or condenser) by a transfocator. The transfocator consists of a selection of Si-lenses, which may be combined in different ways to optimize the focusing. Slits may be inserted at different positions to limit the size of the beam at the expense of loss of intensity, and a decoherer may be introduced to minimize coherent scattering effects.

For DFXRM the incoming x-rays are shaped into a narrow line-beam through a condenser, see description below. A Gaussian horizontal line beam of FWHM = 200 nm in height is achievable at the sample position. Slits define the width of the line-beam, which is typically set to 200 μm.

The sample is mounted on a sample stage with many degrees of freedom to provide accurate sample alignment. The tilts and positions are adjusted by high precision motors. The source-to-sample distance is 55 m.

A crucial part of the microscopy setup is the objective, which selects a narrow range of angles and magnifies the diffracted signal in direct space. In this way the spatial and angular information is deconvoluted as described above since only a small section of the full diffraction peak in angular space is let through the objective, revealing the spatial distribution of this particular orientation within the illuminated slice of the sample. Both the condenser and the objective are so-called compound refractive lenses or CRLs, which consist of a series of many x-ray lenses, see description below.

Several detectors are available, out of which the two are applied in the present study, namely a far field and a near field detector. Both were FReLon camera with an effective pixel size of 1.622 μm. The near field detector may be positioned in the near field region 0.5-50 cm away from the sample and thee far field detector is mounted on a cradle to catch the individual diffraction peaks in the far field at a distance of approximately 5 m, depending on the diffraction peak and the x-ray energy. For purposes of finding the peak on the far field detector at the large distance from the sample, a low resolution Basler detector of larger field-of-view is mounted next to the far field camera. Furthermore, a semitransparent diffraction camera is available at the near field position as well as a horizontal far field camera for the purpose of combining DFXRM with

DCT or 3DXRD studies. A hot air blower was installed to be able to carry out *in situ* studies during annealing.

Since the experiments presented in this thesis were carried out the setup at ID06 has been almost completely replaced by a dedicated setup, which is designed to overcome some of the problems faced in this work. In particular, a new and more reliable sample stage with more degrees of freedom for sample alignment has been implemented since the original sample stage had problems with reproducibility of the small step-sizes necessary for DFXRM. Furthermore, to stabilize the setup everything has been remounted on a 20 tonnes piece of granite. Also, a furnace for heat treatment has been installed.

3.1.5 Compound refractive lenses

The refractive index of x-rays is close to 1 in most materials. Therefore, passing through a single interface does not alter the beam profile or direction of propagation much, and a single x-ray lens have negligible effect. However, the combination of many such lenslets may have a non-negligible effect if the geometry and material properties of the lenses are carefully designed.

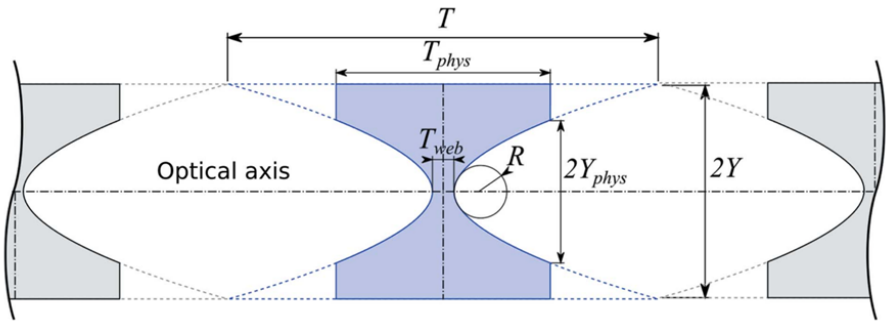

Figure 29: **Compound refractive lens** A CRL consists of a series of parabolic lenslets. From [**Paper4**]

Compound refractive lenses (CRL) are constructed from a series of N parabolic lenslets, each of which has a radius of curvature R and a thickness T, see Figure 29. Together with the energy-dependent refractive decrement δ and the absorptivity μ this defines the optical properties of each lens, which has a focal length of $f = R/2\delta$.

The collective effect of the series of N lenses in a CRL may be derived by the aid of the ray transfer formalism, see [**Paper4**]. With the small parameter

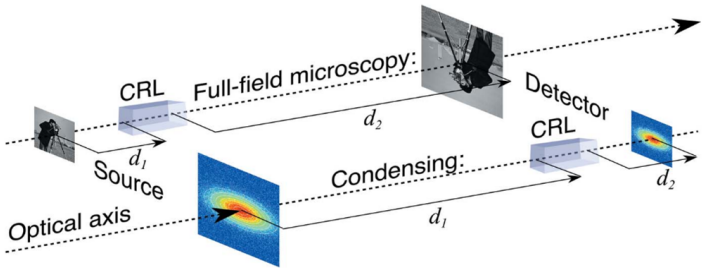

Figure 30: **Condenser and objective** CRLs may be employed as both condenser and objective in DFXRM. From [**Paper4**].

$\phi = \sqrt{(T/f)} \ll 1$ the focal length is given by:

$$f_N = f\phi \cot(N\phi) \tag{52}$$

CRLs have two applications in the DFXRM setup, as condenser and objective, respectively. For a lens of thickness NT and a sample-to-detector distance of $L = d_1 + d_2 + NT$ the two distances d_1 and d_2 defined in Figure 30 must fulfil the modified lensmakers equation:

$$\frac{1}{d_1} + \frac{1}{d_2} + \frac{1}{f_N} + \frac{f_N \tan(N\phi)}{d_1 d_2} = 0 \tag{53}$$

The two combinations of the distances that fulfil these conditions give the two different CRL-configurations: Condensing for $d1 > d2$ and the imaging condition that gives magnification for $d1 < d2$, see Figure 30. The main properties of the two configurations are stated below and the reader is referred to [**Paper4**] for the full derivation or e.g. [Poulsen2014] for a derivation applying an simpler approximation.

3.1.6 Condenser

The role of a condenser is to focus the almost parallel beam coming from the source through the transfocator, and d_1 may be taken at infinity so that $d_2 = f_N$ from the lensmakers equation. Thus to have the smallest and most intense spot at the sample position, the sample must be placed at the focal point, that is at a distance f_N from the exit of the condenser. The Gaussian beam emerging from a CRL has a root-mean-square (RMS) σ_C of (see [**Paper4**]):

$$\sigma_C = \sqrt{\frac{R}{\mu N}} \frac{1}{\sqrt{1 + \mathrm{sinc}(2N\phi)}} \tag{54}$$

The divergence Q of the condensed beam is given by:

$$Q = \frac{2\sigma_C}{f_N} \tag{55}$$

The resulting FWHM height of a diffraction limited beam at the sample position is:

$$H = \sqrt{2\ln 2}\lambda/(\pi Q) \tag{56}$$

For the present DFXRM experiments the condenser lenses were etched in a Si-waver as described in [Stöhr2015], see Figure 31.

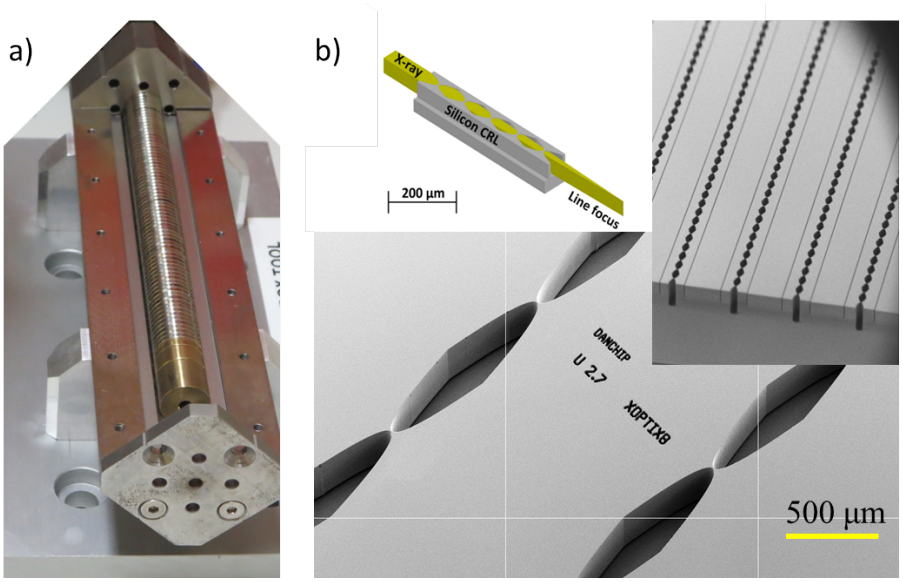

Figure 31: **Be- and Si-CRLs** a) The DFXRM objective is a CRL that consists of up to 72 two-dimensional Be-lenslets. b) CRLs etched in a silicon-wafer provides line beam focus when applied as condensers. Courtesy of F. Stöhr.

3.1.7 Objective

When applied as an objective, the CRL provides a magnification $\mathcal{M}$ given by [**Paper4**]:

$$\mathcal{M} = \cos(N\phi)\left[\frac{d_2}{f_N} - 1\right] \tag{57}$$

Besides the properties of the CRL, the magnification depends on the sample-to-detector distance and the x-ray energy, since the material parameters depend on energy, see Figure 17. Typical values for the present work are $\mathcal{M}15 - 20$. Furthermore, the objective selects a narrow range of angles. The angular acceptance function is Gaussian with a RMS σ_a of [**Paper5**]:

$$\sigma_a = \delta\frac{\mathcal{M}}{\mathcal{M}+1}\sqrt{\frac{2N}{\mu R}} \tag{58}$$

Likewise, the vignetting function, which describes the available field of view, is Gaussian with an RMS σ_v which is given by:

$$\sigma_v = \frac{\delta}{2\mu\sigma_a}\left[(N\phi)^2 - \sin^2(N\phi)\right]^{-\frac{1}{2}} \tag{59}$$

A characteristic distance $1/\gamma$ which defines the median angle at a sample position at a particular distance to the optical axis is given by:

$$\frac{1}{\gamma} = \left[\frac{\sigma_C^2 - \sigma_v^2}{\sigma_a}\right]^{\frac{1}{2}} \tag{60}$$

3.1.8 Resolution

The resolution of the x-ray microscope is given in angular space by the divergence of the condensed beam in the parallel tilt direction and in the perpendicular tilt direction by the divergence of the incoming beam [Resolutionpaper]:

$$\Delta u = Q \tag{61}$$

$$\Delta v = 2\frac{sigma_a}{\sin(2\theta)} \tag{62}$$

For a diffraction limited beam the resolution in direct space is:

$$\Delta x_s = \frac{\lambda}{2\sigma_a} \tag{63}$$

$$\Delta z_s = H \tag{64}$$

The in-plane spatial resolution is given by the properties of the objective lens whereas the spatial resolution in the vertical direction or the layer thickness is

given by the height of the condensed beam. Thus there are restrictions on the simultaneous resolution in direct and angular space, since $\Delta x \cdot \Delta v \geq \lambda / \sin(2\theta)$ and $\Delta z \cdot \Delta u \geq H \cdot Q = \sqrt{2 \ln 2}\lambda$. This implies that the resolution may be optimized to either direct or reciprocal space and that the optimal resolution is better for higher energies.

The voxel size in direct space is given in-plane by the effective detector pixel size divided by the magnification provided by the objective and corrected for the elongation due to projection and as the step size in the direction perpendicular to the line beam. The step-sizes in angular space are given by the sampling mesh grid. For most measurements the resolution in u is so good that it is more convenient to collect the integrated for each step as while the motor is moving. For details on reciprocal space resolution see [**Paper5**].

3.2 Data analysis

Data acquisition should be planned carefully to exploit the full potential of the DFXRM method and the instrumental resolution. The measuring procedures and data analysis are presented in this section and a novel interpretation of the results in terms of dislocation densities and distortion tensor components is derived.

3.2.1 Measuring procedures and mapping

A single layer of the sample is illuminated by a line beam 200-300 nm in height and a diffraction peak from a structural element of interest, for example a recrystallizing grain, is identified. The instrument is focused to the selected diffracted signal. Only a small angular section of the full diffraction peak is let through the objective at a given orientation of the sample and a direct space map of the spatial distribution of the corresponding particular lattice orientation is obtained. By tilting the sample slightly small variations in the local orientation of the lattice normal may be mapped.

A tilt-series in (u, v) is set up that covers the whole range of angles for which the diffracted signal has intensity, which is typically 0.2-1°, and images are acquired at each slightly different orientation of the lattice normal $\vec{G}$. Examples of images at different tilts are shown in Figure 32.

From this 4D data in (x, y, u, v) the local orientation distribution of each voxel in direct space may be pieced together from the intensity of that particular

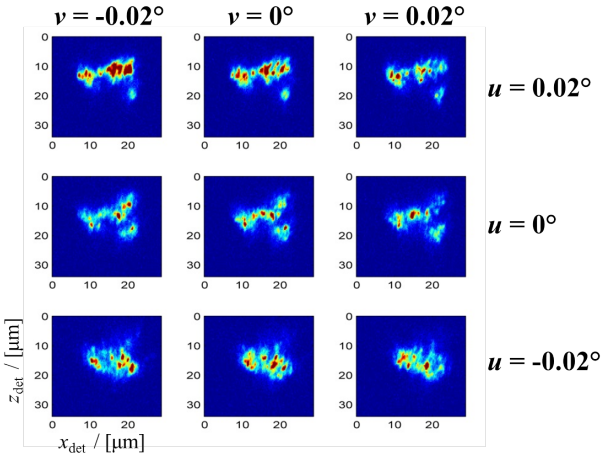

Figure 32: **Raw data** Detector images at slightly different sample orientation. The images are taken from the mosaicity data series presented in Chapter 4. The difference in tilts between images are 0.01°.

voxel in all images in the data series. The local (average) orientation is assigned to individual voxels from a fit to the local orientation distribution, see Chapter 4. The fit may be an overall center-of-mass fit for the whole orientation distribution or it may be a fit to a selected region of the orientation distribution around the orientation space pixel of maximum intensity. The resulting map gives an overview of the intrinsic mosaicity in the crystallite giving rise to the diffraction peak.

Likewise, local maps of the internal variations of axial strain are obtained by a similar approach in which data series in $(u, 2\theta)$ are acquired and the local (average) axial strain is assigned to each voxel from a fit to the intensity distribution for that particular voxel through the data series. See also Chapter 4.

Maps in 3D may be obtained by translating the sample along the vertical direction to illuminate consecutive layers and repeat the tilt-series and analysis.

Note that what is measured is the variations in orientation of the lattice plane normal and the lattice plane spacing. Thus the resulting orientation map only covers two out of three orientational degrees of freedom, since the in-plane lattice orientation is completely unknown. This direction could in principle be investigated by mapping a reflection with a perpendicular component. However, this is not done in the present work. Likewise, the axial strains along the two

perpendicular directions are unknown, but could be measured by mapping at least two complementary reflections.

3.2.2 Geometrical corrections

The assigned local orientation and strain must be corrected according to the position of the diffracting point in the sample. The equations describing the necessary corrections are given in terms of the characteristic length scale γ as [**Paper5**]:

$$\Delta v_{\text{corr}} = \frac{\gamma x_s}{2\sin\theta} \tag{65}$$

$$\Delta 2\theta_{\text{corr}} = -\frac{\gamma y_s}{\tan 2\theta} \tag{66}$$

The need for these geometrical corrections stems from the correlation between the position of the a diffracting point in the illuminated plane and the angle of incidence on the objective, see the sketch in Figure 33.

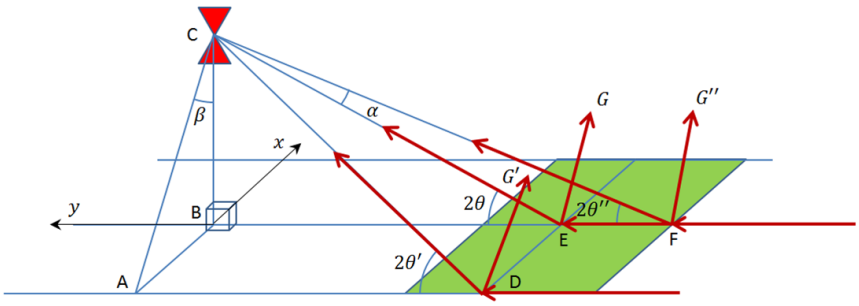

Figure 33: **Geometrical corrections** The position of a diffracting point in the illuminated plane is correlated with the measured orientation and strain and corrections for this must be implemented in the data analysis. Even though the lattice vectors $\vec{G}$, $\vec{G}'$, and $\vec{G}''$ are all observed at the same sample tilts they are not parallel.

3.3 Diffraction from a weakly distorted lattice

Equations for diffraction from a weakly distorted lattice was derived as a part of the thesis work and is presented in this section. It is shown how the deformation tensor determines the scattering vector for a distorted lattice and how this is

connected to the orientation and strain obtained from DFXRM measurements. In this manner, combinations of the gradients of the measured orientation and strain gives some of the components of the Nye tensor, which is related to the dislocation density.

3.3.1 Distortion tensor

The (local) lattice basis vectors $\vec{a}_i'$ of a weakly distorted lattice are given in terms of the undistorted lattice basis vectors as:

$$\vec{a}_i' = \sum_j F_{ij}\vec{a}_j \tag{67}$$

For a weakly distorted lattice we may write

$$\mathbf{F} = \mathbf{I} + \beta \tag{68}$$

where $\mathbf{I}$ is a unit matrix and the distortion tensor β, which is assumed to be small such that $\beta_{ij} \ll 1$ as described in Chapter 2. The distortion tensor may be expressed in terms of the antisymmetric lattice rotation tensor ω_{ij} and symmetric elastic strain tensor ϵ_{ij} as $\beta_{ij} = \epsilon_{ij} + \omega_{ij}$.

For samples of high dislocation densities mapped by experimental techniques of limited spatial and angular resolution, each voxel contains many dislocations and the measurements are averaged over the structure of each voxel. As shown in Chapter 2, dislocations close together shield each others strain fields but together they give rise to large lattice rotations. Therefore it is common to set $\beta_{ij} = \omega_{ij}$ for analysis of for example EBSD measurements [Pantleon2008]. However, by means of DFXRM the mosaicity and strain variations caused by a low dislocation density may be mapped due to the high angular resolution of the technique. Thus individual voxels may contain single or no dislocations. In this case rotation and strain are similar in size.

Consider small rotations (ϕ_x, ϕ_y, ϕ_z) around the sample coordinates axes (x_s, y_s, z_s) where rotations are positive in the counter-clockwise direction. The associated rotation matrix is:

$$\omega = \begin{bmatrix} 0 & -\phi_z & \phi_y \\ \phi_z & 0 & -\phi_x \\ -\phi_y & \phi_x & 0 \end{bmatrix} \tag{69}$$

The diagonal elements of the strain tensor are the axial strains $(\varepsilon_x, \varepsilon_y, \varepsilon_z)$, which are negative for compression, and the off-diagonal elements of the symmetric

strain tensor are given by the shear strains $(\gamma_x, \gamma_y, \gamma_z)$, where γ_i indicates shear in the plane perpendicular to the i-axis:

$$\epsilon = \begin{bmatrix} \varepsilon_x & \gamma_z & \gamma_y \\ \gamma_z & \varepsilon_y & \gamma_x \\ \gamma_y & \gamma_x & \varepsilon_z \end{bmatrix} \tag{70}$$

Thus to first order in the small lattice distortions β is given by:

$$\beta = \begin{bmatrix} \varepsilon_x & \gamma_z - \phi_z & \gamma_y + \phi_y \\ \gamma_z + \phi_z & \varepsilon_y & \gamma_x - \phi_x \\ \gamma_y - \phi_y & \gamma_x + \phi_x & \varepsilon_z \end{bmatrix} \tag{71}$$

3.3.2 Diffraction

As described in Chapter 2 diffraction occurs when the Laue condition for the diffraction vector

$$\vec{q} = \vec{g} \tag{72}$$

is fulfilled, where $\vec{g}$ is a reciprocal lattice vector

$$\vec{g} = \sum_i n_i \vec{b}_i \tag{73}$$

for integers n_i. This condition is derived from Fourier analysis, where the Fourier transform of a periodic function such as the electron density $\rho(\vec{r})$ at a point at $\vec{r}$ on an undistorted lattice is an infinite sum of complex exponentials, $\rho(\vec{r}) = \sum_{\vec{g}} \tilde{\rho}_{\vec{g}} \exp(i\vec{g} \cdot \vec{r})$. For all translations

$$\vec{t} = \sum_i m_i \vec{a}_i \tag{74}$$

with integer m_i that leave the lattice invariant such that $\rho(\vec{r}+\vec{t}) = \rho(\vec{r})$ we have from the orthogonality relations:

$$\exp(i\vec{g} \cdot \vec{t}) = 1 \tag{75}$$

Therefore the distorted lattice must be locally periodic for lattice diffraction to take place. The translations

$$\vec{t}' = \sum_i m_i \vec{a}_i' = \mathbf{F}\vec{t} \tag{76}$$

should leave the distorted lattice (locally) invariant. Thus the condition for lattice diffraction implies that

$$\exp(i\vec{g}' \cdot \vec{t}') = 1 \tag{77}$$

where we assume that we can write the distorted reciprocal lattice vectors in terms of the undistorted reciprocal lattice vectors as:

$$\vec{g}' = \sum_i n_i \vec{b}_i' = \mathbf{H}\vec{g} \tag{78}$$

This is fulfilled for:

$$\vec{g}' \cdot \vec{t}' = \vec{g}\mathbf{H}^T \cdot \mathbf{F}\vec{t} = \vec{g} \cdot \vec{t} \Rightarrow \mathbf{H}^T = \mathbf{F}^{-1} \tag{79}$$

Therefore:

$$\mathbf{H} = \left(\mathbf{H}^T\right)^T = \left(\mathbf{F}^{-1}\right)^T \tag{80}$$

To first order in the displacement gradients we have $|\mathbf{F}| = 1 + \sum_i \beta_{ii}$ and thus $1/|\mathbf{F}| = 1 - \sum_i \beta_{ii}$. Writing out the elements of the inverse of $\mathbf{F}$:

$$\mathbf{F}^{-1} = \frac{1}{1+\sum_i \beta_{ii}} \begin{bmatrix} \begin{vmatrix} 1+\beta_{22} & \beta_{23} \\ \beta_{32} & 1+\beta_{33} \end{vmatrix} & \begin{vmatrix} \beta_{13} & \beta_{12} \\ 1+\beta_{33} & \beta_{32} \end{vmatrix} & \begin{vmatrix} \beta_{12} & \beta_{13} \\ 1+\beta_{22} & \beta_{23} \end{vmatrix} \\ \begin{vmatrix} \beta_{23} & \beta_{21} \\ 1+\beta_{33} & \beta_{31} \end{vmatrix} & \begin{vmatrix} 1+\beta_{11} & \beta_{13} \\ \beta_{31} & 1+\beta_{33} \end{vmatrix} & \begin{vmatrix} \beta_{13} & 1+\beta_{11} \\ \beta_{23} & \beta_{21} \end{vmatrix} \\ \begin{vmatrix} \beta_{21} & 1+\beta_{22} \\ \beta_{31} & \beta_{32} \end{vmatrix} & \begin{vmatrix} \beta_{21} & 1+\beta_{11} \\ 1+\beta_{32} & \beta_{31} \end{vmatrix} & \begin{vmatrix} 1+\beta_{11} & \beta_{12} \\ \beta_{21} & 1+\beta_{22} \end{vmatrix} \end{bmatrix} \tag{81}$$

$$= \left(1 - \sum_i \beta_{ii}\right) \begin{bmatrix} 1+\beta_{22}+\beta 33 & -\beta_{12} & -\beta_{13} \\ -\beta_{21} & 1+\beta_{11}+\beta_{33} & -\beta_{23} \\ -\beta_{31} & -\beta_{32} & 1+\beta_{11}+\beta_{22} \end{bmatrix} \tag{82}$$

$$= \begin{bmatrix} 1-\beta_{11} & -\beta_{12} & -\beta_{13} \\ -\beta_{21} & 1-\beta_{22} & -\beta_{23} \\ -\beta_{31} & -\beta_{32} & 1-\beta_{33} \end{bmatrix} \tag{83}$$

$$= \mathbf{I} - \beta \tag{84}$$

Therefore, to first order in β_{ij} it is found that $\mathbf{H} = (\mathbf{I} - \beta)^T = \mathbf{I} - \beta^T$ and the relation between the distorted and undistorted reciprocal lattice vectors are:

$$\vec{g}' = \left(\mathbf{I} - \beta^T\right)\vec{g} \tag{85}$$

DFXRM maps the spatial variations of the lattice normal $\vec{g}'$ in terms of the deviations from $\vec{g}_0 = g_0\hat{z}$ where $\hat{z}$ denotes the mean lattice orientation. Maps are obtained in terms of the counter-clockwise tilts u around x and v around y as well as a small change τ of the scattering angle 2θ, which is proportional to the deviation in axial strain ϵ:

$$\epsilon = -\frac{1}{2}\tau \cot\left(\frac{1}{2}2\theta\right) \tag{86}$$

With $g' = 2\pi/d_0(1+\epsilon)$ the deviation in length is:

$$g' = (1-\epsilon)g_0 \tag{87}$$

Therefore the distorted lattice normal is:

$$\vec{g}' = \begin{bmatrix} g'_x \\ g'_y \\ g'_z \end{bmatrix} = g_0 \begin{bmatrix} v \\ -u \\ 1-\epsilon \end{bmatrix} \tag{88}$$

$$= \left(\mathbf{I} - \beta^T\right) g_0 \hat{z} \tag{89}$$

Thus by means of DFXRM three components of the distortion tensor may be determined:

$$\beta_{31} = \gamma_y - \phi_y = -v \tag{90}$$

$$\beta_{32} = \gamma_x + \phi_x = u \tag{91}$$

$$\beta_{33} = \varepsilon_z = \epsilon \tag{92}$$

The remaining elements of β are not accessible from the DFXRM measurements unless complementary measurements are performed on other $\vec{g}$-vectors with components perpendicular to the first one, which is usually not done because of geometric restrictions on the instrument.

3.3.3 Dislocation density

The derivatives of the components of the distortion tensor are related to the dislocation density tensor α_{ij} as shown in Chapter 2:

$$\alpha_{ij} = -\varepsilon_{jkl}\partial_k \beta_{il} \tag{93}$$

Within the linear elasticity framework the total dislocation density tensor is given as the sum over contributions from all dislocations present. Thus following [Nye1953] the dislocation density is given by

$$\alpha_{ik} = \sum_t b_i^t \xi_k^t \rho^t(\vec{r} - \vec{r}^t) \tag{94}$$

It is assumed that any dislocation line may be decomposed into its pure edge and screw components and the sum is to be taken over all types of these with number density given by ρ.

From the 3D maps of orientation and strain obtained by DFXRM it is possible to calculate all three spatial derivatives. However, since only the three

components β_{3i} are available only the three components α_{3i} may be obtained:

$$\alpha_{31} = \partial_z u - \partial_y \epsilon \quad (95)$$

$$\alpha_{32} = \partial_z v + \partial_x \epsilon \quad (96)$$

$$\alpha_{33} = -\partial_x u - \partial_y v \quad (97)$$

For comparison, EBSD measurements of deformed samples of high dislocation density provide five components and one combination of α-components and from these the number density of geometrically necessary dislocation in each voxel may be estimated [Pantleon2008]. However, the resolution of EDSB limits this approach to high dislocation content and multiple dislocations in each voxel. With DFXRM the resolution is order of magnitude better and by this approach to data analysis it is in principle possible to map single dislocations and structures of very low dislocation content. The first results as presented in Chapter 4 are promising.

3.4 Focusing the microscope

For high resolution mapping as proposed above to be successful it is crucial that the microscope is properly focused. Otherwise individual images in the data-series may be blurred or shifted with respect to each other. In this section the thesis work on focusing of the x-ray microscope is discussed with emphasis on how to focus the microscope to a good enough precision to avoid shifts of the images in a data series with respect to each other. Some problems regarding the currently applied focusing strategy are sketched and a new focusing routine is proposed for future testing.

3.4.1 The focused microscope

Consider an x-ray microscope consisting of a sample, an objective, and a detector, see Figure 34. The incoming beam is condensed to a line beam through the condenser and knife-scans are performed to optimize the height of the beam at the sample position. The sample center-of-rotation is aligned to the center of the condensed beam. The microscope is then focused by iteratively optimizing the position of the objective along the different degrees of freedom.

The objective is a CRL made from N lenslets each of radius-of-curvature R and thickness T and the optical axis is defined by the central axis of the objective. Using a ray transfer formalism the effect of the objective on a ray

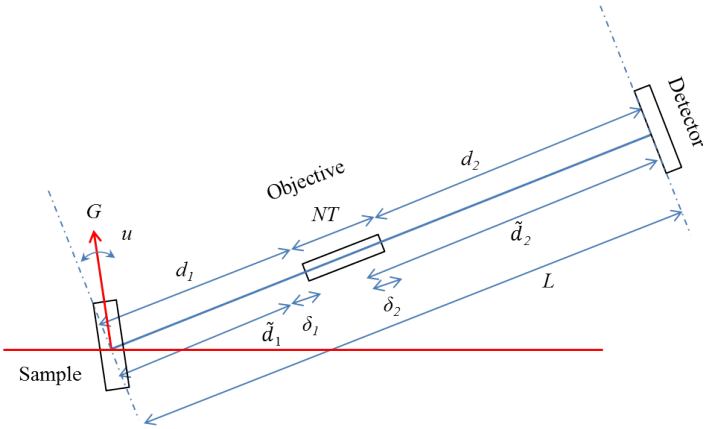

Figure 34: **Microscope in focus** A microscope consisting of sample, objective, and detector. The lensmakers equation is fulfilled, the sample is in the sample plane an a focused image is obtained at the detector. Parameters are defined including out-of-focus shifts etc.

entering the objective at a perpendicular distance y_o and angle α_o the optical axis is given by the matrix $\mathbf{M}^N$:

$$\mathbf{M}^N = \begin{bmatrix} M_{11}^N & M_{12}^N \\ M_{21}^N & M_{22}^N \end{bmatrix} = \begin{bmatrix} \cos(N\phi) & f\phi\sin(N\phi) \\ -\frac{1}{f\phi}\sin(N\phi) & \cos(N\phi) \end{bmatrix} \tag{98}$$

Here the focal length of a single lens is given by $f = R/2\delta$, where δ is the refractive decrement of the lens material, and $\phi = \sqrt{T/f}$. The sample-to-objective distance is d_1, the objective-to-detector distance d_2, and the sample-to-detector distance is $L = d_1 + d_2 + NT$, see Figure 34. For a signal diffracted from a sample point at a perpendicular distance y_s and at an angle α_s to the optical axis, the detector position y_D and resulting angle α_D of the signal is given by the total transfer matrix $\mathbf{K}$:

$$\begin{bmatrix} y_D \\ \alpha_D \end{bmatrix} = \mathbf{K} \begin{bmatrix} y_s \\ \alpha_s \end{bmatrix} \tag{99}$$

The elements of the matrix are:

$$K_{11} = M_{11}^N + d_2 M_{21}^N = \cos(N\phi) - \frac{d_2}{f\phi}\sin(N\phi) \tag{100}$$

$$K_{12} = M_{12}^N + d_1\left(M_{11}^N + d_2 M_{21}^N\right) + d_2 M_{22}^N \tag{101}$$

$$K_{21} = M_{21}^N \tag{102}$$

$$K_{22} = d_1 M_{21}^N + M_{22}^N \tag{103}$$

The microscope is focused for a given configuration when there is no angular dependence and all rays from a sample point meet in the same detector point, that is $K_{12} = 0$, which gives the lensmakers equation as given earlier in this chapter. When this imaging condition is fulfilled the magnification is given by:

$$\mathcal{M} = -\frac{y_D}{y_s} = -K_{11} \tag{104}$$

A typical objective consists of $N = 72$ lenses with $T = 1.6$ mm, $R = 50\mu$m, $f = 16.6$ m, and $\phi = 0.0098$. The microscope distance $L = 5.0$ m gives $d_2 = 4.65$ m and $d_1 = 0.20$ m. Thus for this setup $\mathcal{M} = 17.8$, $M_{11}^N = M_{22}^N = 0.76$, $M_{12}^N = 0.11$ m, and $M_{21}^N = -4.0\text{m}^{-1}$.

3.4.2 Focusing algorithms

The currently applied focusing strategy at ID06 is a standard focusing algorithm which takes a series of images obtained at different positions of the objective as input and calculates the maximum sharpness of the image series using different mathematical methods. Two examples of typical images are shown in Figure 35, the one on the left is 1.2 cm out-of-focus and on the right is the image of best focus as determined by the focusing algorithm. The focused image shows distinct structure in more faint areas, whereas these are blurred in the out-of-focus image. The image sharpness as determined by the algorithm using different approaches is shown in Figure 36. Even for this series that covered a range of 2 cm the image sharpness is not convincingly peaked and it seems that this method of focusing cannot provide sufficient accuracy for high resolution measurements.

Possible problems include that in the microscope setup the illuminated plane is tilted with respect to the optical axis, making it difficult to focus all parts of the horizontally extended sample plane at the same time. Furthermore, if the optical axis is tilted with respect to the sample-to-detector line the offset angle changes with the objective translation. From geometrical considerations it may be derived that the offset angle α_0 at $\delta = 0$ changes by $\Delta\alpha = \delta\alpha_0/d_1$. Assuming a 1° offset and a sample-to-detector distance of 20 cm a translation of the objective by 1 cm gives rise to a change in angle of 0.05° which would show a different spatial distribution. Also, it is observed in Figure 35 that the more faint structures undergo the most obvious increase of sharpness. However, the more intense structures will completely dominate the outcome of the focusing algorithm.

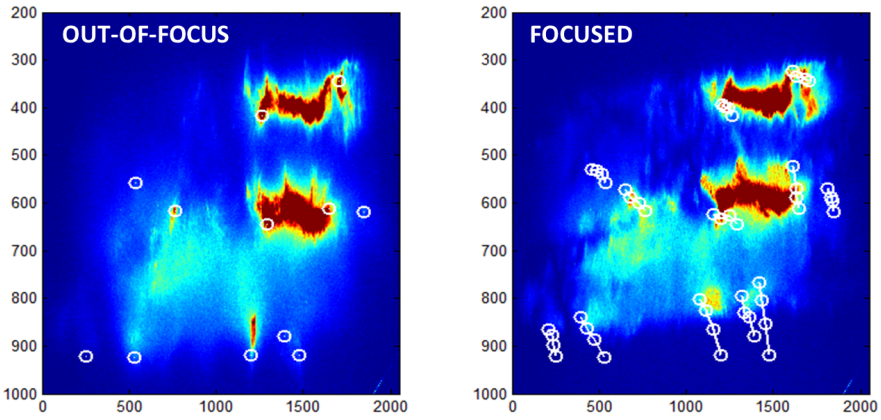

Figure 35: **Focus and out-of-focus** Two detector images of a grain. On the left the microscope was 12 mm out-of-focus and on the right the microscope is in focus. 12 points were traced through a 21 mm scan of the objective position along the optical axis. The traces may be utilized for focusing. Raw data courtesy of A. Bucsek.

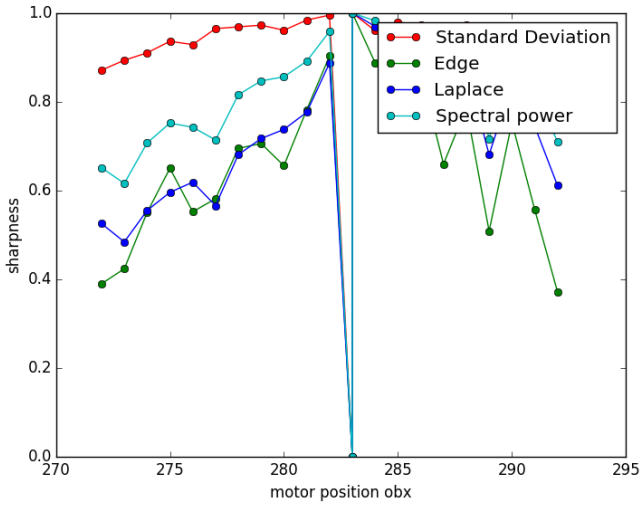

Figure 36: **Focusing algorithm** The output of the focusing algorithm. The image sharpness is not distinctively peaked. The central dip is an artefact produced purposely by the algorithm. Courtesy of C. Yilderim.

3.4.3 General equations for out-of-focus

Consider a slightly out-of-focus situation where $\tilde{d}_1 = d_1 + \delta_1$ and $\tilde{d}_2 = d_2 + \delta_2$ and the sample-to-detector distance L is unaltered to first order in the displacements

δ_1 and δ_2. The position and angle of the diffracted ray at the detector

$$\begin{bmatrix} \tilde{y}_D \\ \tilde{\alpha}_D \end{bmatrix} = \tilde{\mathbf{K}} \begin{bmatrix} y_s \\ \alpha_s \end{bmatrix} \tag{105}$$

may be derived by introducing the displacements as translations before and after the microscope:

$$\tilde{\mathbf{K}} = \begin{bmatrix} 1 & \delta_2 \\ 0 & 1 \end{bmatrix} \begin{bmatrix} K_{11} & K_{12} \\ K_{21} & K_{22} \end{bmatrix} \begin{bmatrix} 1 & \delta_1 \\ 0 & 1 \end{bmatrix} \tag{106}$$

$$= \mathbf{K} + M_{21}^N \begin{bmatrix} \delta_2 & \delta_1(d_2 - f_N) + \delta_2(d_1 - f_N) \\ 0 & \delta_1 \end{bmatrix} \tag{107}$$

3.4.4 Objective translation

Translation of the objective along the optical axis $\delta_1 = -\delta_2 = \delta$, see Figure 38, away from the focused configuration at $\delta = 0$ results in a ray transfer matrix given by:

$$\tilde{\mathbf{K}} = \mathbf{K} + \delta M_{21}^N \begin{bmatrix} -1 & d_2 - d_1 \\ 0 & 1 \end{bmatrix} \tag{108}$$

Thus a small tilt of the sample $u = \Delta\alpha$ that conserved the position of y_s will shift the position of the diffraction spot from a single crystalline point by

$$\Delta y_D = \delta M_{21}^N (d_2 - d_1)\Delta\alpha = -\delta \left(\mathcal{M} - \frac{1}{\mathcal{M}} \right) u \tag{109}$$

provided that the signal is still allowed through the objective at the tilted position. For example the setup described above has $\mathcal{M} - 1/\mathcal{M} = 17.7$ and with an effective pixel size of 1.6 μm, the objective should be focused to within 50 μm to have shifts smaller than 1 pixel for sample tilts of $u = 0.1^\circ = 1.7$ mrad.

A series of images showing large shifts of the measured structure as a function of tilt of the sample is shown in Figure 37. Such image shifts constitute a huge problem for the data analysis, which is based on the assumption that the images are (almost) aligned through the data series, see Chapter 4. Furthermore, it is possible that the diffraction peaks from individual crystallites in the sample plane will move independently of each other, which would make the proposed data analysis impossible.

If the objective is translated along the optical axis a shift is expected:

$$\Delta y_D = \delta M_{21}^N \left(-y_s + (d_2 - d_1)\alpha_s \right) \approx \delta y_s M_{21}^N \left(\frac{d_2}{d_1} - 2 \right) \tag{110}$$

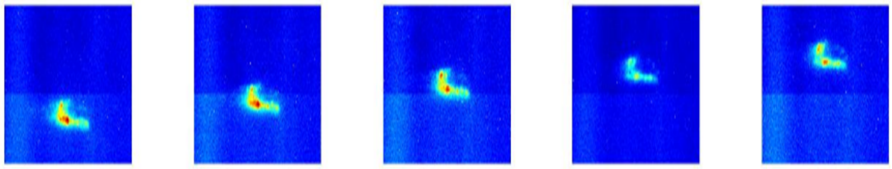

Figure 37: **Observation of shifts** The same feature in consecutive images shifts many pixels as a function of the sample tilt. The substantial shift observed in this example has not been explained by linear effects as described in this section and may be due to non-linear effects.

For simplicity it is assumed that the angle is $\alpha_s = y_s/d_1$. From this expression it is evident that on translating the objective along the optical axis by an amount δ away from the sample the observation point y_D will move away from the point where the optical axis intersects the detector plane. Furthermore, the shift is proportional to y_s that is to the distance of the point in the sample to the optical axis.

3.4.5 Out-of-focus blurring

The images obtained with the microscope are sharp for a range of different objective settings since the depth of field of the condensed line beam is large, on the order of the sample size (300 μm). This is mainly due to the narrow diffraction cone allowed through the objective from each position in the sample. The out-of-focus blurring of the diffraction spot from a point source is calculated from the previously derived relation between Δy_D and the angle, in this case set to be the numerical aperture NA of the objective, $\Delta y_D = \delta \left(\mathcal{M} - \frac{1}{\mathcal{M}} \right) NA$. An estimated value for the numerical aperture is $0.001^\circ = 0.017$ mrad. Thus for out-of-focus translation of the objective of $\delta = 1$ cm a point source will appear merely 2 pixels wide and the image will appear relatively sharp even for this situation. However, under slight out-of-focus conditions the position on the detector of the individual diffracted signal may move during the data acquisition tilt series according to the relation derived above. Therefore the sharpness of the microscope is high, but the images may be shifted through a tilt-series or the individual parts of an image may shift with respect to each other and it is important for the success for an experiment to focus the microscope properly.

3.4.6 Aligning the optical axis

The position of the intersection of the optical axis with the sample plane should be centered with respect to the structure under investigation. This is to avoid reflection and non-linear effects occurring in the lenslets at non-normal ray incidence on the surfaces as well as to minimise the effects of the microscope being slightly out-of-focus.

For alignment of the optical axis it may be utilized that the shift of a point on the detector is proportional to the translation of the objective as well as to the distance of the sample point to the optical axis as derived above. Therefore, tracing several identifiable points in a detector image of the sample through a series of translations of the objective parallel to the optical axis should yield a collection of lines intersecting at the position of the optical axis on the detector. If this does not provide an unambiguous picture there is further information in the distance moved by each point since the points further away from the optical axis will move further than the points closer to it. The objective should be adjusted accordingly and the measurement repeated if necessary.

If the tilt of the optical axis is initially large $> 1^\circ$ the tracing may be blurred by changes in the ray angle giving rise to a different observed shape as described above.

This idea was tested for a series of previously acquired focusing data, see Figure 35. Twelve points were traced through a series of 21 steps of 1 mm each. The traces do not single out to a specific point. However, all lines extend from lower right to upper left and the distance moved of individual points seem to decrease towards the upper left. Thus there is a good indication that the optical axis intersected the detector somewhere up there and the objective should be rotated to adjust for this.

To check whether the structure under investigation is aligned to be in the center-of-rotation the sample may be tilted slightly and the measurement repeated. If the position of the optical axis has moved with respect to the structure, the center-of-rotation could need adjustment.

3.4.7 Focusing the objective

With the optical axis aligned with the structure under investigation the sample-to-objective should be adjusted to focus the microscope. If the objective is placed at an out-of-focus position δ_1 the individual points in the images should

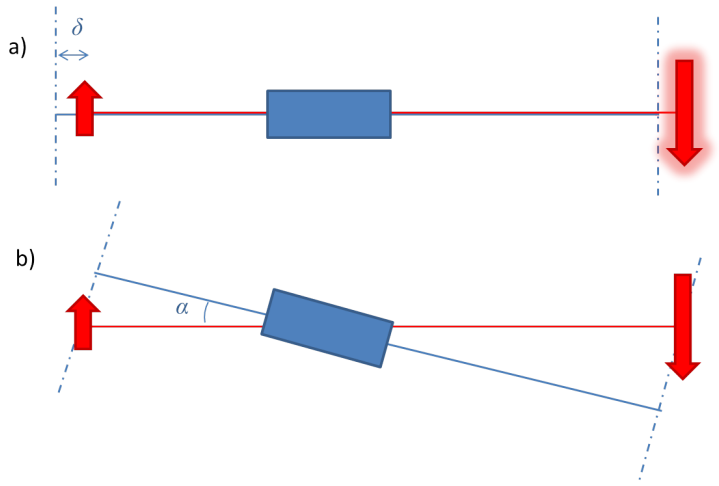

Figure 38: **Configurations** a) The objective is misplaced so the lensmakers equations is not fulfilled and the image on the detector is blurred. b) The optical axis is tilted with respect to the sample-to-detector line. The microscope is focused to this configuration, however it is not know what problems with shifts in the data series and other artefacts this may cause.

move according to the relation derived above upon tilting the sample. A tilt series should be obtained in v since the angular resolution of this tilt is lowest and the probability of seeing the same point in several images is therefore largest here. The slopes A_1 of the shifts as functions of tilt should be given by the magnification of the focused microscope and δ_1, see above. The procedure should be repeated for another objective position at δ_2 such that $\Delta = \delta_2 - \delta_1$ is known and on the order of centimetres. Now the magnification may be determined from the slopes in the two series since

$$\frac{A_2 - A_1}{\Delta} = \mathcal{M} - \frac{1}{\mathcal{M}} \tag{111}$$

In turn the absolute position for the objective to focus the microscope is obtained as:

$$\delta_1 = \Delta \frac{A_1}{A_2 - A_1} \tag{112}$$

This scheme for focusing has yet to be tested at the instrument. A fast and reliable way of identifying and tracing structural characteristics is necessary for the successful implementation.

3.5 Sample

In this section the details of the sample preparation and measurements are presented. For annealing studies of recrystallization the 99.5% aluminium alloy AA1050 is a good choice. The material is well characterised and has a long history of sample of choice for proof-of-concept x-ray studies.

A sheet of the material was cold-rolled to 50% reduction in thickness and cut to $(0.3 \times 0.3 \times 1)\text{mm}^3$ specimens with 0.5 mm cubic handles. The samples were annealed at 325°C for 40 and 50 minutes, respectively. At this temperature the kinetics are fast enough to induce growth *in situ* but slow enough to allow many time-steps to be recorded during the recrystallization process. The specimens were glued to glass rods with ceramic glue and placed in Cu-sample holders in the instrument. The samples were mounted with the diffraction vector parallel to the rolling direction (RD) to study recrystallizing grains of cube-like orientation with (002) parallel to RD.

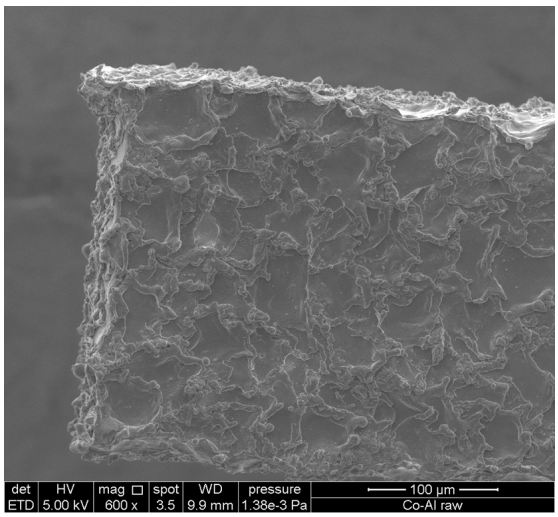

Figure 39: *Sample surface* TEM images of the sample surface. Courtesy of A. Fueller.

4 Recrystallizing grains with interior structure

The boundary migration of recrystallizing grains as they grow into the deformed matrix has been observed to be highly heterogeneous and related to the morphology and texture of the surrounding subgrain structure, see previous chapters. However, the currently well-established 3D mapping techniques are not suitable for studies of this correlation, either because the resolution is too low to distinguish individual subgrains and boundary topology, because the acquisition times are too long to study dynamics or because 3D visualisation requires sectioning of the sample.

In this chapter the first application of the novel x-ray imaging technique dark field microscopy (DFXRM) within recrystallization is presented. It is demonstrated how the internal variations of lattice orientation and axial strain as well as the shape of bulk recrystallizing grains may be mapped with sub-micron spatial resolution and millidegree angular resolution within the extend of a few hours. These results were presented in [**Paper1**, **Paper2**] and this chapter gives a full description of the experimental investigation, data analysis and interpretation of observations. The internal variations are characterized in terms of a network of ultra low angle boundaries and the relation to the external grain boundary is discussed. The internal boundaries are characterised and their evolution during annealing is investigated statistically.

Furthermore, a new approach to the analysis of DFXRM-data in terms of distortion fields and dislocation densities as described in the previous chapter is demonstrated [*Paper in preparation*] and the chapter is concluded with a description of the experimental problems identified during the data analysis.

Except from where other sample details are specifically stated, all data and results presented in this section are obtained for partly recrystallized aluminium AA1050 which had been cold-rolled to 50% reduction in thickness and annealed for 50 minutes at 325°C to obtain an almost 50% recrystallized structure (see description of the samples in Chapter 3).

4.1 Mapping of mosaicity and strain

By means of the DFXRM-setup a selected diffraction peak for a single crystallite embedded in the bulk of a polycrystalline structure may be analysed in detailed by measuring a narrow range of angles out of the full diffraction peak at a time. As described in detail in Chapter 3 the objective lens selects the angles

and magnifies this signal to yield a real space image of the distribution of that particular corresponding lattice orientation and lattice parameter within the illuminated plane of the sample. Data for the full diffraction peak is collected by acquiring real space images at each sample orientation in a mesh of small sample tilts (u, v). For strain measurements the objective lens is simultaneously translated and tilted to obtain different 2θ-values and a data series consisting of direct space images for each configuration of $(u, 2\theta)$ in a mesh is collected. From such 4D data sets maps of the intrinsic spatial variations of lattice orientation and axial strain are obtained. The necessary data analysis and resulting maps are presented in this section. 3D maps may be generated by stacking data for consecutive layers obtained by repeating the measurements after a small vertical translation of the sample.

4.1.1 Shapes in direct and reciprocal space

An example of a full data set is shown in Figure 40 for a 300 nm thick illuminated layer of a recrystallizing grain. The data set consist of 41 × 21 images covering 0.2° in both tilt directions u and v. For each orientation of the sample a direct space image of the diffracted intensity at that particular orientation was acquired. The detector pixel size in this example was 200 nm × 400 nm (horizontal × vertical). The larger grain also mapped in detail had a voxel size of 100 nm × 200 nm × 200 nm and double the step size in the mesh in orientation space.

The total orientation distribution for the illuminated slice of the recrystallizing grain is obtained as the integrated intensity in each image, see the bottom right image in Figure 40. The diffraction of a perfect crystal as smeared out to the instrumental resolution would give rise to a narrow Gaussian orientation distribution. However, the measured orientation distribution clearly deviates from a Gaussian distribution, indicating that the grain possesses internal variations of lattice orientations on the order of 0.1°.

Adding all images in a tilt series gives the total diffracted intensity from the illuminated layer of the grain (at the selected lattice spacing), see the bottom left of Figure 40. The shape of the grain is apparent and may be obtained from the intensity distribution by deciding on a cut-off intensity, see Figure 41a. In agreement with recent observations (see Chapter 2 and 3) the grain boundary possess protrusions and retrusions. DFXRM only provides information on a sin-

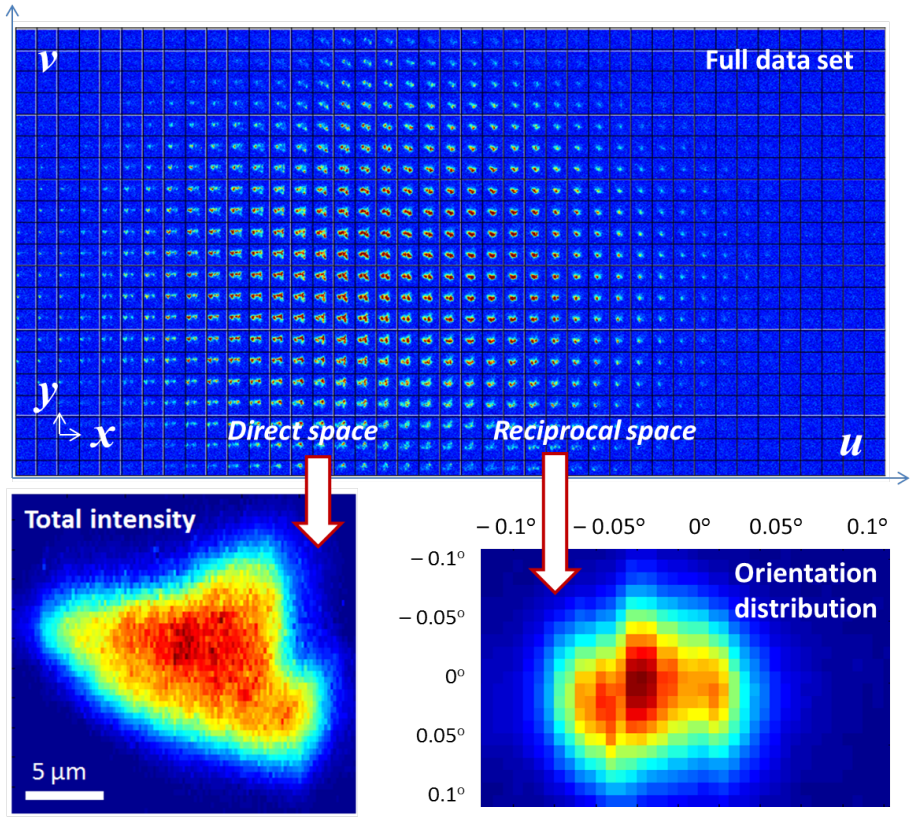

Figure 40: **Data in 4D** An example of a full data set obtained for a tilt series in (u, v) covering $0.2°$ in both angles in 41 and 21 steps, respectively. Direct space images were acquired at each orientation with a voxel size of $0.1 \times 0.4 \times 0.3 \mu\text{m}^3$. The integrated intensity in each image gives the total orientation distribution in angular space, whereas the sum of all images in the series yields the total intensity in direct space which reveals the grain shape. The illuminated layer is tilted to $2\theta/2$ with respect to the rolling direction.

gle grain and not its surroundings, which makes the uncertainty in the position of the boundary somewhat larger than the pixel size. Nevertheless, the far from spherical shape of the recrystallizing grain is visualised with a spatial resolution on the order of 1 μm.

The cross-sectional area of the grain is $15 \times 20 \mu\text{m}^2$ in the illuminated plane and the roughness of the grain boundary is on the order of a few microns with the smallest distinguishable features being protrosions and retrusions that are 2-3 μm wide. In Figure 41b the shape of a larger grain of cross-sectional area

$150 \times 70\mu m^2$ is shown. The boundary possesses protrusions and retrusions similar to those observed for the smaller grain along the majority of the length of the boundary and a zoom along the red line is provided in 41d. However, along the blue line the boundary is flat as shown in the zoom in 41c. This could indicate that this is a boundary segment towards a neighbouring recrystallizing grain.

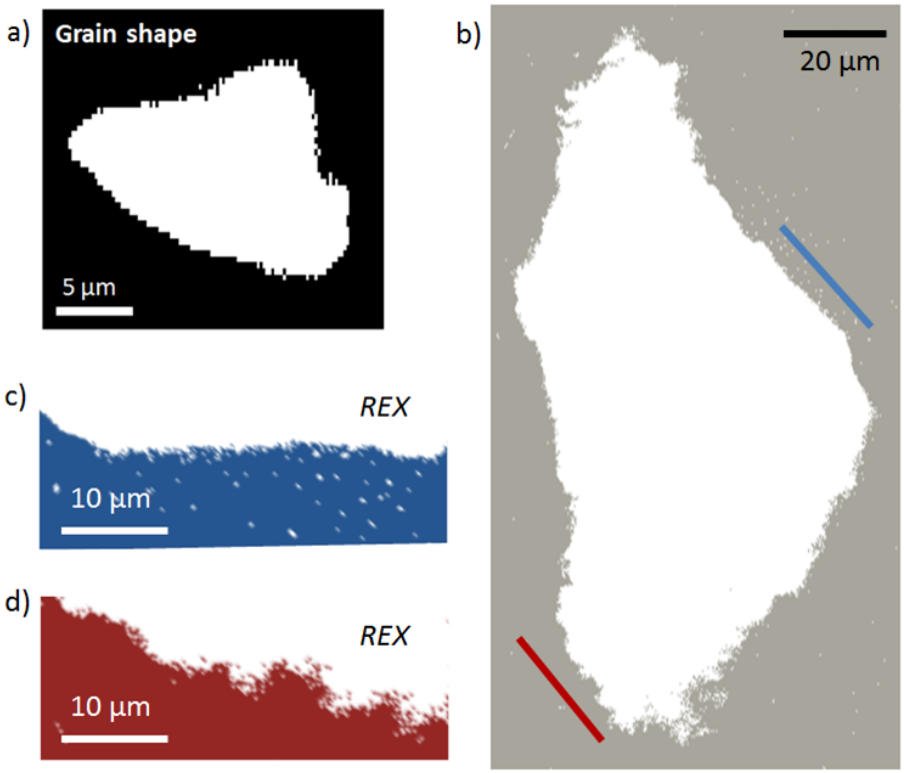

Figure 41: **Grain shapes** The outline of the illuminated layer of the grain is obtained by introducing a cut-off intensity. a) The shape of the boundary of a $15 \times 20\mu m^2$ recrystallizing grain. b) The shape of the boundary of a $150 \times 70\mu m^2$ grain. c) Flat boundary segment along the blue line. White points within the blue are artefacts due to the detector. d) Boundary protrusions and retrusions along the red line in b). Combining consecutive layers a 3D map of the grain shape may be obtained with sub-micron resolution.

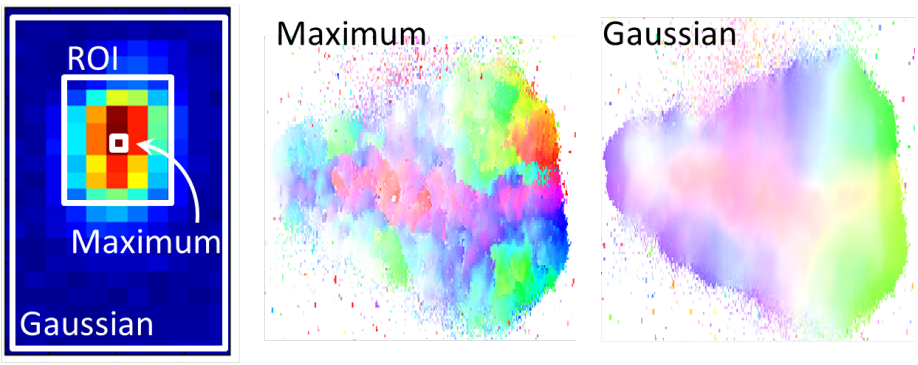

Figure 42: **Orientation from maximum and Gaussian fit** The orientation is assigned to each voxel from the orientation distribution for that particular voxel either directly from the pixel of maximum intensity in the orientation distribution, from a Gaussian center-of-mass fit to the full orientation distribution or a similar fit to a selected region-of-interest (ROI) centered at the pixel of highest intensity (see below). The color indicates orientation, but is not absolute for this figure.

4.1.2 Local orientation distributions

For each voxel a local orientation distribution in (u, v) can be obtained by extracting the intensity of that particular voxel through the whole data series. From this distribution an orientation may be assigned to the voxel either directly from the tilts associated with the pixel of maximum intensity or by a Gaussian center-of-mass fit to the whole distribution or a selected region-of-interest (ROI) centered at the pixel of highest intensity, see Figure 42.

There are advantages and drawbacks of all three methods: Choosing the maximum, the variations in orientation will give rise to abrupt changes in assigned orientation, however the angular resolution is limited to the step size of the experiment. Furthermore, if several lattice orientations are present within the same voxel and give rise to peaks of similar intensity in the orientation distribution, the method only acknowledges the one of highest intensity and ignores the rest.

A Gaussian center-of-mass fit to the whole orientation distribution yields smooth maps of the orientation variations but may smear out variations, especially if two distinct lattice orientations are present in the same voxel. In that case the orientation distribution contains two distinct peaks but the fit

will assign the average, which my be quite different from the actual orientations present.

The ROI-method smooths the regions were more than one but similar orientations are present, but yields abrupt changes in regions with two or more distinct orientations. However, since this method identifies the pixel of maximum intensity as the center of the fit, it is also liable to misrepresentations when two or more orientations are present and it may be argued that the weighted average over orientations present in each voxel is a better way of representing the lattice orientation in that voxel, than it is to select one of the orientations only.

It is evident from Figure 42 that the maximum method gives many sharp features whereas these are smeared out by the Gaussian fit method. It is not obvious which method represents the actual structure best. In the following either the ROI method or the Gaussian method is applied.

Some data series exhibited marked shifts in overall grain position through the series and a substantial effort has been put into trying to correct for this. However, it is not obvious what the optimized relative position that represents reality is. Since it was concluded that even for moderate shifts the quantitative appearance of the mosaicity maps was not altered, no corrections have been applied.

4.1.3 Mosaicity

When an orientation is assigned to the individual voxels from the local orientation distributions a mosaicity map may be obtained from appropriately color-coding each voxel according to the assigned orientation. The mosaicity map shown in Figure 43 is obtained from 3×5 pixels ROI fits around the pixel of maximum intensity. The key to the color-code is shown in the figure with the contours of the total orientation distribution overlaid.

It is observed that the grain is subdivided into domains of uniform orientation. The local orientation distributions which are shown in the figure for four of these domains reveal that the lattice orientation is distinct and uniform within each domain. The domains are seperated by regions where the orientation changes abruptly and the misorientation between the domains is on the order of 0.1° or less. The sizes of the domains vary from 2 to 7 μm, which is comparable to the size of the (larger) subgrains in the deformed structure,

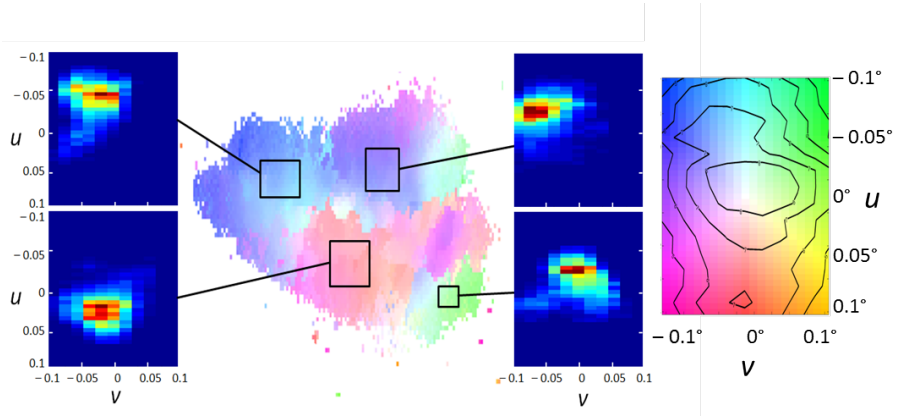

Figure 43: **Mosaicity map** The orientation of each voxel was assigned from a 3×5 pixels ROI fit. The mosaicity map was obtained from color-coding the voxel according to the assigned orientation. The color key is shown with an overlaid contour map of the total orientation distribution. The local orientation distribution of four distinct regions are included. Domains of uniform orientation are observed with sharp boundaries between them and orientation differences across the boundaries on the oreder of 0.1° or less.

that the recrystallizing grain is growing into, see previous chapters. Thus this internal structure may be related to the subgrain structure that the recrystallizing grain grew from. Further investigation of the properties of this internal structure in recrystallizing grains is presented below.

Mosaicity maps provide an easy overview of the internal variations of the lattice orientation. It should be note, that only two out of three orientational degrees of freedom are represented in the map, since DFXRM measures orientation as the deviation of the lattice normal. Therefore the in-plane lattice orientation is completely unknown, but it is assumed that the variations in this direction are similar in size and distribution to the observed directions. The in-plane orientation may be determined if the mapping is repeated for lattice planes with a perpendicular component. However, this was not done for the present experiments.

4.1.4 Gaussian moments

The Gaussian center-of-mass fit has a further advantage since it may easily be extended as follows: If it is assumed that the local orientation distributions are

approximately Gaussian, the Gaussian moments of the local orientation distributions over the whole (u,v)-range may be easily calculated from projections of the distributions onto the two axes. The zero-order moment gives the Gaussian mean or fitted orientation in u and v, respectively, as described above. The higher order moments quantifies the shape of the distribution and thus may reveal more about the variations in the local orientation of the grain.

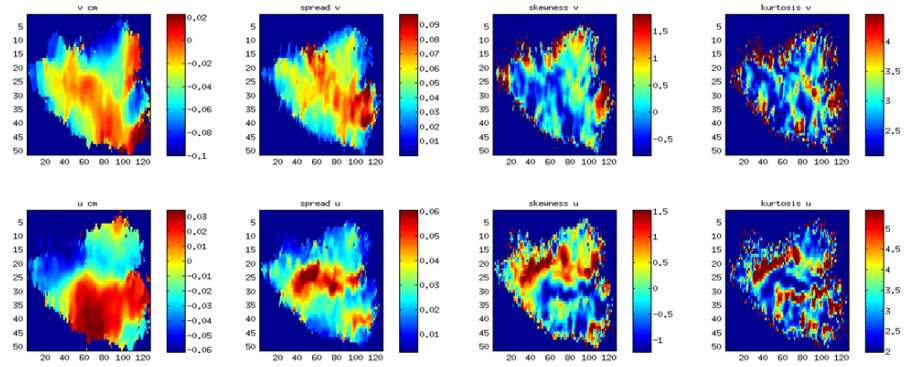

Figure 44: **Gaussian moments** The distributions of the zeroth to third local Gaussian moments obtained from the local orientation distributions for each individual voxel. The top row are calculated for the distribution projected along v and the second row for projection along u. The axes are given in number of detector points and the colorbars indicate the scale of the different moments. See the main text for a discussion.

The first moment gives the variance or spread of the distribution, which is in terms of the orientation distributions is expected to be smaller for more uniform diffracting crystal lattice. Therefore, this parameter should be small in the center of the domains and larger where the boundaries are since multiple orientations may be present here. The second moment, the skewness, is a measure of the asymmetry of the distribution, which is expected to be non-zero if multiple orientations are present in a voxel, so that the orientation distribution consists of several peaks of different intensity. Furthermore, the skewness is expected to change sign across an interior boundary as the dominant orientation changes and thus the shoulder in the distribution changes side. Away from the boundary the shoulder decreases and disappears, thus the skewness should approach zero away from the boundary. The third moment, the kurtosis, is a measure of the

peaked-ness of the distribution. The kurtosis is larger than 3 for a distribution that is sharper peaked than a Gaussian and smaller than 3 for distributions which are flatter than a Gaussian. Thus where more than one orientation is present the kurtosis is expected to be small and in single crystalline regions the distribution is expected to be Gaussian so the kurtosis should be equal to 3 if the distribution is properly resolved in angular space. Values larger than 3 would indicate under-sampling in angular space.

The zeroth to third Gaussian moments along the two tilt directions are plotted in Figure 44, where the top row is the v-components and the bottom row is the u-components. The fitted orientation in u reveals an abrupt change along an almost horizontal line starting from the retrusion in the exterior boundary on the right. This boundary-like feature appears in the variance or spread as an increase along the same line. Likewise, for v there seems to be a central line starting from the left and bending downwards with thin branches towards the exterior boundary at several places. For u in particular it appears that change in sign of the skewness and a low kurtosis is coincident with abrupt changes in orientation as expected. Also the variance or spread is increased in these regions. A large kurtosis greater than 3 is observed for u on both sides of the central boundary, which indicates that this direction was under-sampled since the Gaussian shape of the orientation distribution has not been fully resolved.

This simple method provides insight into the internal structure of recrystallizing grains and may be applied as a means for fast on-site analysis of acquired data while the experiment is ongoing. Internal variations in orientation are easily visualized and interpreted in terms of internal boundary structures and sampling strategies may be adjusted as a result of the indications of the calculated kurtosis.

4.1.5 Strain

Before the observed internal structure is investigated further, strain maps are introduced here for completeness. Strain maps may also be obtained from DFXRM-measurements. Preferably, a 3D mesh in $(u, v, 2\theta)$ should be acquired. This would, however, be too time-consuming, and with an order of magnitude better resolution along u it is acceptable to neglect v and sample a $(u, 2\theta)$ grid. In a similar manner as described above for the orientation distributions the local distribution is fitted by a Gaussian to obtain a local strain measurement for

each voxel.

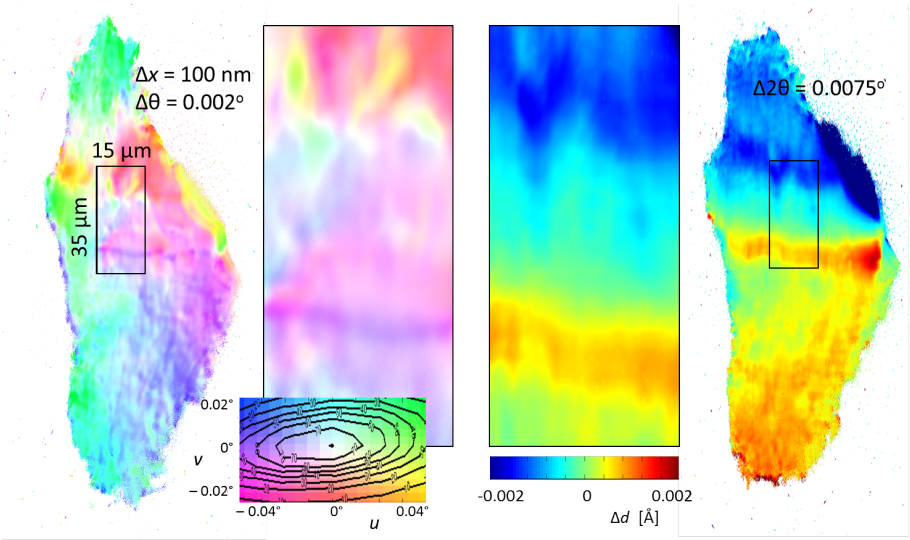

Figure 45: **Mosaicity and strain** Strain and mosaicity maps as obtained by Gaussian fits for a recrystallizing grain of cross-sectional area $150 \times 70\mu\text{m}^2$. A good qualitative correspondence between the strain and mosaicity maps is observed. Note that the strain map has not been corrected for the geometrical gradient described in Chapter 3.

An example of such a map is shown in Figure 45 for a larger grain of cross-sectional area $150 \times 70\mu\text{m}^2$ together with the mosaicity map obtained for the same layer. The voxel-size was $70 \times 280 \times 250\text{nm}^3$ and the step-sizes were $\Delta\theta = 0.002°$ and $\Delta 2\theta = 0.0075°$. A good quantitative correspondence between the mosaicity and strain maps are observed. For example, a horizontal line and several distinct features are observed in both maps. Of special interest is the point where the central line meets the exterior boundary in the right side. This point seems to possess some of the largest orientation and strain differences in the whole of the grain layer. The insets show close-ups of the boxed regions in the two maps. The central part of the grain gave rise to a larger scattered intensity than the top and bottom.

4.2 Ultra low angle boundary network

The mosaicity and strain maps of a single layer of an embedded recrystallizing grain revealed that the grains possess internal variations in lattice orientation

and strain consistent with the uniform domains separated by distinct boundaries. The difference in orientation between the domains is 0.1° or less. Direct evidence of the presence of a network of ultra low angle boundaries within recrystallizing grains is presented in this section and the relation between the intragranular structure and the external grain boundary is investigated. Furthermore, it is demonstrated how these ultra low angle boundaries can be characterised in terms of orientation differences and orientation spread. Furthermore, the evolution of the intragranular structures during annealing is investigated statistically.

4.2.1 Orientation differences

To investigate further the observed internal orientation variations the orientation difference is mapped, see Figure 46a. The orientation difference is given by $\Delta\phi = \sqrt{(\Delta u)^2 + (\Delta_v)^2}$ as is averaged over nearest neighbour voxels. The map reveals well-defined internal boundaries of very low orientation difference, see Figure 46b. The profile reveals that these internal boundaries are as narrow as a single voxel.

The studied layer is subdivided into several regions $5 - 7\mu$m in size with internal orientation variations within the region of $< 0.03°$ and $\Delta\phi$ on the order of 0.05° (0.03-0.1°) between them. On even more detailed inspection, these regions are found to be further subdivided into $2 - 3\mu$m sized domains of internal orientation variations below the resolution of the current experiment and $\Delta\phi \leq 0.02°$ between them.

This intragranular boundary network is a new observation which indicates that the remaining few dislocations inside a recrystallizing grain are not randomly distributed, but well-organized in a network of ultra-low angle boundaries of typical orientation difference $\Delta\phi \approx 0.05°$. This is equivalent to a dislocation spacing of $D = 300$ nm, on the order of the voxel size. Thus the dislocation density of the recrystallizing grain is estimated to be $10^{11}\mathrm{m}^{-1}$. This is equivalent to a stress of less than 2 MPa, which is insignificant compared to the flow stress of Al.

Furthermore, it is observed that the shape of the external grain boundary is correlated to the intragranular network. In Figure 46a arrows indicate where retrusions in the external boundary coincide with points where the internal boundaries meet the external boundary. This finding supplements the discussion

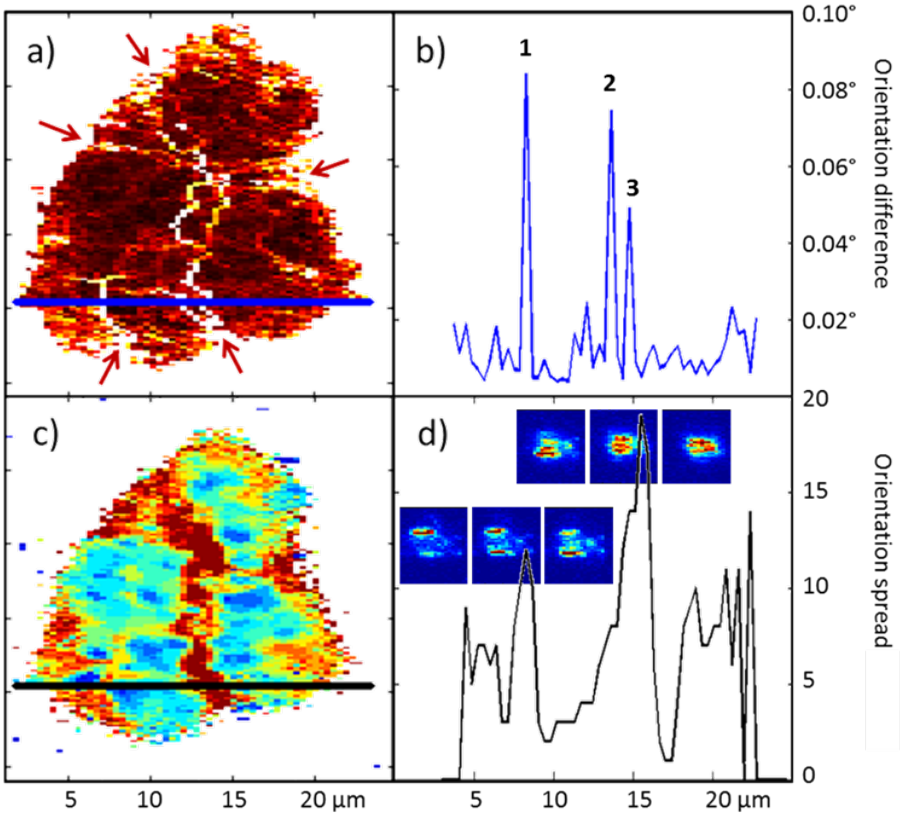

Figure 46: **Characteristics of intragranular boundaries** a) Orientation difference reveals a network of ultra low angle boundaries within the recrystallizing grain. Arrows indicate points where the internal boundary network correlates with the external shpe of the grain boundary. b) Profile along the blue line in a). The orientation difference across the internal boundaries are 0.1° or less. c) Orientation spread. The internal boundaries are associated with an increased orientation spread. d) Profile along the black line in c). The inset orientation distributions have v horizontally and u vertically. From [**Paper1**]

on how the migrating boundary of a recrystallizing grain forms protrusions and retrusions according to the local morphology of the surrounding deformed material, see previous chapters.

4.2.2 Orientation spread

To exploit the multidimensional nature of the DFXRM-data the orientation distribution associated with each voxel may be characterized in terms of the

orientation spread. The spread is defined here as the number of pixels in the orientation distribution with more than half the full-width-half-max (FWHM) intensity and is chosen like this yield small numbers for sharp peaks even if several distinct peaks are present in the orientation distribution, whereas the Gaussian variance (first moment) is large in that case. Thus the orientation spread measures the total spread of the individual peaks from individual voxels rather than the total orientation spread within the voxel.

From Figure 46c it is evident that the intragranular ultra-low angle boundaries are associated with an increase in the orientation spread. The internal boundaries are observed to have different properties, with some as narrow as a single voxel and others several microns wide. This is demonstrated in Figure 46b and 46d where cross-sections of the orientation difference and spread are shown along the lines indicated in the corresponding maps. The intragranular boundary marked by 1 is sharp, indicating a well-ordered structure, whereas the boundaries 2-3 seems to be broader and less organized.

The inset in Figure 46d shows the local orientation distribution taken at both sides of and directly at the boundary. The boundary 1 separates two regions of distinct orientation as indicated by the two distinct peaks in the local orientation distributions and even at the boundary the two orientations are independently identifiable, whereas the different peaks in the orientation distributions at the boundaries 2-3 are less distinct.

4.2.3 3D Mapping

To obtain maps in three dimensions, data is collected for consecutive layers and the resulting maps are stacked. In Figure 47 maps of seven layers with a vertical spacing between layers of 300 nm are shown. The intragranular structures described above are easily identifiable through the layers both in terms of mosaicity, orientation differences, and orientation spread. This confirms, that the observed ultra low angle boundaries form a 3D network inside the recrystallizing grain.

4.2.4 Annealing

To investigate the evolution of this intragranular network a volume of a grain was mapped before and after annealing. The mosaicity of a layer in the $25 \times 50 \mu m^2$ grain reveals a similar intragranular structure in this grain as described above,

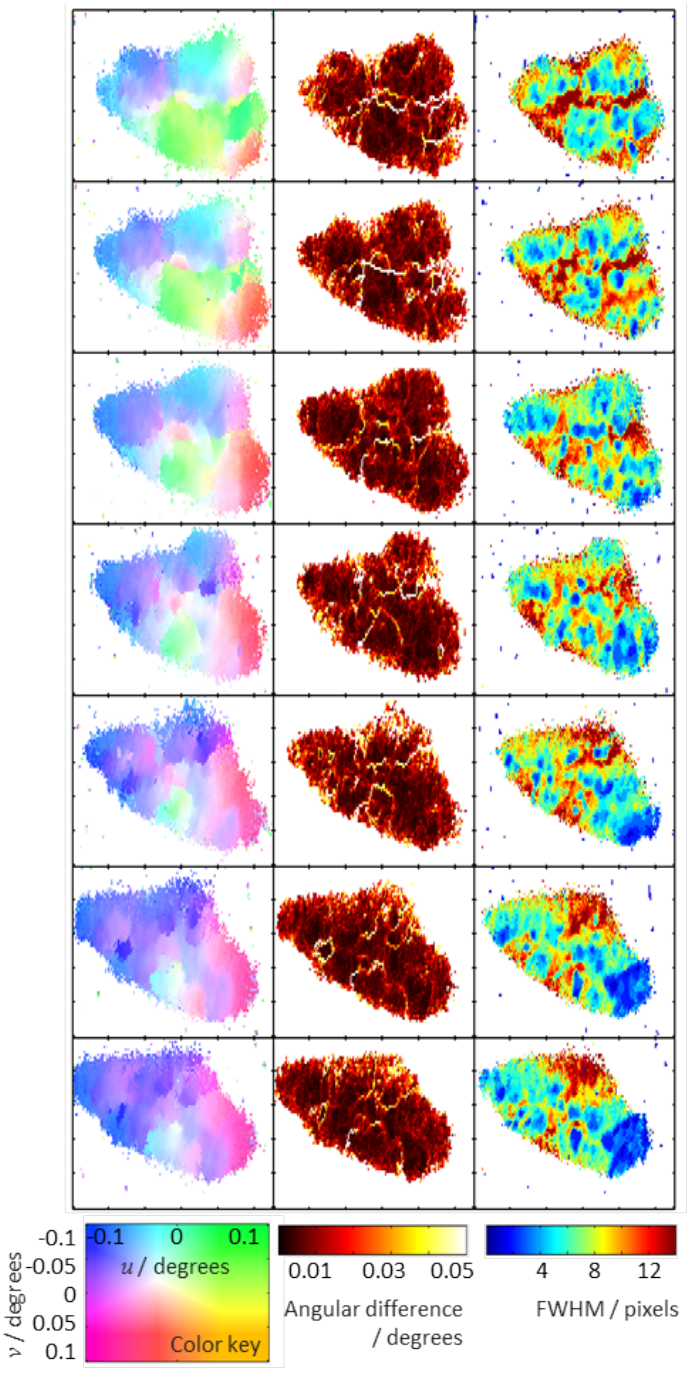

Figure 47: **Maps of 7 consecutive layers** The mosaicity, orientation difference between neighbouring voxels, and the local orientation spread are shown for seven consecutive layers with a layer spacing of 300 nm. The intragranular structure is consistent through the layers. From [**Paper1**].

see Figure 48. A volume of the grain was mapped covering 21 layers in 300 nm steps before the sample was heated to 325°C for 15 minutes, and a volume was mapped afterwards. This procedure was repeated another two times, each with annealing for 10 minutes at 325°C.

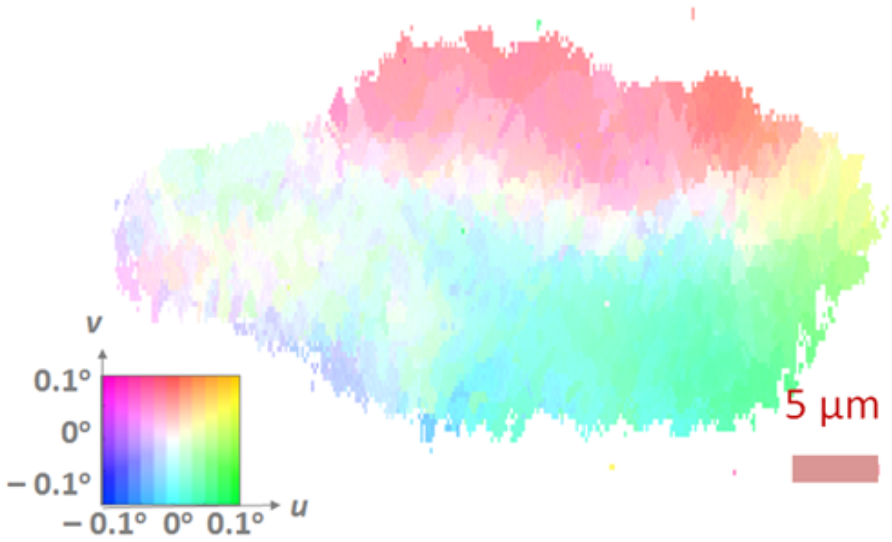

Figure 48: **Mosaicity map of grain used for annealing studies** The grain has a cross-sectional size of $25 \times 50 \mu m^2$ and an internal structure similar to the other recrystallizing grains.

The integrated orientation distribution over the whole volume mapped is shown in Figure 49. The width of this distribution provides an indication of the internal disorder within the grain. During the annealing steps the FWHM of the distribution decreased from 0.1° to 0.05°. This indicates that the structure cleaned up during further annealing.

As it turned out to be difficult to identify the exact same volume in the recrystallizing grain, it was not possible to produce difference maps for analysis. Instead, the structural properties of the mapped volumes were analysed statistically. For each of the annealing steps the internal structure of the mapped volume was quantified in terms of the distributions of voxel intensities, nearest neighbour orientation difference, and local orientation spread. The distribution for each layer was determined and the standard deviation between the layers in the same volume was calculated. The results are shown in Figure 50 with errorbars indicating the standard deviation.

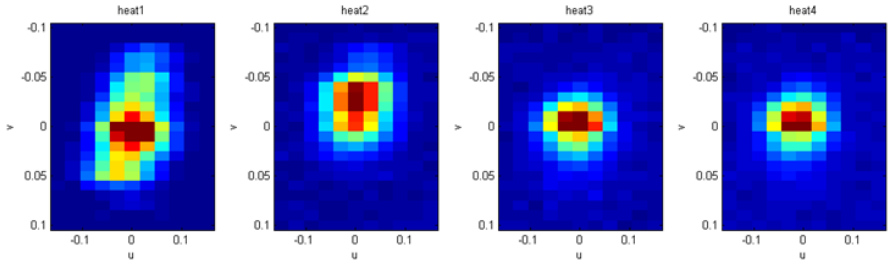

Figure 49: **Integrated orientation distributions** The width of the integrated orientation distribution decreased as a during annealing.

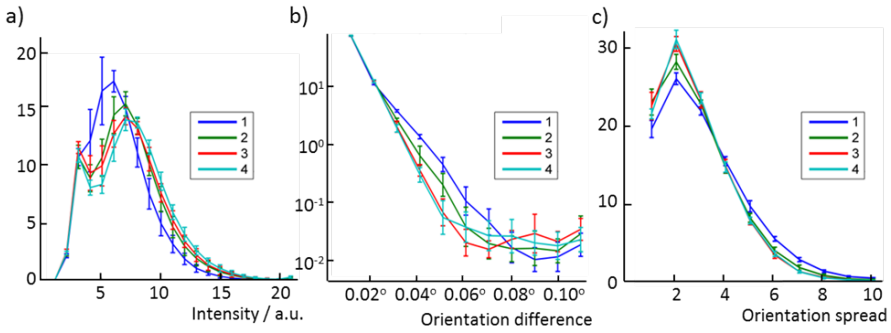

Figure 50: **Annealing of the intragranular network** Statistical study of the evolution of the intragranular structure in a recrystallizing grain during during further annealing. a) The distribution of voxel-wise intensities shift towards higher intensities. b) The distribution of orientation differences between neighbouring voxels decrease. c) The distribution of local orientation spread decreases. This suggests that the internal structure cleans up during further annealing. From [**Paper1**].

The intensity of a diffraction peak originating from a particular voxel is proportional to the diffracting volume, and thus provide a crude measure of the degree of crystallinity within the voxel. As the distribution of intensities was observed to shift towards higher intensities during the four annealing steps, this again indicate that the structure became more well-ordered. Likewise, the distribution of local orientation spread was observed to decrease during the annealing.

The number of voxels with small, non-zero orientation differences decreased while for voxels of larger orientation difference above 0.08° a slight increase in numbers was observed. This is consistent with the structure becoming more

ordered and indicates that the intragranular boundary network organizes further. Some of the few remaining dislocations in the interior of the recrystallizing grain may have moved to the internal or external boundaries or have annihilated during the annealing.

The difference between the distributions for the third and fourth maps are negligible, suggesting that no further cleanup of the intragranular structure takes place upon further heat treatment at that particular temperature.

4.3 Towards dislocation densities

The DFXRM data analysis may be carried one step further on the basis of the interpretation of $(u, v, \epsilon) = (-\beta_{31}, \beta_{32}, \beta_{33})$ as components of the distortion tensor described in Chapter 2. By this method dislocation densities may be extracted from DFXRM-measurements and the internal structures may be (partly) resolved in terms of the different types of dislocations that make up the structures.

In this section the method is demonstrated experimentally for a thinfilm sample of $BiFeO_3$ and the first steps towards applying the method to more complicated samples such as recrystallizing grains in 3D are taken. For the present work the analysis was limited by the unavailability of z-gradients due to difficulties in aligning consecutive layers in the 3D map. The appearance of the available β-derivatives is presented for recrystallizing grains. The results below are preliminary but promising.

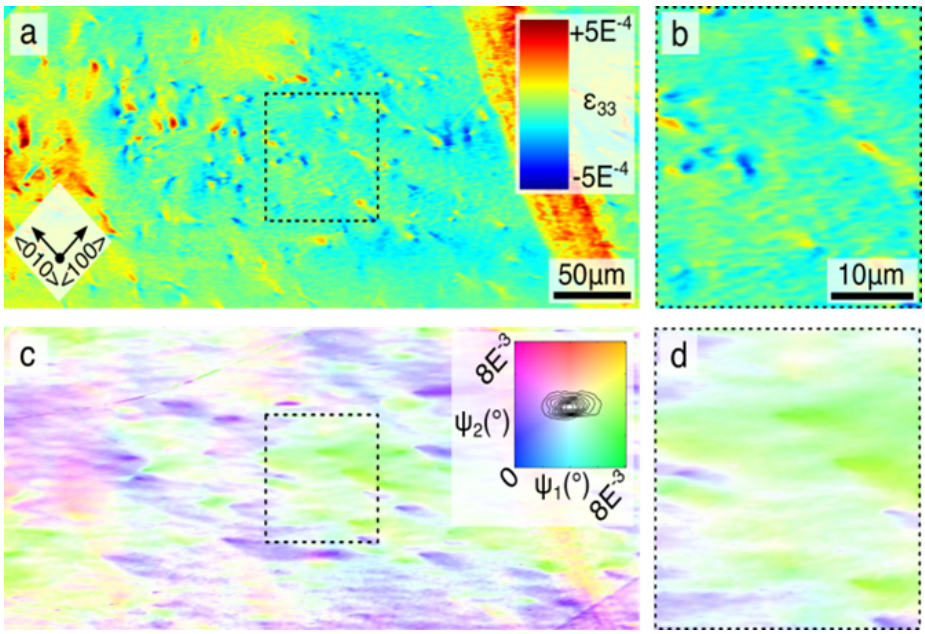

Figure 51: **Mosaicity and strain maps of $BiFeO_3$ thinfilm.** a) Strain map. c) Mosaicity. b), d) Zoom to the indicated square. The mosaicity and strain maps reveal distinct features, but the underlying structure is not apparent. Courtesy of H.Simons.

4.3.1 A first demonstration

The expressions for the β-components which were derived in Chapter 2 are given in the coordinate system of the pure edge and screw dislocations, respectively. In a real sample dislocations of a variety of different types and orientations may be present and the coordinate system of a dislocation is rarely coincident with the coordinate system of the experiment. Since data is collected in the frame of the experiment, the dislocation fields must be projected into the experimental frame. The situation is further complicated by the fact that the scattering vector is tilted to an angle θ around x with respect to the normal direction of the plane illuminated by the line-beam in the DFXRM setup.

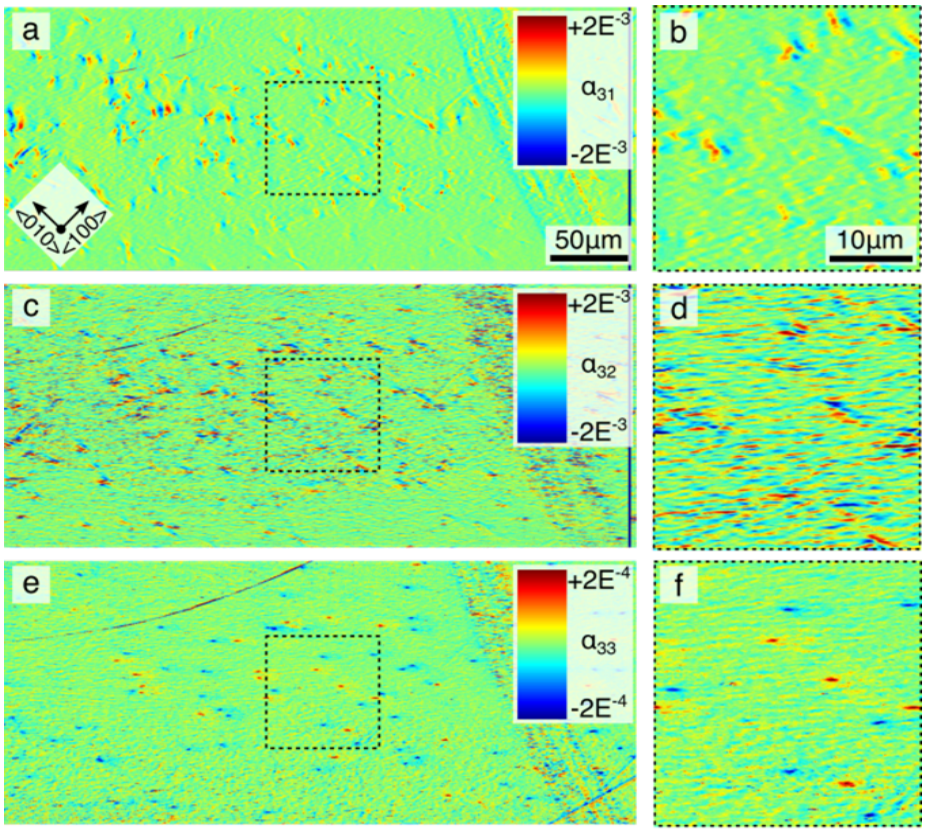

Figure 52: **Derived dislocation densities** The three components α_{31}, α_{32}, andα_{33} available from DFXRM-measurements are shown in a), c), and e), respectively, for a $BiFeO_3$ thin film. b), d), and f) shown the zoomed images as indicated by the squares. The observed dislocation densities are consistent with the presence of single dislocations. [**Paper7**]

For purposes of demonstration the method was applied to DFXRM-data acquired for an epitaxially grown thinfilm of the ferroelectric $BiFeO_3$ which is known to possess screw dislocations along the perpendicular direction. The data presented here will be published as part of a study of $BiFeO_3$ thin films and their functionality. [**Paper7**]

The mosaicity and strain maps obtained for a scattering vector parallel to the plane normal with full-field illumination are shown in Figure 51. There seems to be distinct points of deviating orientation and strain, however the structure responsible for the deviations are not directly identifiable.

With all z-derivatives assumed to be zero the available α-components are derived in Figure 52. Distinct spots of equivalent size and intensity and of both positive and negative dislocation density are easily seen in α_{33}. The observed dislocation densities are consistent with screw-dislocations of both signs as expected, and in the analysis they are interpreted as such. Furthermore, some dislocations are connected two and two of opposite sign by a line in α_{32} and/or α_{31}. This observation indicate that dislocation loops are present within the thin-film and thus the z-derivatives are in fact non-zero. Nevertheless, the example demonstrates the applicability of the analysis.

For the $BiFeO_3$ thinfilm it is demonstrated how dislocation densities may be derived from DFXRM-data and interpreted in terms of certain types of dislocations. For the internal structure of recrystallizing grains of aluminium this is not as straight forward since the many different types of dislocations are expected to be present and due to the *fcc* structure of aluminimum their orientations with respect to the (002) scattering vector are not parallel. Nevertheless, as shown below the analysis yield interesting and useful information about the dislocations structures even for such a sample.

4.3.2 Directional derivatives

Directional derivatives $\partial_i \beta_{3j}$ with respect to the horizontal x-direction and the vertical y-direction are shown in Figure 53 for the Gaussian-fitted orientation of the small grain presented previously. Streaks in the horizontal gradients are observed together with several other interesting features. In particular the horizontal line in du/dy that connects retrusions in the exterior boundary, which is identified as part of the ultra low angle boundary network discussed above. In general, retrusions in the exterior boundary are observed to be associated

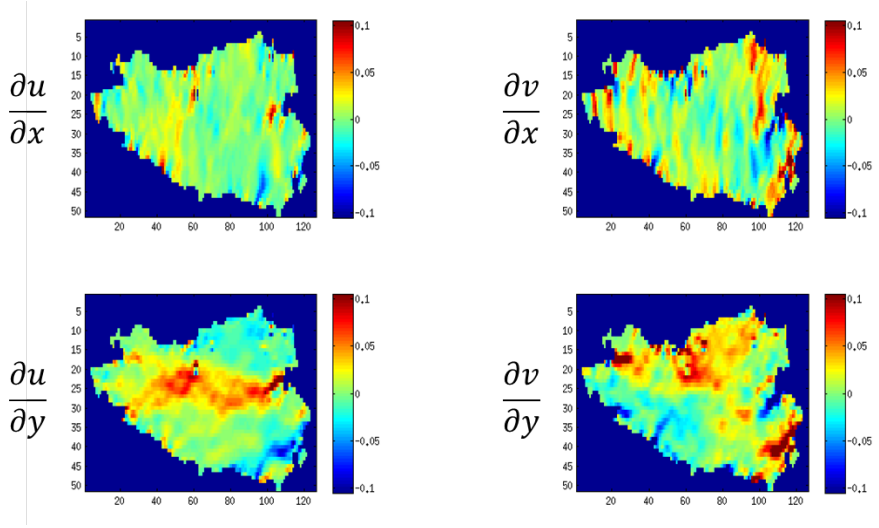

Figure 53: **Directional derivatives for a small grain** The four available derivatives provides complementary information about the intragranular structure

with orientation gradients that deviate from zero as expected from the previous analysis of the intragranular network. The images in Figure 53 reveal localized regions and lines of non-zero gradients. Most importantly, the four different gradients provide complementary information on the intragranular structure, and it is concluded that the structures observed in this analysis agree well with the previous observations.

The derivatives for a larger grain are shown in Figure 54. A distinct shape is observed for du/dy where sharp double lines of opposite sign encircles the central part of the grain. Within this region the diffracted intensity was larger, and the features in the maps are sharper here. In the rest of the grain an underlying pattern is observed for all four derivatives. In du/dx curly lines of alternating sign are following the shape from top to bottom. Likewise in du/dy, but here the lines are roughly parallel to the flat boundary on the top right. The resolution in v is not as good as in u , however, on close inspection there seems to be lines here as well, with directions related to the orientation of the different grain boundaries. Also for this larger grain the four maps are complementary and have few features in common but the observed shapes match each other.

The size and shape of the observed pattern is similar to the subgrain structure of the sample as observe with EBSD (see Chapter 1) and it is speculated

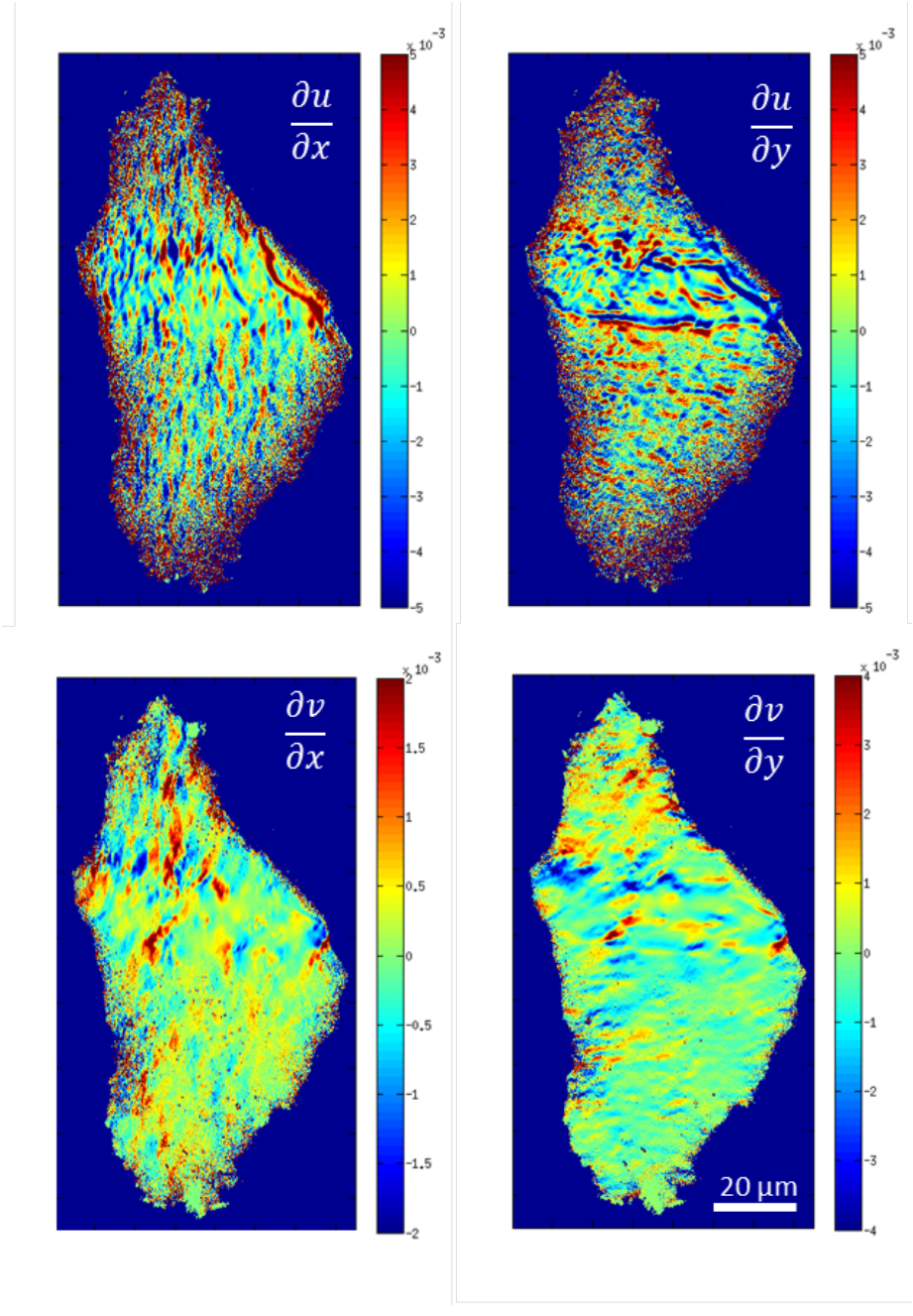

Figure 54: **Directional derivatives for large grain** The four maps reveal structures and patterns representing the intragranular structure.

that this patterned structure is a few remaining dislocations from the deformed structure that the grain has grown from. The different orientations of the pattern in the four derivatives suggest that it is indeed different types of dislocations that are visible in the different derivative plots.

Furthermore, the qualitatively different ultra low angle boundary structure in the encircles region, where lines are more intense and the pattern is not as obvious, suggest that recrystallization for this sample is a two-stage proces: First, the boundary of the recrystallizing grain migrates into the deformed structure and leaves behind an almost defect-free lattice with the few remaining dislocation still in the same position as before the boundary migration. Then, under further annealing the ultra low angle boundary network cleans up and forgets the pattern from the deformed structure.

These findings emphasises the importance of knowing the history of a specimen.

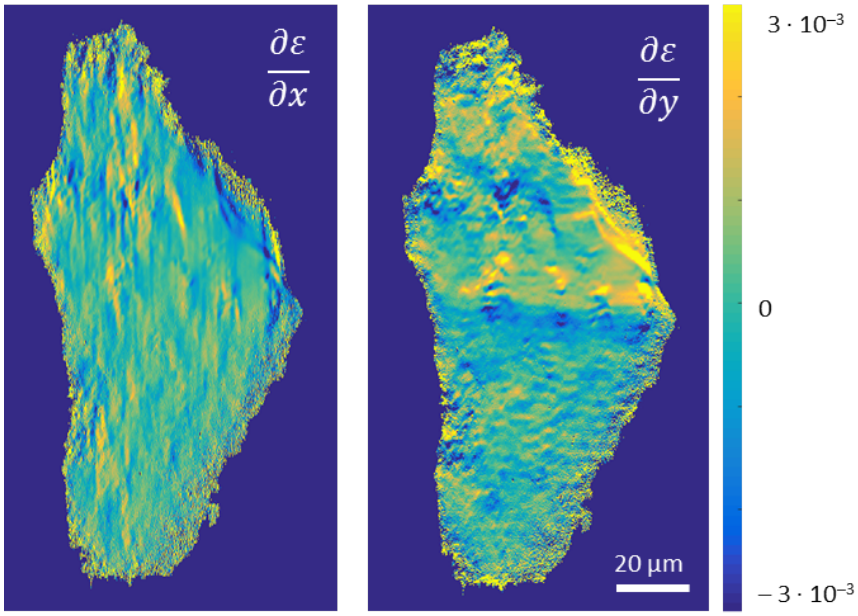

Figure 55: **Directional derivatives of strain** These maps are complementary to the derivatives of u and v

The strain gradients are given in Figure **??**. An apparent repetition of the features could indicate an artificial shift in the data series. However, the central region is also visible here and the bottom line of this structure corresponds to a change of sign.

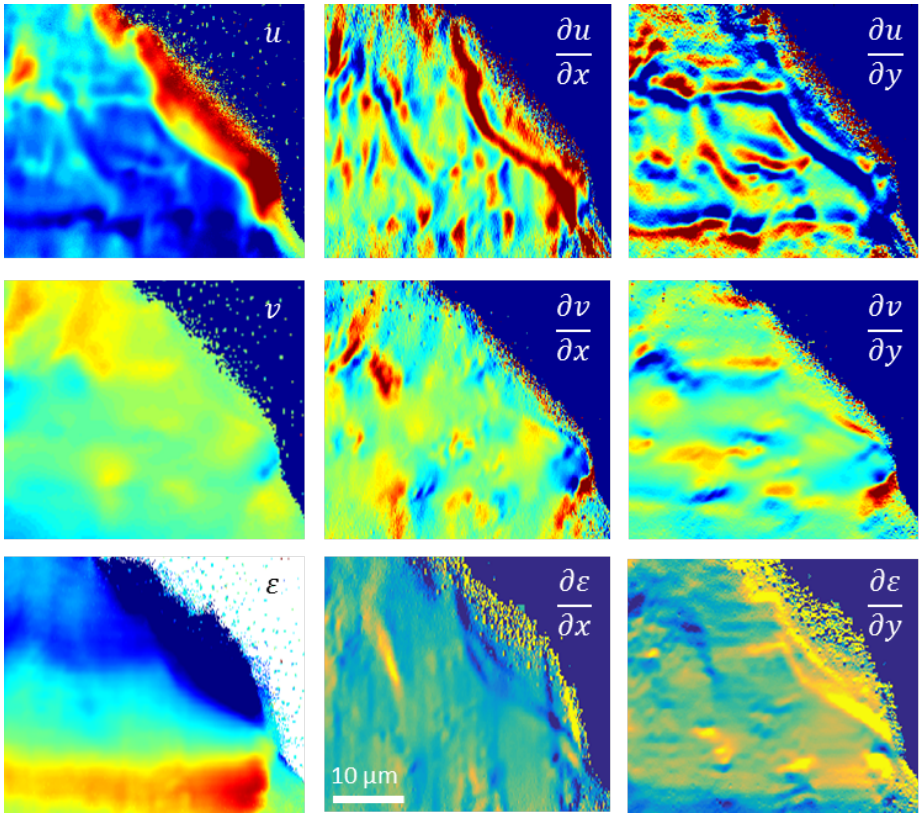

Figure 56: **Zoom on point of interest.** An overview of currently available information.

The point on the right where the internal lines meet the external grain boundary just below the flat boundary segment on the upper right side is connects the external grain boundary with several internal lines. Therefore a zoom on this part of the recrystallizing grain is presented in Figure 56 for all three parameters u, v, and ϵ and their derivatives.

The map in u shows an edge-like boundary which resembles the distortion component β_{yx} shown in Chapter 2 and many interesting features in the maps are observed. However, to progress with the analysis in terms of specific dislocation densities, the 21 layers mapped must be reliably stacked to extract z-derivatives, which as of yet has not been achieved.

4.3.3 Radial gradients

Radial gradient of an image provides a measure of where the image changes the most. Thus the orientational changes may be visualized in an easy manner by calculating the radial gradient with respect to the two perpendicular tilt directions u and v. The radial gradient for the Gaussian fitted orientations in the small recrystallizing grain is shown in Figure 57. The observed structures are remarkable similar to the structures found in the orientation spread in Figure 46 above and the internal boundary network is clearly visible.

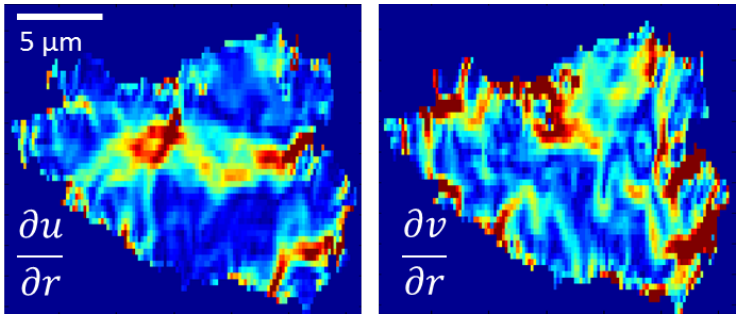

Figure 57: **Radial gradients for a layer of small recrystallizing grain** The radial gradients with respect to the orientations u and v assigned by Gaussian center-of-mass fits are shown. The observed features resemble those determined from the analysis presented above.

Likewise, for the large grain analysed in this section, the radial gradients of u, v, and ϵ reproduces the investigated features and gives an idea of the appearance and length-scale of the internal structure, see Figure 58. Therefore, although it is not quantitatively reliable due to the elongated shape of the

voxels of DFXRM maps, the radial gradient provides an easy overview of the internal structure even for orientations assigned by Gaussian center-of-mass fits to the full orientation distribution. This could be a applied at the beamline as a useful tool for visualising internal structures while an experiment is ongoing, for example to determine if the internal structure has evolved during an annealing or deformation step.

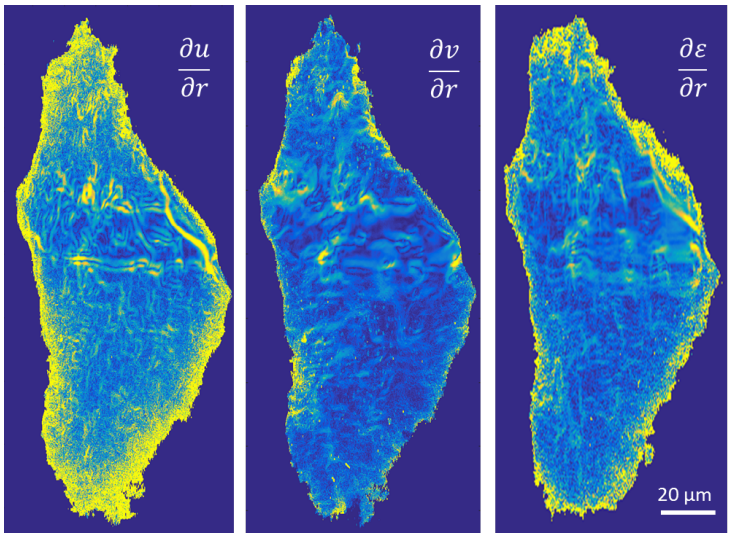

Figure 58: **Radial gradients for a larger recrystallizing grain** The radial gradients with respect to the orientations u and v as well as axial strain ϵ assigned by Gaussian center-of-mass fits are shown. The observed features resemble those determined from the analysis presented above.

In conclusion, it has been demonstrated how internal dislocation structures in almost defect-free grains can be visualised by means of DFXRM and directional derivatives of Gaussian moment fits.

5 Recovery kinetics of individual subgrains

Recovery is a complex process and there may be several mechanisms in play simultaneously. The local dislocation dynamics and subgrain growth kinetics strongly depend on the local texture and strain. Therefore, to understand the mechanisms of recovery it is necessary to be able to characterize the bulk microstructure in 3D and quantify its evolution both locally and on average.

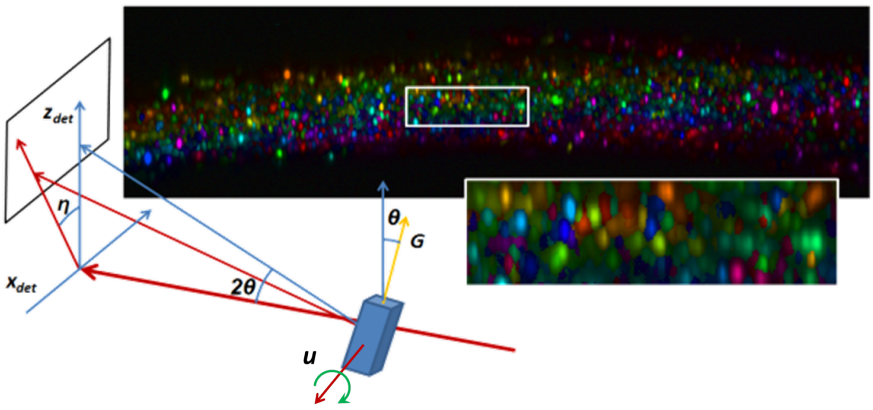

Figure 59: **Experimental setup for subgrain studies** Diffraction from subgrains gives rise to spots on a high resolution detector within a band in scattering angle 2θ corresponding to a section $\Delta\eta$ of the (111) Debye-Scherrer ring. Exposures were made as function of tilt angle u. The brightness of each pixel represents the maximum intensity for that pixel and the color represents the orientation in u for which the intensity was maximum. Shown as inserts are the full image as well as a zoom on the region marked by the white box.

As described in Chapter 2 it has been demonstrated that diffraction spots from several hundred bulk recrystallizing grains could be identified and tracked in time during annealing at constant temperature by means of 3DXRD. From these measurements changes in volume were inferred and by analysing growth curves at two different temperatures individual growth rates and activation energies for close to 1000 grains were obtained (references are given in Chapter 2). It was observed that each recrystallizing grain followed its own growth kinetics with large variations in nucleation time, growth rate, and activation energy.

Being near perfect crystals, subgrain structures give rise to (low intensity) diffraction spots in their own right. However, carrying out the above type of

3DXRD-measurements on the subgrain structures is difficult due to the vast number of illuminated subgrains and corresponding vast number of overlapping diffraction spots. The maximum number of identifiable diffracting units in a 3DXRD experiment is a few thousand, which limits the sample size for a recovery experiment to a thin plate less than 100 μm thick even for a micron-sized point-beam. The feasibility of tracking individual subgrains during annealing has been demonstrated (see Chapter 2), however, the experiments are limited by the resolution of the detector.

In this Chapter a novel experimental approach for tracking thousands of individual bulk subgrains during annealing is presented, which can be directly combined with other x-ray methods at existing setups. The 3DXRD setup was altered to allow tracking of subgrains in mm thick specimens at the expense of only characterizing a section of orientation space. In this way several thousand individual diffraction spots were identified and the characteristics interpreted in terms of subgrain size and internal disorder. Furthermore, each subgrain was tracked during annealing at a constant heating rate and the kinetics was quantified in terms of growth rate, and changes to strain and orientation, leading to a statistical investigation of the underlying mechanisms for recovery at low temperatures.

An introduction to the method and data acquisition is given in the first section as this new method is exploited to study the basic mechanisms related to low temperature recovery in deformed aluminium AA1050. Then follows a presentation of results and a discussion of comparison with current models for recovery. The method and results presented here will also be found in [**Paper3**].

5.1 Experimental technique

A description of the experimental setup and data acquisition strategies is given in this section. Like the DFXRM-instrument, this experiment is based on the 3DXRD setup, the main differences from 3DXRD being that the detector is placed at a position were only a section of a single Debye-Scherrer ring is acquired and the sample is only rotated through a few degrees instead of a full 180° or 360° rotation. A sketch of the geometry is shown in Figure 59

5.1.1 Experimental setup

The experiment was performed at the microscopy setup at the DFXRM beamline ID06 at ESRF (see description in Chapter 3). Using a Si-111 Bragg-Bragg monochromator, a monochromatic x-ray beam of energy of 16 keV (λ =0.77 Å) was focused and defined by slits to provide a uniform boxbeam on the sample of size $100 \times 100 \mu m^2$.

The sample was placed immediately after the slits at a distance of 55m from the source on a goniometer that allowed high precision control over tilts and translations of the sample. For the present experiment we used only the 'rocking angle', the rotation u around the horizontal axis perpendicular to the beam direction.

The sample was mounted on a sample-stage with multiple high precision rotations and translations and illuminated by a box-shaped monochromatic x-ray beam. The diffracted signals from crystalline domains were captured by a high resolution image detector, if the lattice orientation of the domains matched the scattering geometry.

In classical 3DXRD all diffracted signals within the first 3-5 Debye-Scherrer rings are captured on a diffraction detector with a resolution on the order of 100 mm. In this experiment the detector is replaced by a high resolution image detector, a tapercoupled FReLon detector with an effective pixel size of 0.622 μm corresponding in the vertical direction to a resolution of $\Delta 2\theta = 0.0014°$ and in the horizontal direction to $\Delta\eta = 0.0047°$. The spatial resolution was given by the effective pixel-size. This detector was placed at a distance of 22 mm horizontally from the sample position and elevated with respect to the direct beam to collect (111)-reflections at $2\theta = 19.1°$. At this position the detector covered a section of the Debye-Scherrer ring equivalent to $\Delta\eta = 9.5°$, see Figure 59.

The sample was an aluminium AA1050 specimen as previously described, cold-rolled to a 50% reduction in thickness. Using electrical discharge machining, a rod-shaped sample of cross-sectional area $300 \times 300 \mu m^2$ perpendicular to the rolling direction (RD) and 1 mm long was cut from the specimen and annealed for 50 minutes at 325°C. This treatment resulted in almost 50% recrystallization. Thus the sample structure consisted partly of larger recrystallizing grains and partly of deformed grains recovered to a subgrain structure. At 25°C the lattice spacing is 4.045 Å and the heat expansion coefficient is $23.1 \cdot 10^{-6} K^{-1}$.

The sample was mounted on a Cu-stick in the x-ray setup with RD parallel to the scattering vector $\vec{G}$, to be able to study crystalline domains with a (111)-direction parallel to RD to within a few degrees.

The sample was heated continuously with a hot air blower from 25° to 225° at a constant heating rate of 0.6°C/min, except for the first 50°C for which the heating rate was 1.2°C/min. The duration of the full experiment was 5 hours. The actual sample temperature was determined with accuracy better than 10°C from the vertical shift of the total 2θ-ring. Movement and rotation of the sample during the annealing due e.g. to expansion of the Cu-stick was accounted for in the data analysis software. However, the actual shift in volume implied that the number of traceable subgrains was significantly reduced.

While heating, data series were collected in situ for a total of 117 temperatures in the interval, each consisting of 40 consecutive images covering a tilt of $\pm 1°$ in u in steps of 0.05°. Each image was acquired continuously while the sample was rotated through the 0.05° step and showed numerous distinct diffraction spots in the mapped 9.5° section of the 2θ-ring. Combining all 40 images in a data series reveals several thousand diffraction spots. In Figure 59 an example of such a combined data set is shown with colors indication orientation in u and brightness indicating diffracted intensity at that point.

All diffraction spots lie within the same $9.5° \times 2°$ section of the diffraction sphere. Together with a visual inspection of the raw data (see Figure 59 and 60) this suggests that all the identified subgrains lie in the same deformed grain (expect for maybe the presence of a few nuclei from other sites in the sample). Not the full extent of the deformed grain was mapped. Since no diffuse background diffraction from highly disordered structures was observed around the diffraction spots, the deformed grain had recovered to a subgrain structure and all boundaries were well-ordered low angle boundaries. The deformed grain as well as the subgrains had (111) parallel to RD and since subgrains of this orientation are not expected to grow as much as subgrains of cube texture, the kinetics were expected to be slow.

5.1.2 Identification and tracking of subgrain diffraction spots

The data was corrected for shifts due to heat expansion and translation of the sample by the aid of imageregistration in Matlab. The corrections were found to be accurate to within less than one pixel and all shifts shown in the analysis

corresponds the deviations of individual spots from the overall shift. Individual diffraction spots were identified in an automated manner, see Figure 60. The characteristics of each spot were determined and the spots were matched through the temperature series.

In this manner individual diffraction spots from several thousand subgrains were identified for each temperature, and 498 individual spots could be traced through the series from 80°C to 225°C. For each of these the central position in rocking angle u and central position on the detector (u, x_d, z_d) was determined together with the integrated intensity, I_s, and the extend of the spot or peak area, A.

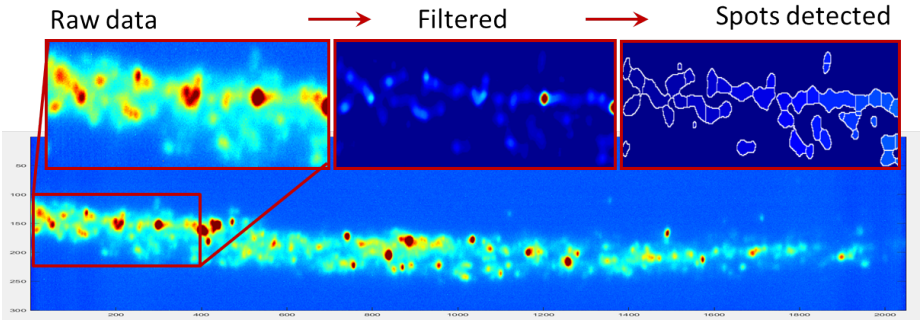

Figure 60: **Data analysis** Using Matlab, the relevant features of the raw images are extracted by applying a circular filter of appropriate size and the individual diffraction spots are identified by peak detection utilizing a watershed approach. The measured intensity in the identified spots as well as the position and extens of the spots were determined and the spots were matched through the temperature series. The illustration is shown in 2D, however the analysis is carried out on the 3D data stacks in u.

The actual sample temperature at each data series was calculated from the total shift in z_d with respect to the data series at 25°C. A shift of 1 pixel corresponded to a change in temperature of $\Delta T = 3.25$°C. The uncertainty in the derived temperature was estimated to be less than 10°C and smaller for lower temperatures. The uncertainty stemmed solely from the calculation since the temperature dependence of the heat expansion coefficient was neglected and it was assumed that even the maximum shift in 2θ was small.

The position in u of a diffraction spot was a direct measure of the tilt of the (111)-lattice plane normal of the diffracting subgrain with respect to rotation

around a horizontal axis perpendicular to the beam direction, see Figure 59. After correcting for the changes due to temperature the vertical position of each diffraction spot z_d on the detector was a convolution of the position of the diffracting subgrain within the sample and its average axial strain. The horizontal position, x_d, was given by both the position of the subgrain and an orthogonal tilt of the lattice plane normal. Likewise, the shape of a diffraction spot is a projection of the subgrain shape blurred by a factor due to the mosaic spread of an imperfect lattice and deviations in axial strain. For the present experiment it is not possible to deconvolute this information, however tracking the changes in detector position, spot size, and intensity of each spot during annealing revealed valuable details of the subgrain kinetics, see below.

5.1.3 Subgrain volume, equivalent radius and growth rate

Integrating over u, the measured spot intensity for each subgrain I_s was converted to an associated subgrain volume V_s in accordance with the following relation [ref Gundlach]:

$$V_s = V_i \frac{I_s}{I} \frac{m \Delta\eta \Delta u}{360^\circ \cdot 180^\circ} \tag{113}$$

I is the total integrated intensity within the measured tilt ranges of $\Delta\eta$ and Δu, and $m = 8$ is the multiplicity of (111)-reflections. Here it is assumed that the sample has a random texture. Dividing by the total intensity also corrects any overall temperature dependence of the diffracted signals. The illuminated sample volume was $V_i \approx 100 \times 100 \times 300 \mu\text{m}^3$. The equivalent subgrain radius R_{eq} was calculated from the geometrical relation $V_s = \frac{4}{3}\pi R_{eq}^3$.

The growth rate for each subgrain was calculated as the derivative of the subgrain volume with respect to temperature:

$$v_T = \frac{dV_s}{sT} \tag{114}$$

The growth curves $V_s(T)$ were smoothened before taking the gradient.

5.1.4 Internal disorder

The size of a diffraction spot is related to the shape and lattice disorder of diffracting crystallite. Only a few spots extended beyond a single orientation in u, indicating that the internal mosaic spread of the subgrains was less than the step size, 0.05°. Since measurements were performed in the near field regime the

peak shapes in (x_d, z_d) were a convolution of the projected shape of the subgrain and the strain and mosaic spread, and line profile theory cannot be applied (this method is restricted to the far field limit). However, the size of the identified diffraction spots gives an indirect measure of the internal disorder in the lattice giving rise to the peak if corrected for the extent of the lattice. Therefore a dimensionless disorder parameter, W, was defined as the ratio between the area in μm^2, A, of the spot on the detector and the calculated cross-sectional area in real space of the corresponding (spherical) subgrain:

$$W = \frac{A}{\pi R_{eq}^2} \tag{115}$$

There are several other contributions to the spot size than the shape of the diffracting subgrain and internal disorder, including instrumental- and size-broadening, thus the disorder parameter is a rather crude measure. Nevertheless, the evolution of W during annealing was found to provide a good indication of the subgrain dynamics, see below.

5.1.5 Rotation and strain

The actual axial strain given by the angle of diffraction and lattice orientation in η of individual subgrains could not be determined from the present experiment, since the position of the corresponding diffraction spot in (x_d, z_d) is a convolution of these parameters with the position of the subgrain within the sample. Likewise, the size of the diffraction spot contained information on the internal mosaicity and strain deviations convoluted with the shape of the diffracting subgrain, which could not be extracted.

However, during annealing the individual diffraction spots could shift slightly and since the subgrains were observed to grow or shrink only moderately, see below, the observed individual shifts could not be accounted for by spatial translation of the subgrain center-of-mass. Therefore, the observed horizontal shifts may be ascribed primarily to subgrain rotation and vertical shifts to changes in the axial strain, where a positive shift indicates a reduction in the lattice parameter and a negative shift indicates an increase with respect to the overall heat expansion. A horizontal shift of 1 pixel corresponded to a lattice rotation of $\Delta\eta = 0.0047^\circ$ and in the vertical direction a shift of 1 pixel downwards corresponded to a change of internal axial strain of $\Delta\varepsilon = 1.5 \cdot 10^{-4}$ relative to the overall thermal lattice expansion. Note, that the (111)-planes observed in

this study are slip-planes and thus their mutual separation and orientation are highly sensitive to the presence and motion of dislocations.

5.1.6 Correlations

To investigate the statistical probability of a correlation between two parameters, the Kendall τ-coefficient was calculated. This coefficient is given by the difference between the fraction of pairs of points with a positively sloping connection line and the fraction of pairs of points with a negatively sloping connecting line:

$$\tau = \frac{N_+ - N-}{N_+ + N_-} \tag{116}$$

If a direct correlation exists such that a larger value of the one parameter is always associated with a larger value of the other, $\tau = 1$. Likewise, $\tau = -1$ if a larger value of one is associated with a smaller value of the other and $\tau = 0$ if no correlation exists between the two parameters.

5.2 Tracking subgrains during annealing

In this section a statistical analysis is presented of the evolution during annealing of the several hundreds of subgrains that could be tracked trough the whole temperature range. The analysis starts from the calculation of overall size distributions and other statistical properties as a function of temperature combined with the examination of individual growth curves and evolution of disorder parameters and shifts. Then the individual growth curves are examined followed by an investigation of growth rates and the possible correlation to subgrain size.

5.2.1 Size distributions and disorder parameter

Several thousand subgrains were identified at each temperature step and out of these 498 were traceable through the whole temperature range. The statistical analysis of the obtained subgrain characteristics is summerized in Figure 61. The first column shows the evolution with temperature of the parameters for 10 randomly selected subgrains and the statistic for all subgrains are shown in the middle column, with the central line indicating the average and the surrounding lines indicating one and two standard deviations, respectively.

The mean equivalent radius (central line in Figure 61b) did not change much: it decreased slightly from 1.14 μm at 100°C to 1.08 μm at 160°C, remained

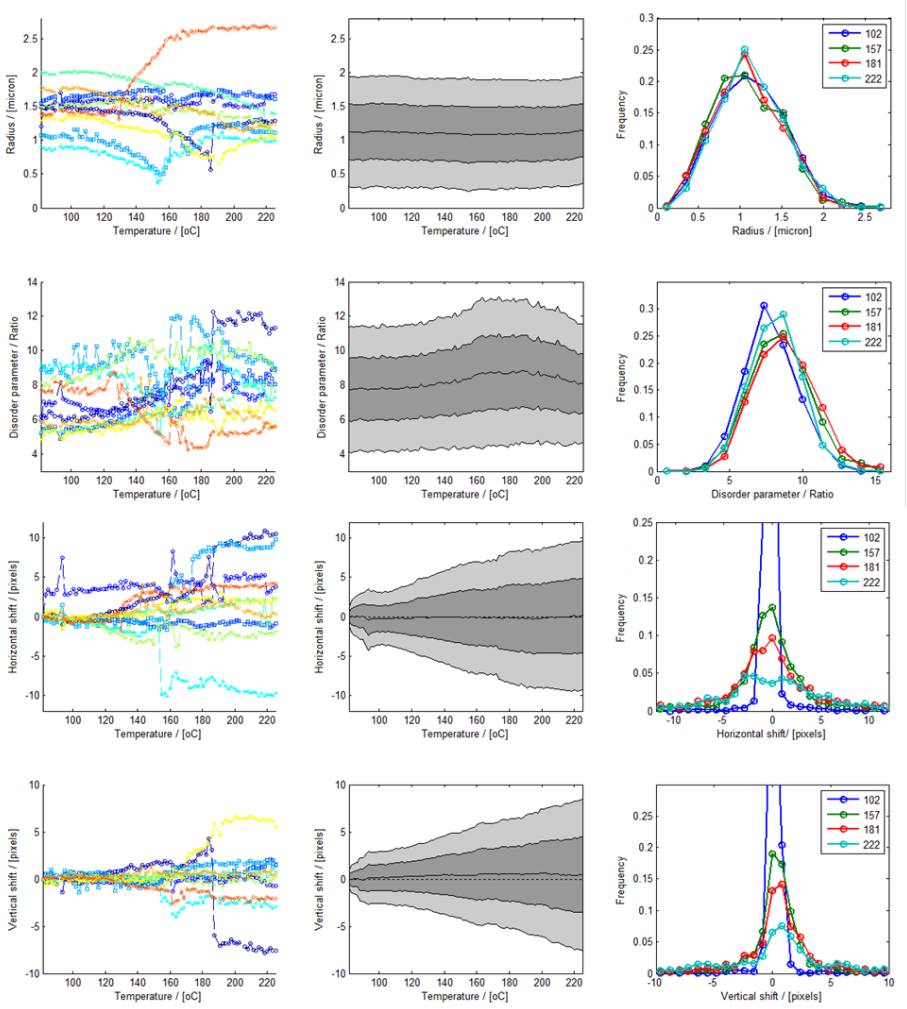

Figure 61: **Statistics and tracking of individual subgrains** Statistical analysis of four parameters for 498 individual subgrains. Equivalent radius, disorder parameter, and horizontal and vertical shifts of the diffraction spot. Left column: 10 randomly selected subgrains. Middle column: Mean in the middle and 1 and 2 standard deviations. Right column: Distributions for four temperatures. Each histogram is generated from data from 5 subsequent temperature steps to better the statistics.

constant until 190°C then increased to 1.15 μm at 220°C. The size distribution (Figure 61c) was narrow and resembled a lognormal distribution for all temperatures. The majority of the detected subgrains had equivalent radii within 0.5-2 μm with a detection limit of 0.2-0.3 μm, depending on the maximum intensity

of the diffraction spot. The normalized size distribution remained largely unaltered during the experiment. The initial decrease in equivalent radius and the broadening of the size distribution was most likely caused by the appearance of new subgrains of detectable size.

It should be noted that the absolute value of the equivalent radii (and volumes) rely on the assumption that the diffracted intensity of the sampled area is representative of the whole diffraction sphere. This is likely to be wrong since diffraction from a deformed grain is not evenly distributed on the sphere. However, the total scattered intensity from the deformed grain as well as its volume is not available. The effect of this uncertainty is a possible shift of the size distribution, but the shape of the distribution is independent of this problem. Furthermore, the calculated sizes are in good agreement with previous x-ray studies and electron microscopy measurements, see Chapters 1-3.

The mean disorder parameter (Figure 61e) increased in the interval 100-160°C, remained constant at 160-190°C and decreased in the interval 190-225°C. The internal disorder as quantified by the disorder parameter increased up to 160°C and decreased at higher temperatures, indicating that internal mosaicity and strain build up for low temperatures and was released at higher temperatures. The shape of the distribution (Figure 61f) was similar for all temperatures, but was shifted towards larger values and slightly broadened at 157°C and 181°C, consistent with a build-up of strain and mosaicity. At 222°C the distribution was narrower and peaked at an intermediate value, consistent with subgrains becoming more defect-free and relieved of axial strain.

5.2.2 Shift, rotation and strain

The mean shift in horizontal detector position relative to the position at 85°C (Figure 61h) was constantly zero as expected if the sample position and orientation were steady and any overall motion eliminated in the data analysis. The distribution of horizontal shifts (Figure 61i) broadened with increasing temperature and at 222°C it had become a symmetric double peak. Furthermore, small symmetric side peaks were observed at 7 and 6 pixels shift for 181°C and 222°C, respectively.

The double peak character of the horizontal shift distribution at high temperature suggests a favorable accumulated rotation of 0.014°, which for a spherical subgrain of radius 1 μm corresponds to atoms near the boundary moving 2.5 Å

along the boundary, similar to the interatomic distance in the structure. Likewise, the side peaks at 6-7 pixels are equivalent to subgrain rotation of 0.03° or maximal atomic motion of 5.2 Å, and several of the subgrain tracks in Figure 61g exhibit even larger shifts of more than 10 pixels equivalent to rotations of 0.05°. These rotations were smaller than or equivalent to the step size in u and therefore similar lattice rotations in Δu could not be observed in the present experiment, although the position in u was a direct measure of lattice orientation. For comparison, a single edge dislocation (Burgers vector $b = 2.335$ Å) through the center of a subgrain of 1 μm radius causes a difference in lattice orientation of 0.013° from side to side. Thus rotations of a similar magnitude are expected if a dislocation enters or leaves the subgrain.

For the vertical detector position the mean shift (Figure 61k) increased steadily to approximately +1 pixel at 200°C before decreasing slightly towards the end of the temperature series. The distributions were broadening with temperature and peaked at positive shift. Note that the data was corrected for the vertical shift due to heat expansion of the sample by image registration before carrying out the analysis, and the observed average positive shift stem from the deviation of individual spots from the overall behavior. The distributions had a shoulder at -3 pixels above 157°C and symmetric side peaks at shifts of 7 pixels for the two highest temperatures.

The side peaks in the vertical shift distribution suggests that changes in axial strain of $\epsilon = 5.3 \cdot 10^{-4}$ are significant. For a spherical subgrain of 1 μm radius such a change in axial strain means a lattice expansion or contraction that correspond to atoms near the subgrain boundary moving 5.3 Å along the radial direction, again similar to the interatomic distances in the sample. It is not possible from these measurements to conclude whether strain is building up or released, since the actual strain in individual subgrains cannot be determined. However, the observed changes in strain are consistent with internal stresses typically found in aluminium (sub)grains of this size. The positive mean shift in vertical detector position indicates that the subgrains that were traceable through the whole temperature series on average expanded less than what would be expected for a heat expanding lattice without strain at all temperatures. It is not possible from these measurements to determine whether negative axial strain is building up due to external pressure on these subgrains or whether initially present positive strain is released due to heat expansion of the whole sample.

All shifts in detector position of individual subgrain spots were interpreted in terms of lattice rotations and changes to internal strain, since the observed changes in subgrain sizes were too small to generate center-of-mass translations large enough to explain the observed shifts. This argument is quantified as follows: A shift of a diffraction spot on the detector of 1 pixel in either direction is equivalent to a subgrain center-of-mass translation of 0.622 μm. The smallest change in size that would produce a center-of-mass translation of 0.622 μm for a spherical subgrain is a change of radius by that length. The observed subgrain radii are, however, on the order of 1 μm and in general the subgrains are not observed to grow or shrink sufficiently to cause a shift of several pixels.

Coalescence of two spherical neighboring subgrains of 1 μm equivalent radius would result in a center-of-mass translation of 1 μm and an increase of equivalent radius to 1.3 μm, since the combined subgrain would no longer be spherical but elongated along the line connecting the centers-of-mass of the two merging subgrains. Thus, this mechanism is consistent with the observed shifts and growth. However, coalescence would most likely also involve a rotation of one or both subgrains as well as changes to internal disorder and strain, which would give rise to larger shifts than the mere translation.

Furthermore, the changes in detector position related to center-of-mass translation should be similar in all directions, yielding similar features in the distributions of both horizontal and vertical shifts, which is not the case. The observed side peaks at 6-7 pixels appear similar (see Figure61i and l), but would indicate a center-of-mass translation of minimum 3.7 μm, which is not consistent with the observed small changes in size. However, the smearing out of the distributions could be caused by center-of-mass translations in combination with subgrains adjusting their orientation and lattice parameter slightly.

5.2.3 Growing and shrinking grains

The statistical analysis may be taken even further by looking at growing and shrinking subgrains separately, see Figure 62, where statistics for growing subgrains are red and for shrinking subgrains are blue. Several differences were observed. These are pointed out in the following and interpreted in terms of dynamics specific to either growing or shrinking subgrains.

The size distributions appeared very similar for the growing and shrinking subgrains with only minor changes over time (Figure 62a-b and e-f). On the

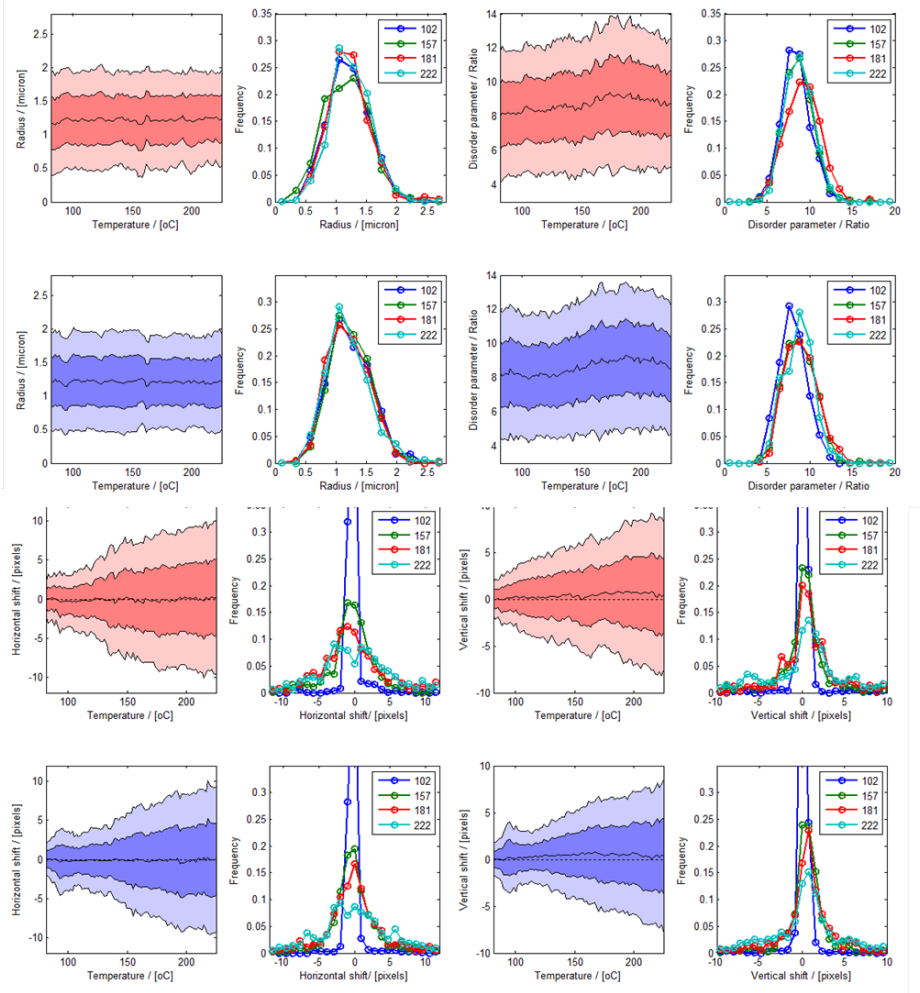

Figure 62: **Growing and shrinking subgrains** Statistics for growing (red) and shrinking (blue) subgrains seperately. a)-h) Size and disorder parameter distributions. i)-p) Horizontal and vertical shifts. Central lines are means as a function of temperature, surrounding lines are 1 and 2 standard deviations, respectively. Also shown are histogram distributions at four different temperatures.

other hand, comparison of Figure 62c and g revealed that for temperatures below 150°C the mean disorder parameter for growing subgrains was larger than for the shrinking ones and almost constant, whereas an increase was observed for the shrinking subgrains. At higher temperatures above 160° the disorder decreased for growing subgrains but was almost constant for shrinking subgrains. These

differences were confirmed by the distributions of disorder parameters shown in Figure 62d and h and are consistent with a build-up of internal disorder in shrinking subgrains at low temperature and a clean-up, primarily in growing subgrains at higher temperature.

Interpreting vertical shifts as deviation in the axial strain and horizontal shifts as rotation, several differences are observed. Both shift distributions for shrinking subgrains (Figure 62m and o) exhibited a broadening at 90°C followed by a narrower part at 110°C, a feature which was not present in the distributions for growing subgrains (Figure 62i and k). However, strain distribution for growing subgrains (Figure 62k) exhibited a similar feature at 160-170°C, which was not present in the other distributions. This indicated a transition behavior specific to shrinking and growing subgrains, respectively. The deviation of strain was zero at 160°C for growing subgrains followed by an increase to a constant value of approximately 1 pixel (Figure 62k) whereas for shrinking subgrains (Figure 62o) the shift increased until 180°C followed by a slow decrease to close to zero above 210°. These differences indicated that the growth behavior was related to the internal strain and mosaic properties of individual subgrains.

Above 180°C the rotation distributions for the shrinking subgrains (Figure 62n) had a set of distinct side peaks at 6-7 pixels. For the growing subgrains the distributions were broader and the side peaks less distinct with more intensity at larger absolute shifts (Figure 62j). The lattice orientation of the growing subgrains changed gradually as the subgrains grew leading to a variety of horizontal shifts, whereas the shrinking subgrains seemed to undergo a certain rotation only, yielding the side peaks.

Likewise, at 181° the strain distributions for growing subgrains (Figure 62l) had distinct side peaks at 3 and 6 pixels and at 222°C exhibited distinct side peaks 7 pixels, strongest on the negative side, whereas for shrinking subgrains (Figure 62p) there were broad shoulders out to 8 pixels. The peak center moved towards reduced lattice parameter (increased shifts) with temperature for the shrinking subgrains, whereas for growing the peak position did not until the highest temperature.

Thus the evolution of distributions with temperature was clearly different for shrinking and growing subgrains, respectively, indicating that the individual growth behavior was connected to the internal dynamics in the individual subgrains.

5.2.4 Individual growth curves and growth rates

The individual size (Figure 61a), disorder parameter (Figure 61d) and horizontal and vertical shift in detector position (Figure 61g and 61j) of individual subgrains were tracked during heating. No two growth curves were identical and individual subgrains would grow in one temperature interval and shrink in another. None of the 498 tracked subgrains were observed to grow more than to about a doubling of the equivalent radius and none shrunk to less than half the initial radius (Figure 61a). Some subgrains exhibited large changes and some only small changes, with the largest changes observed to happen between 120°C and 190°C. Some changes happened smoothly and continuously over larger temperature intervals, other changes were abrupt. In general, no obvious correlation could be derived from the growth curves and the evolution of monitored parameters for individual subgrains. Average behavior of all the tracked subgrains did not reflect the diversity of individual kinetics fluctuations.

For each temperature the mean growth rate and standard deviation for growing and shrinking subgrains are shown in Figure 63a. The main features of the absolute mean growth rate as a function of temperature were two peaks, a large increase at 160°C and a smaller one at 90°C. For growing subgrains the mean growth rate increased in the interval 100-140°C whereas the growth rate was constant for shrinking subgrains. The distributions of growth rates (Figure 63b) were sharply peaked at zero. The distribution at 157°C was broader than for the other temperatures, indicating faster dynamics at this temperature.

Note that each individual subgrain may grow in one temperature interval and shrink in another. Thus the number of growing and shrinking subgrains changed with temperature and the average subgrain size and size distribution remained almost constant, see Figure 63b and 63c. The peak in the mean growth rate around 160°C as well as the broadening of the associated distribution suggested that at this temperature a thermally activated process that was not dominant at lower temperatures suddenly became energetically favorable, causing faster growth processes at this temperature. However, since the overall size distribution and mean size did not change markedly, this process merely caused a rearrangement of boundaries, not actual coarsening.

No obvious correlation between subgrain size and growth rate was evident from the scatterplot of growth rate versus volume, shown for all 498 subgrains at four different temperatures in Figure 63c. The Kendall τ-coefficient was approx-

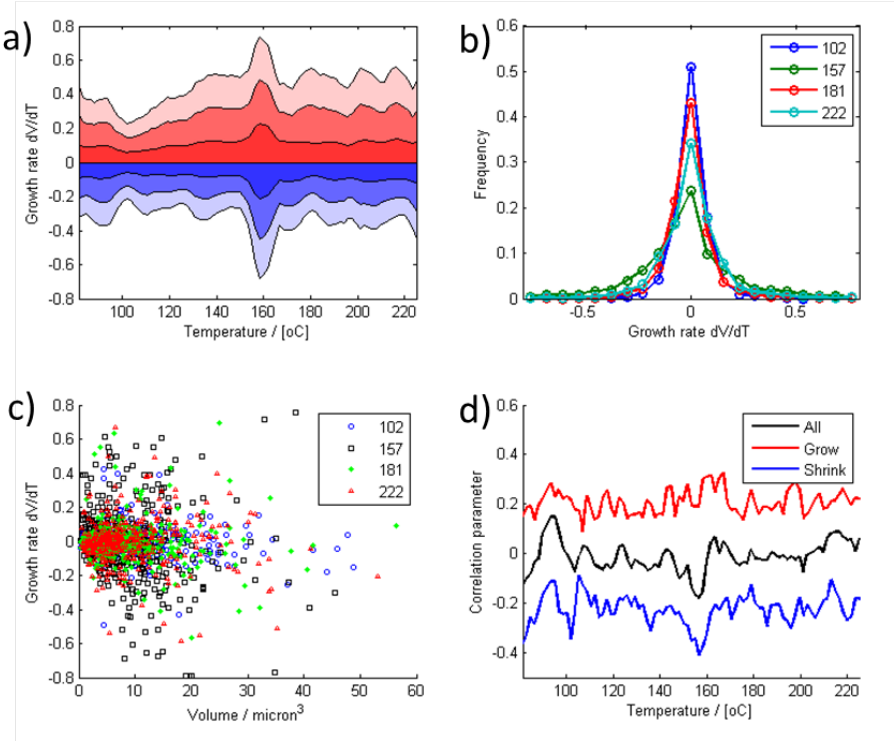

Figure 63: **Growth rate** a) Mean growth rates as function of temperature. Red: Growing, Blue: Shrinking. Lines closest to zero are mean growth rate, followed by 1 and 2 standard deviations, respectively. b) Distribution of growth rates for 4 temperatures. c) Growth rate versus size at 4 temperatures. d) Correlation between Size and growth rate as a function of temperature for all, growing and shrinking subgrains respectively.

imately zero when all subgrains were included, see Figure 63d, thus subgrain size did not determine whether a subgrain was growing or shrinking. For growing subgrains it was found that the larger subgrains were more likely to have a larger growth rate ($\tau \approx 0.2$). However, this also applied to the absolute growth rate for the shrinking subgrains, since $\tau \approx -0.2$ implied that shrinking subgrains of larger volume were more likely to have a larger negative growth rate. Thus larger subgrains were more likely to have larger absolute growth rates. At 160°C the correlation parameter for shrinking subgrains had a peak ($\tau \approx -0.4$) followed by a peak in the correlation for growing subgrains ($\tau \approx 0.3$). None of the tracked subgrains were small and shrinking fast since these would have disappeared during the temperature series, which however does not influence

the observed lack of correlation.

5.3 Model for recovery

Several observations presented in the previous section are in direct contradiction with the models for recovery presented in Chapter 2, including the individual growth kinetics, small changes to internal orientation and strain, and in particular the lack of a correlation between size and growth rate. Therefore, in this section a simple size-independent model is introduced and applied to extract transition temperatures from the individual growth curves. The section finishes with an analysis of the differences between growing and shrinking grains.

5.3.1 Simple model for growth rates

Because no obvious correlation between subgrain size and growth rate was observed, the subgrain size was omitted in a simple model of thermally activated subgrain growth, and the growth rate was represented by:

$$v_g = v_\infty \left(1 - \frac{T_c}{T}\right) \tag{117}$$

Here v_∞ is the growth rate at large temperature and T_c is a critical temperature above which the available thermal energy is large enough to active growth, which may have positive or negative growth rates. Linear fits to v_T as a function of inverse temperature $1/T$ for each subgrain were made for ten smaller temperature intervals of 7-10 temperature steps to determine v_∞ and T_c. An example is shown in Figure 64 for 10 randomly selected subgrains. The fits to other intervals and subgrains appeared similar, with bundled curves intersecting at some central value and occasionally an outlier when growth was continued from previous temperature intervals. The data was smoothed before taking the derivative and fitting.

Figure 65 shows the distributions of critical temperatures obtained from the fits. The temperature steps in the corresponding intervals are indicated below the distributions with circles of the same color. The T_c-distributions were all peaked within the corresponding temperature interval and the majority of the determined critical temperatures fell within the interval. The distributions around 90°C and 100°C as well as around 150°C and 170°C are sharply peaked and the rest are broader. There seems to be a broadening of the distributions towards higher temperature in two series, up to 150°C and above 150°C.

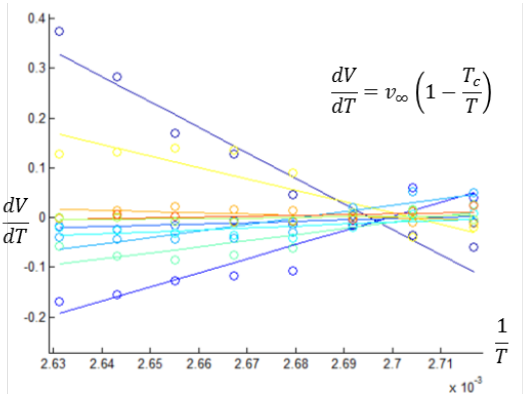

Figure 64: **Growth rate versus inverse temperature** Example of fit interval in size-independent model for ten randomly selected subgrains.

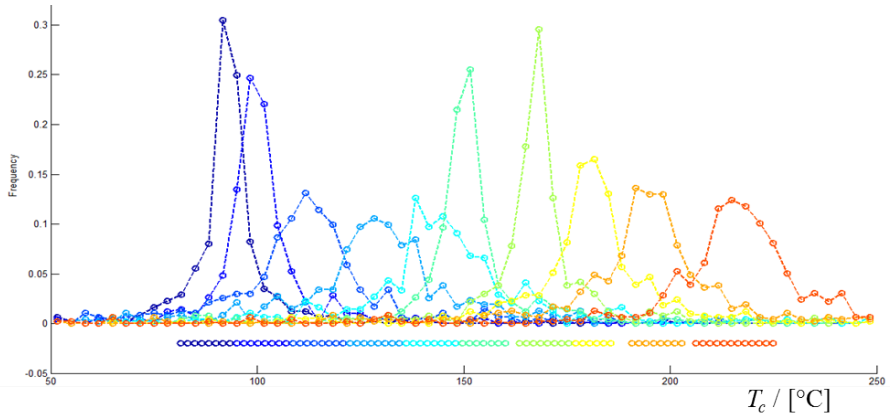

Figure 65: **Critical temperature T_c in size-independent model.** Distributions of critical temperatures as obtained from fits to the model for the corresponding fit intervals indicated below zero by circles of the same color. Each circle represents a data series.

Since the distributions of critical temperatures were peaked within the corresponding temperature interval and the majority of T_c's fell within the interval, the heating rate was slow enough to allow all thermally activated processes at a given temperature to occur before the temperature had increased significantly.

5.3.2 Stages of recovery

All subgrains were of similar size and no significant coarsening took place during the experiment since the size distribution and mean equivalent radius remained

largely unchanged, see Figure 61. Nevertheless, the size and disorder parameter for individual subgrains evolved with temperature, as did the orientation and axial strain. Several different stages of recovery were observed: Two transition stages around 90°C and 160°C, respectively, identified by peaks in the growth rates and narrow T_c-distributions, a build-up stage at 100-150°C, where the internal disorder of individual subgrains increased, and a release stage above 180°C where the internal disorder decreased. From the traces of individual subgrains it was evident that the most marked changes happened in the temperature interval 130-190°C. In the following the three different stages are characterised.

The observed transition stages exhibit more dynamical changes than before and after. In a material like AA1050 with many impurities there are many obstacles pinning the dislocations and boundaries, thus different individual boundary motion is expected to be initiated at all temperatures. Nevertheless, distinct transition stages were observed. The first transition stage around 90°C was associated with a peak in the average disorder parameter as well as increased spread of shifts for the shrinking subgrains, but no obvious indications for the growing subgrains. The second transition stage at 160°C was associated with the maximum observed disorder parameter, increased spread of shifts for the growing subgrains but none for the shrinking ones, and the larger changes to strain and orientation was onset here. The increase in disorder parameter up to this temperature as well as the deviation in the changes to the strain with respect to the overall thermal expansion indicated that the growth processes depend on the internal structure of the subgrains and not merely the boundary structure and curvature.

The observed transition temperatures could correspond to the observed onset of recovery (see Chapter 2) and may be interpreted as thermal activation of new mechanisms of dislocation motion at these temperatures. However, from the present measurements it is not clear whether the specific transition temperatures is a general feature of all similar specimens or if the observed sudden dynamical changes in this temperature range was caused by a mechanism specific to the specimen under investigation. Thus it is not possible to settle whether the observed dynamics are due to general properties of single dislocations and boundaries or a thermally activated local event which initiated a cascade of other events in its vicinity.

For the build-up stage in the interval 100-150°C the average disorder parameter increased and the average expansion of the lattice of individual subgrains

was observed to be smaller than the average thermal expansion. The growing subgrains possessed larger internal disorder than the shrinking ones and it remained constant in the interval. For the shrinking subgrains the disorder parameter increased in the interval to a value similar to the constant value observed for growing subgrains. Likewise, the deviation in lattice expansion was primarily found with the shrinking subgrains and no rotation was observed.

These observations are consistent with subgrain boundary motion driven by the difference in internal energy across the boundary due to differences in dislocation densities inside the two neighbouring subgrains. When boundaries move, dislocations are left behind in the growing subgrains and squeezed together in the shrinking ones, thereby leaving the overall properties of growing subgrains unchanged whereas the internal disorder in shrinking subgrains increases as the average lattice parameter decreases. Thus at this stage the subgrain boundary motion is not directly curvature driven, but forced by the mediation of internal pressure due to dislocation density.

A release stage was observed above 180°C where rotations and changes to lattice parameters consistent with single dislocations moving to the subgrain boundary were observed. As the subgrains change size the disorder decreases, especially for the growing subgrains, indicating that subgrain boundary motion now cleans up the few dislocations stuck in the interior of subgrains. The motion is thus driven by a reduction in the energy stored inside the subgrains, possibly in combination with a reduction in boundary surface energy when interior dislocations are included in the subgrain boundary or annihilated by boundary dislocations. Possibly, dislocations were also emitted from the subgrain boundaries into the interior of the subgrains thereby increasing disorder and causing the boundaries to follow.

5.3.3 Recommendations for future models for recovery

It is customary to quantify recovery in terms a bulk property such as the average (sub)grain radius and investigate the evolution of this property with temperature or annealing time. However, in the present study the average equivalent radius was found to be almost constant although the radii of individual subgrains could change markedly. The driving force may be related to local dislocation or subgrain boundary curvature, but was found to not be directly correlated to the subgrain size since no correlation between subgrain size and

growth rate was observed. Rather, the dynamics seemed to be determined by the internal strain and remaining dislocation density causing disorder in individual subgrains. These findings indicate that the evolution of the average subgrain size or mesh size is not an adequate measure of the extent of recovery for low temperature studies. Instead, the dynamics of individual subgrains and the evolution of their internal strain and dislocation density should be monitored to quantify the overall processes via statistics. A typical dislocation density of $10^{12}\mathrm{m}^2$ in a subgrain of 1 μm radius indicates that as few as 3 dislocations intersect a cross-section of the subgrain. Nevertheless, the dynamics of these seem to have huge influence on the dynamics of the hosting subgrain. Furthermore, the involved mechanisms are likely to be bulk properties since the small strains involved are relieved at free surfaces. Therefore it is crucial to develop techniques such as the method presented in this section that allow for *in situ* characterization with high angular resolution of many individual subgrains in the bulk at the same time, and the findings for the highly individual subgrain kinetics should be incorporated in new models.

5.4 Mapping subgrain structure

Based on the experiment presented above (part of) a subgrain map of the deformed structure may be obtained by triangulation if the sample is illuminated by a narrow line beam (as in DFXRM) and the same data series is acquired at two or more different sample-to-detector distances. Furthermore, additional reflections may be collected by translating the detector vertically to other 2θ values and the detector may be moved in the detector plane to collect additional data at other values of η.

A first test of this method was performed for the same sample and setup as described above with a line beam of 200 nm in height restricted by slits to a width of 100 μm. An illuminated layer containing a recrystallizing grain was selected and data similar to the data series presented above for one temperature step was collected for both (111) and (002) parallel to RD.

The preliminary data analysis was done by manual inspection of the diffraction spots by identifying the same spot in data at two different detector positions. The intersection between the line through both spots and the illuminated then gave the position of the subgrain in the sample. In this way, the center-of-mass of more than 100 individual subgrains were traced to regions within the

deformed structure. The accuracy of the triangulation was estimated to be on the order of 1 μm by determining the range of positions allowed by the extend of the two diffraction spots. The outcome is shown in Figure 66. The approximate shape of the recrystallizing grain is indicated in green. Distinct spots due to the internal structure of the grain are observed.

The individual subgrain sizes may be obtained from the intensity of the diffraction spot as described above and the orientation and strain may be extracted from the position of the diffraction spot when the direct space position is known. Combining this technique with DFXRM, both the recrystallising grain and the surrounding subgrains may be mapped in 3D within a timespan of a few hours to days, depending on the volume and resolution.

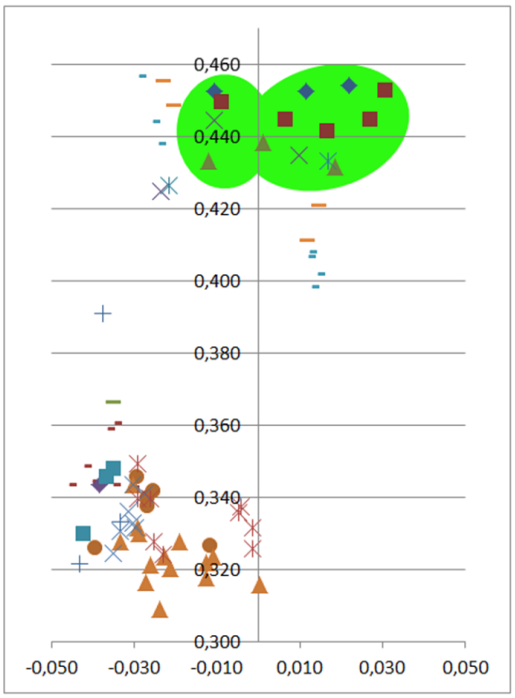

Figure 66: **Center-of-mass map of subgrains** A first test of the triangulation method for mapping subgrain structures. The center-of-mass position of individual subgrains are indicated by points and the approximated shape of a present recrystallizing grain is shown in green. Axes are in μm.

6 Outlook

The project behind the present thesis has offered a variety of very different tasks from hands-on making the experiment work and writing scripts for data analysis to revising metallurgical models and a substantial amount of pen-and-paper tensor maths. Not surprisingly, there are many loose ends and new problems discovered, but also encouraging work in progress and interesting new ideas to be tested. This section gives an overview of what to do next.

6.1 X-ray imaging in the future

DFXRM has been demonstrated in this thesis to be a promising new tool for fast non-destructive imaging. As the new member of the x-ray imaging family, the technique needs maturing to realize the optimal data acquisition strategies. At that point the technique may easily be combined with other techniques at the same setup, and the ultimate experimental setup would provide full grain map of a polycrystalline sample by 3DXRD or DCT with online data analysis. Then a zoom on a specific selected grain could be obtained by tomo-tomography and a by further zooming in to a specific layer of the grain, the internal structure could be mapped by DFXRM. Annealing (or deformation) could be performed with the sample still mounted on the instrument and the measurements could be repeated by zooming out to do a grain map, zoom in on a selected grain and so on.

Furthermore, in recrystallizing samples the subgrain structure could be mapped by the triangulation technique proposed in the previous chapter. Alternatively, by appropriately placing the near field detector at different η the full 2θ-ring may be collected and taken as input for a near field version of the 3DXRD reconstruction. In this way the interplay between the migrating boundary and the surrounding subgrain structure could be investigated with high angular and spatial resolution. For example it would be interesting to find out if the subgrains immediately outside the boundary prepare to become a part of the recrystallizing grains by rotating or changing in other ways.

6.2 Extensions of the DFXRM technique

DFXRM is currently based on sampling volumes layer-by-layer by illuminating the sample with a narrow line-beam and translating the sample to reconstruct

the 3D volume from layers afterwards. As an alternative to scanning layer-by-layer a volume map of the internal structure of the grain may be obtained by topo-tomography with an additional DFXRM mosaicity or strain scan at each orientation. In this way the strain fields of single dislocations in a diamond crystal have been mapped, see [MRSpaper], and with appropriate reconstruction algorithms this procedure may be extended to mapping the structure of dislocation networks in embedded grains etc.

The high angular resolution of the microscope is both a gift and a curse since DFXRM is best suited for samples of very small variations in orientation and strain and not for deformed samples. However, a map of a subgrain structure with high spatial resolution and individual average subgrain orientation could be obtained from sweeping over larger angles at the cost of the high angular resolution. Optimal settings for angular step-size, magnification etc. should be tested, bearing in mind the relation between angular and spatial resolution as discussed in Chapter 3.

While evaluating the theoretical properties of CRLs it became apparent that the back-focal plane has special properties that could be utilized for a different approach to microscopy. At this plane all parallel rays from the sample plane meet in the same point. Thus by blocking out a point in the back-focal plane the direct space points of that particular lattice orientation will be dark in the detector image, and thus series of images at different blocked-out points can provide mosaicity map.

A way of exploiting the full dimensionality of DFXRM data could be an approach that has been termed Ultramicroscopy. The idea is to utilize the distinct appearance of the measured local orientation distribution if defects are present for a forwards-backwards reconstruction that iteratively matches the generated diffraction from the assigned mosaicity map to the actual orientation distributions. In this way a detailed map of internal dislocation structures could be obtained. The method could be supplemented by high resolution reciprocal space maps. However, the effort needed to write the reconstruction algorithm together with the promising dislocation density approach presented in this thesis takes Ultramicroscopy off the top-priority list.

Of course, there is also an option to combine dark field microscopy with bright field measurements. For this purpose a semi-transparent detector has been installed.

6.3 Experimental problems to be solved

During the first experiments for this thesis work it was a struggle aligning the microscope due to limited motor step-size, too few degrees of freedom, and an unreliable sample stage. However, the instrument has been fully rebuilt with a new sample stage fit for the purpose and with more degrees of freedom, which has hugely simplified the alignment procedure and provides more reliable measurements. Further improvements of the microscope include the introduction of multi-layer Laue lenses as the condenser and the installation of a furnace for annealing studies. Nevertheless, there is currently still an unresolved problem related to the focusing and effect of the CRL objective lens. The current methods for focusing are not very precise and the scheme for focusing as suggested in Chapter 3 of this thesis should be tested and automated if successful.

Despite a huge effort it has not been possible to theoretically account for the large shifts observed in some data series. All theoretical considerations regarding CRLs have been based on the ray transfer formalism, with the basic assumptions that the angle of incidence of rays on the lenslet surfaces is small to allow for a linear approximation for refraction and no reflection. However, even for small tilts of the optical axis (see Chapter 3) the angle of incidence is not small due to the parabolic shape of the lenslets. Therefore it is suggested to consider non-linear effects if the problem with shifts persists (and to perhaps save some of the shifted data-sets).

Another technical difficulty is to relocate the same layer in a sample after annealing, since the shape of the grain under investigation may have changed during the heat treatment. In a recent experiment not reported in this thesis the external shape of the sample was successfully utilized to relocate the same layer. The sample surface was structured by the cutting procedure and had a roughness on the order of 10 μm. From the bright field image of the sample the position could be adjusted with submicron precision. Alternatively, fast DCT could be implemented as a tool for identifying the internal structures.

6.4 Data analysis

A problem encountered during data analysis is the apparent shifts of consecutive images and layers with respect to each other. These shifts can in principle be corrected for using image-registration. This has successfully been done for thin film samples, but it has proven difficult for grains, partly because the intensity

distribution in the images changes a lot with angle so that standard methods cannot be applied, partly because it is not obvious which shifts are physical and which are not. Thus to correct the affected data series there is a need to define a reliable (and physical!) registration optimization. Many such ideas have been tested during the data analysis for this thesis, however, none proved successful. Furthermore, a non-consistent and as of yet unexplained in-plane shift from layer-to-layer has been observed, which has set a stop to the dislocation density analysis as presented in Chapter 4, since derivatives in z could not be obtained. This issue should be resolved as soon as possible to be able to match layers and obtain 3D structures.

The extraction of mosaicity and strain is currently done for each voxel individually without any comparison to the properties of the neighbouring voxels. Instead, it could prove fruitful to implement a segmentation algorithm, fast multiscale clustering (FMC) in particular. The FMC algorithm segments N dimensional on an increasingly fine scale, therefore it can be applied to structures that contains structures of many different length-scales and orders of magnitude differences in the parameter that separates clusters - perfect for polycrystals. By means of FMC it should be possible to resolve structures more reliably and physically accurate that by simply assigning a value from the orientation distributions. The implementation of this algorithm is further relevant for EBSD where series of Kikuchi-patterns may be taken as input and overlapping signals due to multiple orientations present in the same voxel could be resolved.

6.5 Ideas for experiments and more

Here follows a list of examples of measurements that could be done with DFXRM in the near future. First of all the recovery experiment presented in Chapter 5 should be repeated for a similar sample, for higher temperatures and for constant temperature. The amount of information is immense compared to the measuring time and effort and the data presented in this thesis calls for more, since it has become evident that the current models for recovery are not in agreement with reality. New models should be derived that takes into account the individual kinetics observed for subgrains during recovery and for that more empirical information is needed. This could be complimented for example by glass- DFT simulations in the same way phase-field simulation supplements grain growth studies.

Likewise, the triangulation method demonstrated in Chapter 5 should be applied and combined with DFXRM of the recrystallizing grain during annealing to shed more light on the interplay between the recrystallizing grain and the surrounding subgrains. Much could be learned from such an experiment about the effects of subgrain orientation and structure on the boundary migration of recrystallizing grains. Furthermore, the nature of the intragranular structure and its relation to the structure of the deformed matrix could be revealed. (Data has already been collected but is yet to be analysed.)

The mapping of the strain field of a single dislocation by means of DFXRM has been demonstrated and the next step is to 'film' dislocation motion and dislocation interaction. The theoretical description of the fields associated with dislocation is usually limited to a static 2D-approach as is presented in Chapter 2. However, thermal lattice vibrations may cause standing wave strain fields around the dislocation. These fields would not be visible by other techniques since the oscillations are fast and a standing wave behavior would be cancelled out when averaged over time. However, such fields might be visible with DFXRM since all orientations and strains present in a voxel are measured, not only the average. Oscillating fields or not, DFXRM is a valuable new tool for visualizing dislocations in thick samples and supposedly the topo-tomographic method can be extended to dislocation networks and other complex structures, provided the microscope is properly focused. In that case a dislocation network within a grain could be visible in the off-peak images.

A final, more wild idea should be mentioned, namely the possibility of measuring the pressure in the different parts of a leaf *in vivo*. This is an open question that challenges biophysicists because models of fluid flow in plants depend strongly on the pressure and pressure-differences inside plant cell-structures and currently no method exists to verify the assumptions. It is proposed to utilize the self-precipitation of silver nanoparticles in a leaf to image the pressure-induced variations in the lattice constant of the nanoparticles. According to calculations, this should be barely doable with the current DFXRM setup. The only remaining problem is how to mount a living tree on the instrument.

7 Conclusion

Recrystallization of metals is a complex process involving structure and dynamics at multiple length-scales. This thesis presents a first application of dark field x-ray microscopy (DFXRM) within recrystallization. The aim of the thesis was to apply DFXRM to a partly recrystallized sample and thereby address open questions regarding the structure of recrystallizing grains, the surrounding subgrain structure, and the relation between them. Two different types of experiments were conducted, DFXRM mapping of mosaicity and strain in recrystallizing grains and a statistical annealing study aimed at monitoring the evolution of the individual subgrains during recovery.

As part of the thesis work a theoretical description of the microscope and the objective lens in particular was derived, yielding expressions for resolution and optimization. Furthermore, a novel scheme for focusing the microscope utilizing out-of-focus shifts in acquired data was suggested.

The sample of choice was aluminium AA1050 cold-rolled to 50% reduction in thickness and annealed at 325°C for 50 minutes to obtain aproximately 50% recrystallization. Several bulk recrystallizing grains were mapped in 3D by illuminating the sample layer-by-layer utilizing a narrow line-beam 200-300 nm in height. The spatial resolution was 100 nm along the best direction, the angular resolution was on the order of millidegrees and strain resolution was 10^{-4}.

From mosaicity and strain maps it was evident that the recrystallizing grains possessed an internal structure in the form of a well-defined network of ultra low angle boundaries. A first analysis of these ultra low angle boundaries showed that they carried a misorientation of 0.1° or less and separated regions of less dislocation content with sizes on the order of a few μm. Some boundaries were sharper than could be resolved by the instrument whereas other boundaries were several μm wide. A direct correlation between the intragranular structure and the external grain boundary was observed as the grain boundary exhibited retrusions at points where the low angle boundaries met the boundary of the recrystallizing grain. An annealing study showed that the intragranular structure became more ordered during heat treatment.

The theoretical framework for analysing DFXRM-data in terms of distortion fields and dislocation densities was presented and demonstrated for a thin film sample of simple geometry. On applying a similar analysis to the map of a large

grain $\approx 100\mu$m a patterned structure appeared, reminiscent of the subgrain structure of the deformed matrix. A distinct region in the central part of the grain possessed a different, more strongly diffracting structure. These findings suggest that recrystallization in this sample may be a two-step process involving grain boundary migration followed by recovery of the remaining dislocation network within the recrystallizing grain.

The subgrain structure was monitored during recovery at constant heating rate and temperatures well below the onset of recrystallization. A method for tracing the variations in size, orientation and strain of several hundred individual bulk subgrains $\approx 1\mu$m in size was demonstrated.

From the statistical analysis of individual growth curves it was observed that each subgrain exhibited its own growth kinetics. The size of individual subgrains could change markedly, but the average grain size remained unaltered. Slight changes to orientation ($\leq 0.05^\circ$) and strain was observed as well, consistent with a slight reorientation or relaxation due to a single dislocation motion.

The growth rate for each subgrain as a function of temperature was derived from the growth curves. In contradiction with prevalent models, no correlation between growth rate and subgrain size was observed. This finding calls for a reformulation of recovery models to incorporate the observed highly individual subgrain dynamics. In this thesis a simple size-independent model was applied to extract critical temperatures. From this analysis a transition stage was identified at 160°C, consistent with the onset of recovery as measured by calorimetry.

As a final feature, promising first results from a preliminary test of a new triangulation method for mapping subgrain structures were presented. The center-of-mass position of individual subgrains was tracked to within 1 μm providing a new method for mapping simultaneously the recrystallizing grain and the subgrain structure of the deformed matrix surrounding it.

Together with existing x-ray imaging techniques the DFXRM-methods as presented in this thesis provide a powerful toolbox for studying recrystallization of metals.

List of References

HullBacon2011 D. Hull and D.J. Bacon, Introduction to Dislocations, fifth edition, Elsevier, 2011.

Volterra1907 V. Volterra, Ann. Ecole Norm. Super. 24 (1907) 401

Taylor1934 G.I. Taylor, Proc. Royal Society of London, Series A 145 (1934) 362.

Orowan1934 E. Orowan, Z. Physik 89 (1934) 605.

Polanyi1934 M. Polanyi, Z. Physik 89 (1934) 660.

Vogel1953 Vogel, Pfann, Corey, Thomas, Physical Review 90 (1953) 489.

Zhang2011 X. Zhang, A. Godfrey, X. Huang, N. Hansen, Q. Liu, Acta Mat. 59 (2011) 3422

Zhang2016 X. Zhang, N. Hansen, A. Godfrey, X. Huang, Acta Mat. 114 (2016) 176

Kröner1958 E. Kröner, Z. Physik 151 (1958) 504

Nye1953 J.F. Nye, Acta Metallurgica 1 (1953) 153

Weertman1992 J. Weertman, J.R. Weertman, Elementary Dislocation Theory, Oxford University Press, 1992.

Lazar2003 M. Lazar, Computational Materials Science 28 (2003) 419.

Gutkin1999 M.Yu. Gutkin, E.C. Aifantis, Scripta Mat. 40 (1999) 559.

Nowacki1986 W. Nowacki, Theory of asymmetric elasticity, Pergamon Press, Oxford, 1986.

Wilsdorf1999 D. Kuhlmann-Wilsdorf, Phil. Mag, A 79 (1999) 955.

HH2004 F.J. Humphreys, M. Hatherly, Recrystallization and related annealing phenomena, second edition, Elsevier, 2004.

Haessner1978 F. Haessner, Recrystallization of metallic materials, 2nd ed., Reiderer-Verlag, Stuttgart, 1978

Yu2015 T. Yu, A. Hughes, N. Hansen, X. Hung, Acta Mat 86 (2015) 269

Hong2013 C. Hong, X. Huang, G. Winther, Phil. Mag. 23 (2013) 3118

BayHansen1992 B. Bay, N. Hansen, D. Kulhmann-Wilsdorf, Mat. Sci. Eng. A158 (1992) 139

OrsundNes1989 R. Orsund, E. Nes, Scripta Metallurgica, 23 (1989) 1187

vonNeumann1952 J. von Neumann, Metal interfaces (ed. C. Herring) (1952) 108

Mulins1956 W.W. Mullins, J. Appl. Phys. 27 (1956) 900

MacPherson2007 R.D. MacPherson, D.J. Srolovitz, Nature 446 (2007) 1054

Hu1963 H. Hu, Trans. Met. Soc. AIME 224 (1962) 75

Vandermeer1959 R.A. Vandermeer, P. Gordon, Trans. Met. Soc. AIME 215 (1959) 577

Moelans2013 N. Moelans, A. Godfrey, Phys. Rev, B 88 (2013) 054103

Schmidt2004 S. Schmidt, S.F. Nielsen, C. Gundlach, L. Margulies, X. Huang, D. Juul Jensen, 305 (2004) 229

Lepinoux2010 J. Lepinoux, D. Weygand, M. Verdier, C.R. Physiquie 11 (2010) 265

Krill2002 C.E. Krill III, L.-Q. Chen, Acta Mat. 50 (2002) 3057

McKenna2014 I.M. McKenna, H.F. Poulsen, E.M. Lauridsen, W. Ludwig, P.W. Voorhees, Acta Mat. 78 (2014) 125

Als2001 J. Als-Nielsen, D. McMorrow, Elements of modern x-ray physics. John Wiley and Sons, 2001.

Warren1990 B.E Warren, X-ray Diffraction, Dover, 1990

Li2018 P. Li, A. Maiden, Scientific Reports, 8 (2018) 2049

Momose2003 Momose, A.; Kawamoto, S.; Koyama, I.; Hamaishi, Y.; Takai, K.; Suzuki, Y. Japanese Journal of Applied Physics. 42: (2003) L866.

Cloetens1997 P. Cloetens, M. Pateyron-Salomé, J.Y. Buffiere, G. Peix, J. Baruchel, F. Peyrin, M. Schlenker, Journal of Applied Physics 81 (1997) 5878

Nist2018 $http://physics.nist.gov/PhysRefData/FFast/html/form.html$

Henke2018 $http://henke.lbl.gov/optical_constants/getdb2.html$

Ludwig2009 W. Ludwig, A. King, P. Reischig, M. Herbig, E.M. Lauridsen, S. Schmidt, H. Proudhon, S. Forest, P. Cloetens, S. Rolland du Roscoat, J.Y. Buffiere, T.J. Marrow, H.F.Poulsen, Materials Science and Engineering A 524 (2009) 69.

Ludwig2001 W. Ludwig, P. Cloetens, J. Hartwig, J. Baruchel, B. Hamelin, P. Bastie. J. Appl. Cryst. 34 (2001) 602

vanBoxel2014 S. van Boxel, S. Schmidt, W. Ludwig, Y.B. Zhang, D.Juul Jensen, W. Pantleon, Materials Transactions 55 (2014) 128

Simons2015 H. Simons, A. King, W. Ludwig, C. Detlefs, W. Pantleon, S. Schmidt, I. Snigireva, F. Stöhr, A. Snigirev, H.F. Poulsen, Nature Comm, 6 (2015) 6098.

Poulsen2004 H.F. Poulsen. Three-dimensional x-ray difraaction microscopy - mapping polycrystals and their dynamics. Springer, 2004.

Lauridsen2003 E.M. Lauridsen, H.F. Poulsen, S.F. Nielsen, D. Juul Jensen, Acta Mat, 51 (2003) 4423.

Lauridsen2000 E.M. Lauridsen, D. Juul Jensen, H.F. Poulsen, U. Lienert, Scripta Mat. 43 (2000) 561

Poulsen2011 S.O. Poulsen, E.M. Lauridsen, A. Lyckegaard, J. Oddershede, C. Gundlach, C. Curf, D. Juul Jensen, Scripta Mat 64 (2011) 1003

Gundlach2004 C. Gundlch, W. Pantleon, E.M. Lauridsen, L. Margulies, R.D: Doherty, H.F. Poulsen, Scripta Mat. 50 (2004) 477

Hayashi2015 Y. Hayashi, J. Appl. Cryst. 48 (2015) 1094

Schmidt2008 S. Schmidt, U.L. Olsen, H.F. Poulsen, H.O. Sørensen, E.M. Lauridsen, L. Margulies, C. Maurice, D. Juul Jensen, 59 (2008) 491

Hefferan2012 C.M. Hefferan, J. Lind, S. F. Li, U. Lienert, A. D. Rollett, R. M. Suter. Acta Mat. 60 (2012) 4311

Lauridsen2001 E. M. Lauridsen, S. Schmidt, R.M. Suter, H.F. Poulsen. J. Appl. Cryst. 34 (2001) 744

Bernier2011 J.V. Bernier, N.R. Barton, U. Lienert, M.P. Miller, Journal of Strain Analysis for Engineering Design 46 (2011) 527.

ESRF2018 *http* : *//www.esrf.eu/*

Jakobsen2007 B. Jakobsen, H.F. Poulsen, U. Lienert, X. Huang, W. Pantleon, Scripta Mat. 56 (2007) 769

McDonald2015 S.A. McDonals, P. Reischig, C. Holzner, E.M. Lauridsen, P.J. Withers, A.P. Merkle, M Feser., Scientific Reports 5 (2015) 14665

Poulsen2014 S.O. Poulsen, H.F. Poulsen, Metallurgical and materials transaction A 45A (2014) 4772 Stöhr2015 F. Stöhr. Microfabrication of hard x-ray lenses. PhD Thesis, DTU, 2015.